Delft University of Technology
Department of Microwave Sensing, Signals and Systems
Faculty EEMCS

Feasibility Study on Optically Transparent Cylindrical Dielectric Resonator Antennas Integrated in an Enclosed Light Bulb Using Doppler Based Radar for Human Presence Detection

by

Mai-Han Truong

to obtain the degree of Master of Science
to be defended on October 3rd, 2018 at 14:30

MScEE track Telecommunications & Sensing Systems

Tuesday 25th September, 2018

Studentnumber:
4289811

TU Delft Supervisor
Prof. Dr. A. Yarovoy *Professor, Chairman*

Signify Supervisor
Ing. P. Boonen *Electronics Architect*

Exam Committee
Prof. Dr. A. Yarovoy *Professor, Chairman MS3*
Dr. F. Uysal *Assistent Professor MS3*
Dr. S.M. Alavi *Assistent Professor ELCA*

Signify Engineers
Dr. J.B. Mills *Senior Scientist*
Ir. M. Creemers *Lead Development Engineer*
Dr. A. Palaios *RF Engineer*

Signify
Confidentiality Statement

Abstract

This thesis will focus on an 24 GHz indoor human presence detection radar with an optically transparent dielectric resonator antenna (DRA) applied in an enclosed light source. The DRA was studied extensively by simulations and measurements and demonstrated to suffer from blind spots for radar implementation because of the light bulb housing. To apply a DRA for the presence detection, one should do measurements on the radiation patterns of the DRA to match the DRA to its housing environment.

A Frequency Modulated Continuous Wave (FMCW) radar was studied because of its possibility to detect almost static and moving humans. Simple waveforms such as the ramp and triangular waveform are used to obtain a beat frequency for presence detection. To linearize and remove the temperature and chip sample dependence of the BGT24MTR11 radar transceiver, a phase locked loop (PLL) was used based on the ADF4159 chip. The PLL was designed to have a loop bandwidth above 200 kHz and phase margin above 70 degrees, to reduce the frequency overshoot and have a relative fast lock. The system was tested and generated sweeps successfully for slow ramps, but failed on operating in the proper sweep bandwidth for ramps faster than 10 ms. The limitation on sweep time, lower transmit power and lossy circuitry were factors which made the radar system not suitable for human motion detection.

Words of Appreciation

I would first like to thank my thesis supervisor Mr. Yarovoy who is the head of Microwave Sensing, Signals and Systems (MS3) research group at Delft University of Technology. He managed the first contact between Philips Lighting and me since I was looking for a quarter length internship back then. After the internship Mr. Yarovoy continued to support me during the master thesis and helped me in steering the thesis in the right direction whenever needed. Very useful advice was given by him and other associate professors of the MS3 group including O.A. Krasnov, F. Uysal and J. Puskely. For measurement and validation of the designed antennas using the anechoic chamber of TU Delft P. Aubry spend days to help me who I am also very thankful for. F. van der Zwan also supported me a lot at my radar board demonstration by providing the measurement equipment. Other members of the MS3 group helped me a lot providing the equipment that I needed during my thesis and they were also present during my midterm presentation which included P. Swart and D. Tran.

From the very first day of the internship at Philips Lighting my supervisor Paul arranged a team of antenna/RF engineers who provided support a lot of feedback and useful suggestions on a weekly basis. Paul was also very helpful in forwarding my non-antenna related questions to the specialists that he knew and arranged a lot of electronics which were needed for my thesis. Math was one of the RF engineers who could provide a lot of information regarding the Hue bulb during my thesis. If he did not have the requested information, he provided contacts who could help me further with my product related questions. Alex was also part of the weekly antenna/RF team who managed to be at many weekly meetings even though it meant that he had to move towards our building every week. Alex was always very diligent in learning about new areas related to the research fields of my thesis and helped a lot with my academic writing at the beginning of my thesis. John is the last (but not least) person who was part of the weekly antenna meetings during my internship and thesis. I am very grateful for the time he spends on answering my doubts and his eager to share his outstanding knowledge on RF and antenna field. The casual tea sessions with John were always motivating and made me realize I really enjoyed working in a company. I also want to thank Dave who provided me with his measurement equipment for my radar system which took over half his working space. His input was always very helpful, especially on the phase locked loop design and phase noise measurement. For the antenna prototyping I would like to thank Jack Ruijs for his excellent PCB design skills and his eager to finding the right contacts for prototyping purposes. Herman is also a person that I want to thank a lot for the prototyping support where he always made his project number available for the (many) small activities in the workshop. The workshop was very useful for me during my thesis due to their expertise in prototyping and the many available electronic parts. Jo and Robert who were always very helpful in providing support from small soldering parts to PCB machining which I am thankful for. I would also like to thank my group manager Dik who provided full support in resources needed during the thesis and who involved me in many activities with other colleagues which helped me a lot to bond more with other group members.

I also want to say thanks to the interns in our research group at Philips Lighting for their understanding and motivating words and for helping me enjoying life at work. Shuang and Artjoms were keeping me company during lunch breaks and encouraged me to achieve my goals during the thesis. With Shuang I worked together during the internship which strengthened the teamwork between us and Artjoms was always there to have casual and fun conversations whenever needed. I would also like to thank Artjoms for his kindness of helping me out whenever some bus strikes happened, which would potentially prevent me from getting towards the company on certain days.

I must also express my profound gratitude to my parents for providing me with unfailing support and continuous encouragement throughout the years of my study and through the process of this thesis. They always encouraged me to get the best out of myself and to never give up. I would not be here where I am today without their love, support and confidence. My warmest and dearest

gratitude goes to Lennart, my lovely boyfriend who showed endless support and gave me a lot of confidence during my study and this thesis.

Thank you,
M.H. Truong

Eindhoven
Tuesday 25th September, 2018

Contents

Abbreviations

ACC	Adaptive Cruise Control
ADC	Analog Digital Converter
CDRA	Cylindrical Dielectric Resonator Antenna
CFAR	Constant False Alarm Rate
CP	Charge Pump
CPI	Coherent Processing Interval
CW	Continuous Wave
CZT	Chirp z-Transform
DAC	Digital Analog Converter
DC	Direct Current
DFT	Discrete Fourier Transform
DRA	Dielectric Resonator Antenna
EM	Electro-Magnetic
FDTD	Finite-Difference Time-Domain
FFT	Fast Fourier Transform
FMCW	Frequency Modulated Continuous Wave
FSV	Frequency Slope Variation
GCPW	Grounded Coplanar Waveguide
HDRA	Hemispherical Dielectric Resonator Antenna
IP	Ingress Protection Marking
IR	Infrared
ISM	Industrial, Scientific and Medical
LED	Light Emitting Diode
LFMCW	Linear Frequency Modulated Continuous Wave
LUT	Look Up Table
MCPCB	Metal Core Printed Circuit Board
MTI	Moving Target Indicator
PCB	Printed Circuit Board
PFD	Phase Frequency Detector
PLL	Phase Locked Loop
PM	Phase Margin
PN	Phase Noise
PRF	Pulse Repetition Frequency
PRI	Pulse Repetition Interval
PSK	Phase Shift Keying
RCS	Radar Cross Section
RDRA	Rectangular Dielectric Resonator Antenna
RF	Radio Frequency
SNR	Signal to Noise Ratio
TCXO	Temperature Compensated Crystal Oscillator
TE	Transverse Electric
TM	Transverse Magnetic
VCO	Voltage Controlled Oscillator

Nomenclature

α	Frequency slope
ΔR	Range resolution
Δv	Velocity resolution
$\Delta\phi$	Phase difference
ϵ_r	Relative material permittivity
λ	Wavelength
μ_r	Relative material permeability
ϕ	Angle measured from x axis
ϕ	Phase of signal
σ	Radar cross section
τ	Target induced time delay
θ	Angle measured from z axis
A_{Rx}	Received signal amplitude
A_{Tx}	Transmitted signal amplitude
B	Frequency sweep bandwidth
BW	Bandwidth
c_0	Speed of light
e_{nl}	Frequency sweep linearity
f_b	Beat frequency
f_c	Carrier frequency
f_D	Doppler frequency (Doppler shift)
f_R	Receive frequency
f_s	Sample frequency
f_t	Transmit frequency
f_τ	Signal propagation time frequency
$f_{bd,u}$	Beat frequency down and up
f_{npm}	Cylindrical dielectric resontor antenna resonant frequency
$G_{D,FFT}$	Processing gain
G_{Rx}	Gain of receive antenna
G_{Tx}	Gain of transmit antenna
$K\phi$	Gain of phase frequency detector
K_{vco}	Gain of voltage controlled oscillator
Kd	Gain of Charge pump
L_r	Total receiver losses

N_s	Number of signal samples
N_{FFT}	Number of signal samples after the Fourier transform
P_{Rx}	Radar received power
P_{Tx}	Radar transmitted power
R	Target range
R_b	Blind range of pulse radar
S_r	Received power density
S_t	Transmitted power density
S_{Rx}	Received signal
S_{Tx}	Transmitted signal
T	Time duration
T	Waveform duration of one ramp
T_0	Reference temperature
T_p	Waveform duration of transmit pulse
T_{chirp}	Waveform duration of chirp/fast ramp
T_{CPI}	Waveform time duration
T_{rec}	Recovery time duration of the pulse radar
V_t	Target velocity
V_{ua}	Unambiguous velocity
X'_{np}	Bessel function of the first kind derivative
X_{np}	Bessel function of the first kind
a	Cylindrical dielectric resonator antenna radius
c	speed of propagating signal
D	Decimation factor
d	Cylindrical dielectric resonator antenna thickness
F	Noise figure
k	Boltzmann constant

List of Figures

List of Tables

List of Definitions

The parameters which are defined in this section are used throughout this thesis.

Antenna

MCPCB
A Philips Hue aluminium core PCB with traces and LEDs placed on top of it. This plate serves as ground plane for the antenna and is shaped in a particular way as shown in the thesis.

Radar Parameters

During this thesis the velocity of a target is defined to be negative when the target is approaching the radar.

Signal to Noise Ratio(SNR)
The Signal to Noise Ratio (SNR) is defined as the ratio of the received signal power divided by the noise power, in this case the noise power is defined as the thermal, circuitry and environmental noise. For the total signal power the processing gain obtained after signal processing is included in the SNR ratio.

Radar Performance
Since the radar is used as human motion detector by comparing the SNR to a certain (variable) threshold value, the minimum SNR needed for a detection is used to describe the radar performance. Therefore a radar performance is better when the minimum SNR is lower while the radar system is still able to detect a target.

Transmitter
The transmitter generates defined waveforms or pulses to be sent and applies amplification of the signal to provide adequate range. The carrier source is defined by the synchronizer.

Receiver
The receiver is set on the range of transmitted frequencies, amplifies the returned signal and transforms the received signal into video format. To get the greatest target information (range, speed, direction), the receiver must add minimum excessive noise to the signal.

Synchronizer
In case of a pulsed radar, the synchronizer regulates the rate at which pulses are sent, it defines the Pulse Repetition Frequency (PRF).

Data Recorder
The data recorder obtains the data (mixed for a two-antenna system) and sends it to the processor for data processing.

Processor
The processor uses signal processing to obtain the relevant data for target detection. The way of processing differs for different type of radar systems.

Display
The display presents the processed data for the user to interpret if there is a target of interest present or not, this can be a computer. For the lighting application the display is not of relevance and the processor will send the presence detection data towards the lighting control system.

Circulator
The circulator alternates between received and transmitted signal to the antenna and are used as a type of duplexer. It protects the receiver circuitry from the transmitted signal by not allowing

direct signals from one to the other. Circulators are used in mono-static radar systems with one antenna to separate the receive signal from the transmitted signal. An alternative that could be used instead of circulator is a transmit-receive switch (TR switch) which alternates between the transmitter and receiver connection towards the antenna. However, by using a TR switch, the system can only receive or transmit which does not agree with the continuous presence detection needed for lighting applications.

Mixer
The frequency mixer mixes the transmitted and received signals to obtain the frequency sum and difference. Since the frequency difference obtains the target information (beat frequency in FMCW), the frequency sum signal is filtered out.

Rx,Tx Antenna
The transmit (Tx) and receive (Rx) antenna radiate and obtain electromagnetic energy.

Phase Locked Loop (PLL) Parameters

Frequency Range
The frequency range equals the range that is generated by the VCO. For commercial radar applications this frequency range is often limited by the ISM bands. In this case the frequency range is limited to the 24.125 GHz ISM band with a bandwidth of 250 MHz.

Frequency Resolution
The frequency resolution is the smallest increment in frequency possible and is limited by $\frac{f_{VCO}}{N}$ and $\frac{f_{VCO}}{N+K/F}$ for a integer-N PLL and fractional-N PLL, respectively.

Phase Noise and Jitter
Ideally a clock signal would generate a pure sine wave, however in reality all clock signals are prone to phase-modulated noise which spread the clock signal to adjacent frequencies. These adjacent frequencies results in phase noise sidebands. The phase noise represents the amount of signal power (dBc/Hz) at an offset frequency from the carrier frequency in frequency domain. On the other hand, phase jitter is the time domain instability of the clock signal and can be seen as a random variation in clock signal edges.

Spurious Signals
Spurious signals is a measure of the discrete, deterministic and periodic interference in the noise spectrum. An example of spurious signals is the interference in the noise spectrum caused by the phase detector with high levels of transient noises. The Phase Frequency Detector (PFD) noise is superimposed on the control voltage for the VCO which then modulates the VCO output.

Loop Bandwidth
The loop bandwidth influences the phase noise, settling time, spur suppression. Furthermore it also determines the PLL controllability and stability and which makes the loop bandwidth a critical design parameter of the PLL.

Phase Margin
The Phase Margin (PM) is a measure of stability and is defined as the offset between the open loop phase and 180 ° at the unity(0 dB) open loop gain frequency. Usually the PM needs to be at least 40-45 ° [14] and is typically between 45 - 70 ° [15].

Settling Time
The settling time is a measure of the time needed to re-tune the VCO frequency from one to another. Since the frequency resolution is limited, the frequency is considered as locked within a defined margin(i.e. ± 1 kHz) from the desired frequency.

Lock Range
Range of frequencies where the PLL can lock when it is not locked.

Capture Range
Range of frequencies where the PLL can lock after a lock has been achieved.

1 Introduction

1.1 Motivation of the research

As remote sensing instrument radar has developed considerably over the last 70 years and has become widely used not only in the military domain, but also for aerospace applications, air traffic control, weather services and speed control. Lately, radar is becoming more widely used in the automotive industry [16, 17], medical equipment [18] and for everyday home products, reaching more users and markets. The radar became small in size, easy to handle and low cost which makes it viable for implementation in commercial products. The biggest drawback of the modern radar technology is that depending on application, radar requires specific design, optimization and adaption which makes radar development a time-consuming task.

Current lighting systems often use a separate presence detection unit where users must place these units in every room where the light bulbs are present. From a social point of view, a separate detection unit needs batteries, must to be placed visibly in every room and should be pointed at a room entrance. The human presence detection in lighting systems should aim to be invisible to the user such that the design is compact and visibly attractive when placed in a home environment.

This thesis focuses on integrating a radar system in an indoor lighting product which functions as human presence detector. The use of a radar instead of other presence detection systems such as passive infra-red, ultrasound, Time of Flight or a camera system is because of its small size, accurate range and/or velocity resolution and less to no privacy concerns. Another advantage of the radar is the possibility to look through laminates which is not possible with other type of sensors. Therefore, the radar could be implemented inside the light bulb without being visible to the user. Furthermore, light bulbs are commercial products which require the radar system to be low cost therefore the manufacturing difficulty and material costs should also be taken into account.

Considering high-end modern light bulbs with many electronic systems/ functions implemented, radar integration in such a device is a challenging task. The major challenge is integration of the radar antenna in the bulb. There is often a lot of metal present around the bulb (e.g. metal structures), the bulb housing is often almost fully closed and the radar system should be very compact to fit in the bulb housing. Metal is likely to influence the radiation pattern of the radar system since electro-magnetic waves cannot penetrate through metal.

Some experiments have been done by using simple monopole antennas integrated on the LED surface covered by the bulb cap. The limited space on the LED surface is the reason of using wire antennas over patch antennas which require more space in general for implementation. However, these simple wire antenna solutions block the lighting illumination pattern causing shadows in the cap which is unacceptable for a lighting product. The detection system thus should not interfere with the lighting illumination pattern or its communication with the current main control system to obtain the integration of the detection unit in the light bulb. For this to be realized the antenna needs to be optical transparent which makes the dielectric resonator antenna a suitable candidate for this application. The motivation of this thesis is to investigate possibility of implementing a low-cost transparent dielectric resonator antenna in an enclosed light bulb housing.

1.2 Antennas Integrated in Light Bulbs: Existing Approaches

Transparent Antennas

To make a part of an antenna optical transparent one could consider two types of antennas that are described in literature. The first transparent antenna is based on a patch antenna [19] or monopole [2] with transparent conductive films (e.g. a silver grid layer) instead of metal structures and see through substrate.

Saberin et al. [19] explored an optical transparent patch antenna made of transparent conducting oxides and discussed the challenges that come with such an antenna. The transparent patch antennas were however limited by intrinsic properties which made these antennas not suitable for commercial products. These antennas require a clean room for fabrication of the thin mesh layer on top of the see-through substrate and have to be mounted vertically which is a delicate task which cannot be applied in a commercial manufacturing process which uses 2D pick and place machines. Another optically transparent antenna was made by Hautcoeur et al. [2] where an optically transparent meshed silver/titanium bilayer was printed on a glass substrate. The advantage of this antenna is that it lacks the losses due to skin depth effect in contrast to multilayer antennas made from both transparent material and conductive material. The above-mentioned antennas both require thin layers which can be manufacturing intensive and hence costly. Furthermore, these antennas suffer from low gain and efficiency since there is still some lossy metal present and because of the poor transparent conductors [19].

The second type of antenna is the Dielectric Resonator Antenna (DRA) which consists of a non-conducting resonator and feeding mechanism with a relatively high efficiency compared to the example transparent patch and monopole described above. The DRA is a resonant antenna fabricated from low loss microwave dielectrics and is mostly used at microwave frequencies. A low-loss microwave dielectric material is fed resulting in a resonant frequency which is predominantly a function of the size, shape and material permittivity.

Dielectric Resonator Antenna

The DRA is a suitable option for lighting applications because the resonator part can be made of different transparent materials including glass [20, 21] and plastics [22, 23]. Leung et al. [24] demonstrated the use of a transparent glass resonator also as a lens for photo-voltaic sources and showed in another study [20] that the influence of soldered LEDs did not influence the antenna performance significantly.

The DRA has more attractive features, including a small antenna size with a main dimension proportional to $\frac{\lambda_0}{\sqrt{\epsilon_r \mu_r}}$ [25], a high radiation efficiency due to minimal conduction losses and relatively large bandwidth. By decreasing the dielectric permittivity of the resonator, the bandwidth can be further increased as shown by Yarovoy et al. [22, 23] and changing the operation mode in the resonator resulted in different antenna radiation characteristics [12]. With many possible feed options the resonator operation mode can be changed and adds a possibility to excite the DRA with existing technologies. The design freedom makes the DRA a good candidate for the lighting application.

1.3 Objectives of Research

To the best of the author's knowledge a study on a low dielectric DRA integrated in a bulb environment has not yet been covered in literature. Leung et al. [20, 21] are the only ones who considered transparent DRAs before, using glass resonators with dual function. What these studies did not cover is the implementation of a plastic (low-cost) dielectric resonator antenna in an enclosed bulb environment. This thesis will therefore focus on a low dielectric permittivity DRA made of transparent polycarbonate and its ability to function as a radar-based presence detector integrated a light bulb. The shortcomings to this problem are studied during this thesis which include the influence of antenna parameters of the DRA by an enclosed light bulb, the sensitivity of a DRA for manufacturing and material tolerances and the possibility to implement such an antenna together with a radar system in a light bulb housing.

This thesis makes three main contributions to knowledge:

- Investigate integration of DRA into light bulb and influence of bulb environment on DRA parameters;
- develop a radar model for human presence detection using DRA and determine requirements to DRA in order to successfully detect human presence with this radar;
- experimentally verify both radar model and DRA model developed

1.4 Outline of Thesis

The organization of this thesis is as follows. The second chapter gives a brief overview of the lighting system environment and some preliminary related work on optically transparent antennas. The third chapter examines the use of radar for human presence detection, challenges that are likely to be present and uses a radar model for human presence detection simulations. The optical transparent dielectric resonator antenna is then described in more detail in the section thereafter including simulations and a prototype for validation. The development and design of the total radar system is included hereafter, which describes the design choices made for the total system. Afterwards a section is dedicated to the measurement and validation of the proposed radar system. Each part of the radar system is tested for its functionality. The last section will conclude the thesis with the results obtained during this thesis and a conclusion will be drawn. Some future work recommendations are also presented in the last section. In the appendices parts of the measurement results are shown which were too comprehensive to include in this thesis main body.

2 Antenna Integration in Light Bulbs

Nowadays, home lighting systems are slowly getting rid of using traditional switches in every room to turn them on or off. To have a more convenient and energy efficient way for users to operate the light bulb, human presence detection sensors are used which turns the bulb on at room entrance and turns it off while no one is present. These detection units however must be placed facing the room entrance which does not makes the design visible attractive.

To make the lighting system more attractive in its environment, the presence detector can be integrated into the light bulb. However, this is not straightforward since the light bulb environment is known to be quite challenging. These challenges include a metal enclosed housing, fully occupied LED board, enclosed cap for the light bulb and memory and computational power restrictions on the lighting system, which are further elaborated in the next sections.

2.1 Application of an Antenna Integrated Lighting System in an Indoor Home Environment

The home environment is a complex application environment for a presence detector system since the bulb can be used in all kinds of configurations and within different lampshades. A lampshade made of metal compositions for example will interfere with any Doppler based presence detector applied inside the bulb. In addition, the distance from the detector and a person can vary a lot. A person's movement can be very close to the light bulb which makes target radial velocity detection by a presence detector challenging. Unless the antenna radiation pattern is comparable to a perfect isotropic antenna, it is difficult to measure the speed and range of a person under all angles. During this thesis the focus will be on the home environment with bulb positions A, C and D as shown in Figure 1b, due to fewer degrees of freedom in orientation of the bulbs. Since these positions are all mounted in a ceiling the angle that should be at least covered is 120 degrees as depicted in Figure 1a in order to cover the area that is below the light bulb. Situation D in

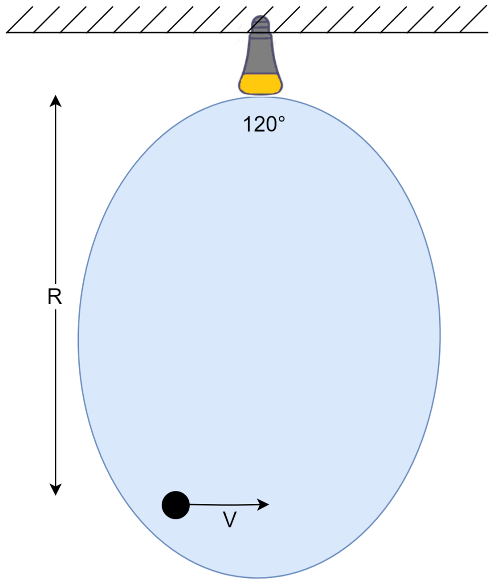

(a) Presence detection system with 120 degrees viewing angle and target range and velocity depicted

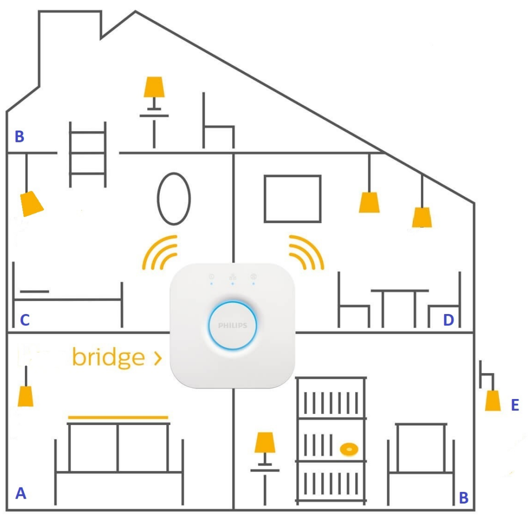

(b) Some bulb positions in a home environment, adapted from [26]

Figure 1: Antenna system in lighting applied and the total home environment depicted

Figure 1b shows multiple Hue bulbs operating near each other which causes interference between transmitted and/ or received signals. The presence detectors of these bulbs will continuously detect each other because of interference between the transmit and receive signals. To avoid these situations one presence detector in a bulb could be turned off by a bridge which connects all light bulbs in a home environment and has information about their location in different rooms.

In a home environment with humans as targets of interest give boundaries on the detection speed and range. A person walks on average about 1.5 m/s and can have a speed up to 4 m/s when sprinting. For motion detection purpose only, human models do not have to be overly complex since gait is not of main interest. It can be assumed that a person has an average Radar Cross Section (RCS) of 1 m^2 when a person is moving radially towards the detection system. However, if the bulb is placed on a ceiling the average RCS for a person is expected to be lower than 1 m^2 since the movement of the person is not towards the presence detection system which makes the radial velocity of a person towards the detection system smaller. The minimum distance between the presence detector and a person can be defined when the bulb is mounted into the ceiling facing downwards. When assumed that a ceiling has a minimal height of 3 meters and the tallest person living on earth equals 2.51 m [28], the minimum required measuring distance equals 49 cm.

In addition, if a person is sitting behind a desk and typing, the motion is very limited which makes the person invisible for a motion detector. With a motion detector as used for current light bulbs systems, light will be turned off when no motion is detected after some time. A person working behind a desk is likely to exceed this 'on' time and will not be detected when the motion sensor checks presence again. To be able to detect an almost static person, both range and speed information is needed. Radar systems are a widely used solution for obtaining this information. They are relatively simple and can be made low cost for a commercial lighting product. The radar is discussed in a later section in more detail.

If a person enters the detection range of the system, light is supposed to turn on within a specified response time and with a certain distance. The total system response time (including turning the light bulb on) is set on 500 ms which is a typical specification for lighting applications. Taking the system startup time into account of 100 ms at max, the presence detection system operation can use the remaining 400 ms for data processing and detection. After presence detection of a target, the light bulb can be kept on for 5 minutes. During these 5 minutes the continuous detection system can be turned off to save power and after the 5 minutes passed the detection should be turned on again to check if there is still someone present. If no person is detected the lights can be turned off afterwards. What should also be taken into account is the power consumption of the bulb in stand-by which could be very high if a lot of data is processed for the presence detection system. It is therefore preferred to limit the amount of signal processing for the presence detection system. For a typical presence detection like a frequency modulated radar, the Fourier Transform to convert from time domain signals to the frequency domain spectrum uses most of the computing power and memory. The fast Fourier transform (Fast Fourier Transform (FFT)) is widely used because of its speed and simplicity but is computationally expensive. A different type of transform that can be used to limit the number crushing for radar based presence detection systems is based on the Chirp-Z transform. Both the FFT and Chirp-Z transform are more described in detail in Appendix B.

2.2 Connected Lighting System Environment

Typical high-end light bulbs have micro-controllers available in the light bulb itself to control the lighting and to communicate with the outside world. Figure 2 shows the bridge functioning as the heart of the lighting system, only allowing communication from light bulb to bridge using ZigBee. The potential implemented presence detection system however will run continuously including a lot of signal processing as part of the presence detection. Computing power and memory storage is needed at a certain point in the total lighting system where the conversion from time to frequency domain is done. Looking at the current system there are several places where the signal processing could be done using a micro controller. Ideally the light bulb itself can handle all this signal processing which eliminates any problems with the communication speed and occupancy between the light bulbs and bridge. To have the total presence detection system operating in the light bulb itself, enough memory in the light bulb micro-processor is needed for signal processing. However, not only the detection electronics will need memory for the signal processing on a micro-processor in the light bulb, also the communication from light bulb to bridge and vice versa should not change. Typical lighting systems use small microprocessors with very limited memory and computing power available, leaving minimal to no space left for presence detection signal processing.

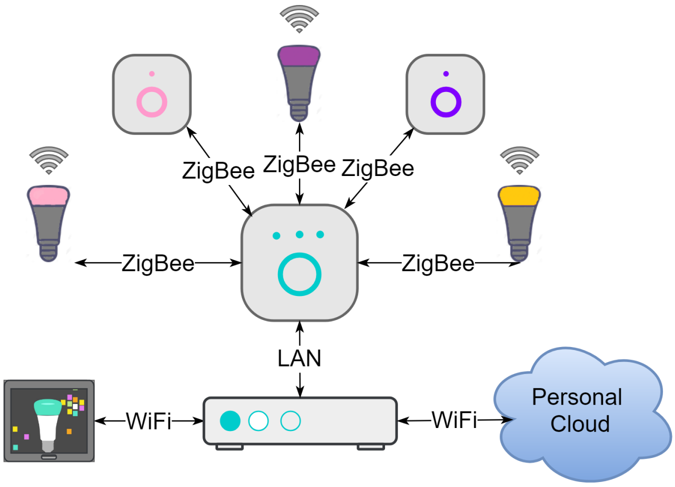

Figure 2: Connected lighting with router and cloud included

This problem can be solved by moving all computations to the bridge itself or in the cloud because both have more storage space and computing power. However, the bottleneck of this solution is the ZigBee communication which only allows sending or receiving and is likely to be occupied most of the time by the lighting control system. To cope with this problem, data should be saved in the bulb until the ZigBee channel is available for transmission. However, this will solution needs even more memory in the bulb itself to store the data until it can be transmitted. If the ZigBee transmission is not available yet and the bulb memory is full, the data in the bulb itself will be overwritten and data will get lost (which might contain detected presence data). Therefore, the presence detector integrated in the light bulb should take the limited processing power and memory usage into account.

2.3 Fully Enclosed Bulb Environment

Lighting applications can very a lot between the design of the bulbs and their layout, however, some typical similarities are present in light bulbs that are challenging for an antenna implementation. One of these challenges is the fully closed (metal) bulb housing (shown in Figure 3b) for Ingress Protection Marking (IP) rating agreement and heat-sink application, which makes it difficult for the presence detector to operate through. Figure 3b also depicts the L-shaped slot antenna in the aluminium housing which is present for the ZigBee communication. Making extra slots in the light bulb housing would be a solution to let electro-magnetic waves escape to the environment, however this will disturb the heat distribution. The heat distribution is of uttermost importance because the temperature in a typical light bulb can get up to 100°C at the power circuitry which should be distributed to the outside of the light bulb as quickly as possible. In addition, rapid temperature changes in the light bulb are quite common which ranges from room temperature to the 100°C in a few seconds. By making cuts in the light bulb housing, the heat transfer will be relatively slower due to less metal present and might overheat the inside circuitry. Thus, placing an antenna on the Light Emitting Diode (LED) surface under the cap is the most likely solution. The LED surface board is also called Metal Core Printed Circuit Board (MCPCB) and is shown in Figure 3a.

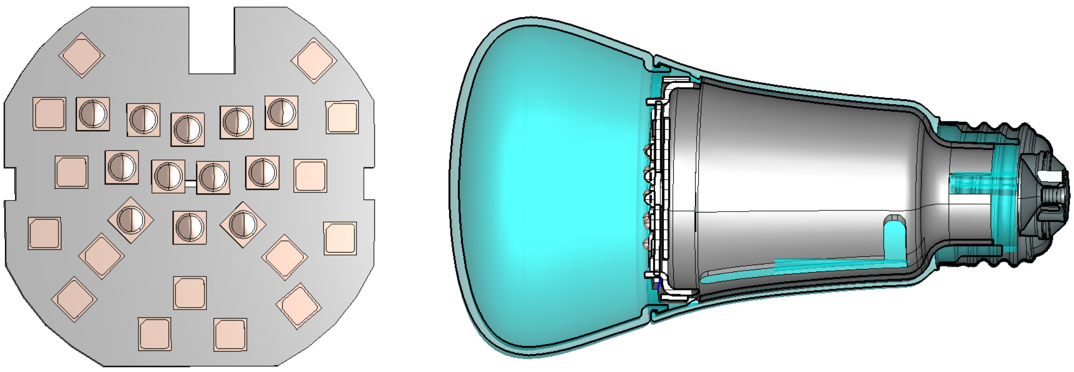

(a) MCPCB

(b) Cross section bulb

Figure 3: MCPCB with white LEDs mounted on the circumference and colored LEDs on the center in (a) and (b) shows the cross section of the total bulb without internal circuit present

A typical lighting application that would be suitable for the use of a presence detector, is the Hue White and Color bulb. The Hue bulb is chosen as application since challenges as mentioned above are all present. The considered bulb has a very limited space for the presence detection system application since it already consists of electronics including a ZigBee communication with a bridge ('heart of the lighting system') and the LED power system. Figure 3b details the cross section of a typical Hue light bulb without internal circuitry. The internal circuitry occupies the length of the bulb and leaves the upper part available for a presence detection circuitry. The LED surface of the Hue bulb, is depicted in Figure 3a consisting of an aluminium plate with traces and LEDs on top, which makes it challenging for an antenna implementation without blocking visible light. The traces are linked by a connector placed in an off-centered cutout at the top of the MCPCB and occupy most of thes MCPCB surface. The white and colored LEDs are placed in a color blending optimized position near the MCPCB edge and in the MCPCB middle, respectively. A varying MCPCB over the years is very common because of evaluation on the LEDs or different LED packaging due to manufacturer changes. It is thus of importance that the antenna is not too sensitive for the LED placement.

Integrating an antenna on the MCPCB should not interfere with the LED placement and LED color blending. Because of limited space on the MCPCB antennas which require ground plane clearance are not suitable and therefore not considered during this thesis. Simple antennas like a patch, a planar inverted-F antenna (PIFA) or a meandered PIFA which all require ground plane clearance around the antenna is likely to not fit on the MCPCB. Especially the PIFA antenna is less suitable for this application since these antennas are known to be heavily influenced by ground plane changes. Some experiments have already been done using simple monopole antennas on the MCPCB, which were preferred over patch antennas because of the limited ground plane area needed for implementation. These simple wire antenna solutions however are high in profile which block the lighting illumination pattern. The resulting illumination pattern has shadows that can be observed in the cap for users and is thus unacceptable for a lighting product. The antenna should therefore not interfere with the lighting illumination pattern, which makes transparent antennas interesting candidates for this application. These transparent antennas are considered in more detail in the next section.

2.4 Existing Approaches on Optically Transparent Antennas

Optically transparent antennas are described recently with only a few contributions in literature linked to a realistic application. One possibility of obtaining such an optically transparent antenna, is to use transparent conductive layers deposited on see-through substrates and another possibility is to use transparent dielectric resonator material together with a typical antenna feed network. Another possibility is a dielectric resonator antenna which uses an optically transparent resonator. Both approaches are elaborated in the next sections.

2.4.1 Antennas Made of Transparent Conductive Materials

The optically transparent antenna made of transparent conductive material deposited on see-through substrates are mainly studied in recent years. Different transparent conductive materials were reported by studies including: silver meshed grid layer (AgGL) [1, 2], silver transparent conductive coated polyester (AgHt) and coating by using an ultrathin copper layer, Indium Tin Oxide (ITO).

AgGL uses a thin silver grid layer film on a transparent substrate which is studied extensively by Hautcoeur et al. [1, 2], who introduced different Ag meshed based monopole antennas. These antennas are equal in size as traditional wide-band monopole antennas, but are mounted vertically to limit the ground plane space needed as shown in Figure 4a. Many of the transparent antennas are made for lower frequencies (up to 10 GHz) to keep their size reasonably large for easier prototyping and implementation. Only one 60 GHz AgGL-based transparent monopole antenna was described by Hautcoeur et al. [1] which resulted in a few millimeter sized antenna. A microscope picture of this antenna is shown in Figure 4b which is fed by a coplanar probe. To keep the transparency high, the thin-film deposition are typical on the order of 100 nm to 2 μm [19]. However, when these depositions are thinner than skin depth (see Equation (1)), the effective resistance of the conductive layer increases as a function of thickness.

$$\sigma = \sqrt{\frac{2}{\sigma \omega \mu}} \tag{1}$$

There is thus a trade-off between a thick metallization to prevent losses from the skin depth and obtaining a high transparency.

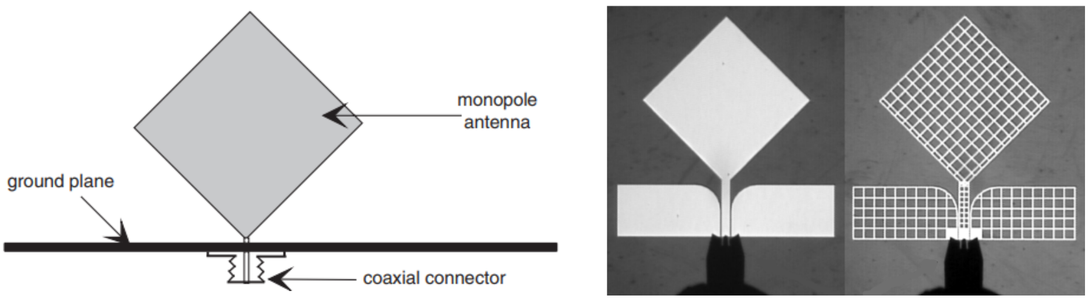

(a) Probe-fed monopole antenna

(b) Coplanar-fed monopole 60 GHz antenna

Figure 4: Probe-fed and coplanar-fed monopole antennas, obtained from [1, 2]

Colombel et al. [29] investigated another type of transparent monopole antenna based on ITU/Cu coated polyesters (AgHt) which were fabricated using RF sputtering. A thin (1μm) copper coated polyester transparent antenna had an improved optical transmittance around 60% compared to the 1 nm coated sample, while the gain was drastically low compared to the traditional (non-transparent) monopole. The thin copper coating was too thin in terms of skin depth, causing a significant loss in gain. Moreover, it was also reported that the very thin copper coating offers poor hardness and are sensitive to mechanical stresses which makes this type of antenna unsuitable for industrial applications. Another 1 μm ITO based layer was used in the same research which however also suffered from poor gain. The losses regarding the skin depth improved significantly, however the ohmic losses were dominant for this type of antenna. Compared to the copper coating the ITO based antenna had a high hardness and better optical transmission (close to 80%). A last test was carried out on a three-layer ITO/Cu/ITO coating which compromised between high transparency and performance. These monopoles were all mounted vertically with a corner fixed on a probe connector.

The antennas as studied in recent years based on transparent conductive material deposited on see-through substrates are an interesting option for implementation in a light bulb. The antennas are very thin which makes implementation on a limited space LED surface ideal. They also have a very wide detecting angle (because of monopoles far field radiation characteristics) and can be implemented for mass production considering the possible low cost of IC design when produced in large volumes. However, to get such layered antennas dedicated production methods such as RF sputtering must be applied in a clean room. Typical lighting companies do not have clean rooms available which makes the introduction of such an antenna very costly. In addition, these antennas are very thin which makes integration in a LED bulb a very delicate task. Current lighting LED boards are typically fabricated using pick-and-place machines and solder paste/ glue for attachment. For an optically transparent vertical placed monopole, the pick and place machine must be very accurate and with positioning possibilities in three dimensions. Therefore the transparent conductive material antenna is not considered for the light bulb application.

2.4.2 Dielectric Resonator Antennas

Dielectric resonator antennas (DRA) have been studied since 1983 by Long et al. [30]. In recent years the study on DRAs has increased due to attractive features including the size, high radiation efficiency, relatively low cost and relatively large bandwidth. The antenna size of a DRA can be scaled down roughly by a factor of $\frac{1}{\sqrt{\epsilon_r}}$, which made antenna designers in the late eighties and nineties work with many high dielectric permittivity ($\epsilon_r \approx 20 - 100$ [12]) ceramics. However, using ceramics limits the design flexibility when complex shapes are desired and is prone to chip and fracture during manufacturing. This makes the manufacturing process delicate, time consuming and hence expensive which does not satisfy the requirements for a commercial lighting product.

Another advantage of the DRA is the design freedom in using different feed structures. Different excitation structures for the DRA have been studied over the years. Typical feed methods are based on a coaxial probe, patch, slot or microstripline. The coaxial probe can be inserted into the resonator as shown in Figure 6a which requires a precise drilled hole in the resonator to avoid air gaps between the feed and resonator to not influence the antenna performance because of the dielectric permittivity difference. To avoid this problem, an aperture coupled feed can be used as shown in Figure 6b. For lighting applications the DRA feed should have a low profile to avoid interference with the illumination pattern. A probe feed will have a relative high profile which is likely to block the color blending of the LEDs. The patch feed is a low profile solution, but needs ground plane clearance to function. Therefore a microstripline, (grounded) coplanar waveguide or slot are most suitable for the integration of a DRA on a LED board. The integration of the dielectric resonator antenna in the light bulb production process requires a bit of adhesive and a 2D moving pick-and-place machine places the resonator on the LED board, which is easier compared to the transparent conductive material antenna.

The dielectric resonator antennas can be divided in the simple shaped (easy to fabricate) and complex resonators. Simple shapes like the cylindrical and rectangular DRA are relatively easy to manufacture while hemispherical antennas are in general more difficult to fabricate if a similar accuracy is desired. These shapes are described in the next subsections and their suitability for the application is discussed.

Cylindrical DRA

Many studies [3, 12, 25, 30–33] have been published on the simple shaped Cylindrical Dielectric Resonator Antennas (CDRA). Long et al. [3] carried out an analysis for a probe-fed CDRA using

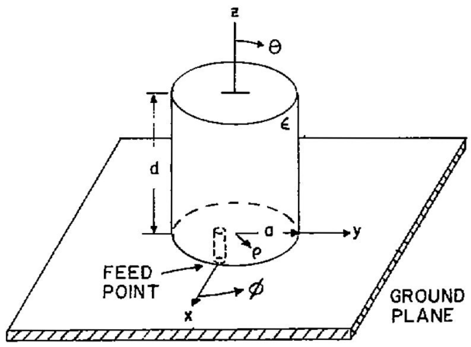

Figure 5: CDRA geometry and parameters, shown in [3]

the magnetic wall theory. This theory ignores the probe feed and assumes the surfaces of the DRA to be perfect magnetic conductors, resulting in an uniform cylinder. The geometry of the used CDRA is shown in Figure 5 [3] with the parameters also depicted.

The resonant frequency for Transverse Electric (TE) and Transverse Magnetic (TM) can be described by the following equation [3, 31]

$$f_{npm} = \frac{c}{2\pi a\sqrt{\epsilon_r \mu_r}} \sqrt{\left\{X_{np}, X'_{np}\right\}^2 + \left\{\frac{\pi a}{2d}(2m+1)\right\}^2} \quad [Hz] \tag{2}$$

where X_{np} is used for TE mode, X'_{np} for TM mode and X_{np}, X'_{np} stand for the Bessel functions of the first kind and its derivative, respectively. The dimensions of the CDRA in Equation (2) are given by the radius a [m] and thickness d [m] and $(n,m,p) \in N^3$. The fundamental mode for the CDRA is the TM_{110} mode which is often the mode of interest because it resonates at the lowest resonant frequency and its radiation pattern represents a magnetic monopole. Equation (2) is presented [3] to be accurate within a few percent from the actual resonant frequency and is also tested to materials with lower dielectric permittiviteis (4.5). Other more simple formulae that are derived for cylindrical DRAs are only valid for higher permittivity resonators (>10) and are therefore not considered in more detail.

Mongia et al. [12] investigated different resonating modes and corresponding radiating characteristics of CDRAs. They divided possible modes in a DRA into three types: transverse electric (TE), transverse magnetic (TM) and hybrid (HE or EH). The CDRA modes were defined as $TE_{0pm+\delta}, TM_{0pm+\delta}, HE_{npm+\delta}$ and $EH_{npm+\delta}$ where δ ranges between 0 and 1 and n,p,m are natural numbers. The indexes n,p,m are used where n denotes the azimuthal variation of the fields, p represents the order of variation of the field along the radial direction and index m denotes the order of variation of fields along the z-direction. Mongia et al. [12] have shown that the different resonator modes in Table 1 have far fields comparable to dipoles and quadrupoles.

Table 1: Mode features of an isolated CDRA, obtained from [12]

Mode	Symmetry plane	Far field	Orientation multipole
$TE_{01\delta}$	Mag. wall	Magnetic dipole	vertical
$TE_{011+\delta}$	Elec. wall	Magnetic quadrupole	vertical
$TM_{01\delta}$	Elec. wall	Electric dipole	vertical
$TM_{011+\delta}$	Mag. wall	Electric quadrupole	vertical
$HE_{11\delta}$	Elec. wall	Magnetic dipole	horizontal
$HE_{21\delta}$	Elec. wall	Magnetic quadrupole	horizontal
$EH_{11\delta}$	Mag. wall	Electric dipole	horizontal
$EH_{21\delta}$	Mag. wall	Electric quadrupole	horizontal

Rectangular DRA

A Rectangular Dielectric Resonator Antenna (RDRA) offers better design flexibility compared to a cylindrical one because of the three independent geometric dimensions. Figure 6a gives an example of a RDRA fed by a microstrip which is attached to the RDRA surface. The RDRA is more difficult to analyze theoretically because of edge-shaped boundaries which complicates the evaluation of modal coefficients.

Different methods were used in the past to analyze the RDRA including Finite-Difference Time-Domain (FDTD) [34] to approximate the radiated field and the dielectric waveguide model [35]. The first is especially used for complex resonator geometries and is more accurate but also time consuming and memory intensive when antenna parameters have to be optimized. The latter assumes the fields in the waveguide to be sinusoidal while the fields outside the guide are exponential declining. When the RDRA is mounted on a ground plane only TE modes can be excited including its fundamental operating mode TE_{111} resulting in simple equations for the resonant frequency [36]

$$f_{TE_{111}} = \frac{c}{2\pi\sqrt{\epsilon_r}}\sqrt{kx^2+ky^2+kz^2} \quad [Hz], \quad kx = \frac{\pi}{a}, \quad kz = \frac{\pi}{2b} \tag{3}$$

where ky can be obtained from

$$d = \frac{2}{k_y}tanh(\frac{k_{y0}}{k_y}), \quad k_{y0} = \sqrt{kx^2+kz^2} \tag{4}$$

and the related resonator dimensions a,b and d are defined in meters. These formulae however are not tested for very low dielectric permittivity resonator materials as is needed for the lighting application.

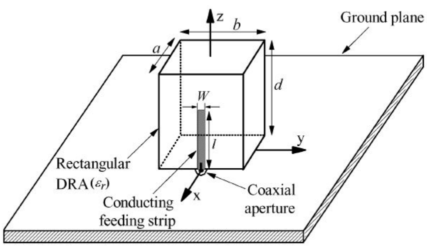

(a) Geometry RDRA, obtained from [37]

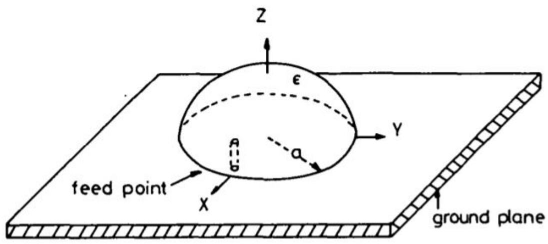

(b) Geometry of HDRA, obtained from [38]

Figure 6: Geometry of rectangular and hemispherical DRA and their parameter definitions

Hemispherical DRA

A resonator shape that might be used as a dual functioning antenna is the Hemispherical Dielectric Resonator Antenna (HDRA) with the option to act as a lens. Many studies have been published on HDRA resting on a ground plane and fed by a probe or aperture feed [21, 24, 38, 39]. The fundamental mode of a probe fed ground plane mounted HDRA is TE_{111} which results in an efficient radiation pattern in the direction perpendicular to the ground plane. The resulting resonant frequency can be obtained with Equation (5), where $k = k_0\epsilon_r^{1/2}$ equals the wavenumber in the dielectric, k_0 is the free space wavenumber and a is the radius of the HDRA, as depicted in Figure 6b.

$$f_{TE_{111}} = \frac{4.775 * 10^7 Re(ka)}{\sqrt{\epsilon_r}a} \quad [Hz] \tag{5}$$

However using a probe as feed would cause shadows in the illumination pattern.

Leung et al. [20, 21, 24] were the first to use a transparent hollow HDRA and a RDRA for optical applications. As resonator glass K9 borosilicate crown was used and the proposed antennas were focused on having a dual function. The hemispherical hollow resonator was used as a lens on top of a solar cell and also as light cover over some LEDs and a rectangular one was placed on top of some LEDs for decorative purposes. With an air-gap in the HDRA the impedance bandwidth of these multilayer antennas can be significantly improved [40]. It was demonstrated that the insertion of a LED inside the resonator of a HDRA on the edges had a negligible effect on the antenna performance [21]. However, these studies did not show the influence of a realistic bulb environment (e.g. a cap, thick ground plane, many LEDs) on the DRA.

2.5 Conclusion

A presence detection sensor makes a lighting system visible attractive to the user and its indoor home environment. The configuration for the home environment is limited to ceiling mounted bulbs with a 120° field of view. With humans as the targets of interest, the detection speed is limited between a 0 to 4 m/s and the minimum detection range is set on 49 cm. The response time of the final system should be within 500 ms, which include 100 ms for the light bulb to turn on, leaving 400 ms left for the presence detection.

Enclosed light bulb housings bring a lot of challenges including: the metal housing, particularly shaped ground plane, rapid temperature changes inside the light bulb from room temperature up to 100 degrees and very limited space for electronics. The metal housing in formed by a metal core Printed Circuit Board (PCB) (MCPCB) occupied with LEDs and traces and a body with an L-shaped slot for ZigBee communication. These LEDs are aligned to optimize the color blending and can therefore not be moved around which leaves limited space for an antenna feed structure. In addition, the antenna should not block the visible illumination pattern which makes the optical transparent antenna an interesting candidate for integration on the LED board.

Two types of optically transparent antennas were considered: transparent conductive materials antenna and dielectric resonator antenna(DRA). Because the ease of manufacturing and the possibility to integrate the antenna in the production process of a light bulb, the dielectric resonator antenna is favored over the transparent conductive material antenna.

Different simple shapes were considered for the DRA resonator with two outstanding shapes for the application. Cylindrical and rectangular shaped resonators are easy to manufacture by machining processes and can be placed on the MCPCB using a pick-and-place machine. The hemispherical resonator must be made by molding and polishing to obtain a smooth surface resonator which makes the resonator production costs higher. With the slot, microstrip or (coplanar) waveguide feed the cylindrical shaped resonator is chosen to mimic the far field radiation pattern of a slot antenna. The slot-like far field radiation pattern is favored over the pattern of a monopole because of the limited back radiation to have more directivity in the field of view of the antenna. In addition, the antenna gain should be higher than 0 dB in the antenna field of view.

3 Radar for Human Presence Detection

Human presence detection can be obtained by a range of technologies which all detect the human body in an area of space. Modern technologies proposed for human presence detection include image recognition, infrared sensors, radar or detection of smart devices. The last detects human presence using Bluetooth, ZigBee or Wi-Fi signals coming from smart devices carried by persons.

A passive detector integrated in a light bulb could be used to detect these smart device signals which is a relatively simple approach because high-end bulbs are already connected and would require only small adjustments to detect these signals. However, for a home environment people are typically not carrying their smart devices with them everywhere which makes this detection technique not suitable.

Infrared (IR) sensors are pyroelectric sensors which measures infrared waves radiating from objects in its field of view. They can be active (motion detectors) or passive (PIR). IR sensors can be applied to a large area and in real time. Furthermore, they pick up movement which can be useful in a variety of circumstances. The strength of the IR sensor also causes a weakness. The use of temperature to distinguish objects cause problems when objects are very similar in thermal energy levels. Also objects near or obscuring each other are not detectable with the IR sensor which is a problem for home environment applications.

Detection using image recognition requires images obtained by cameras for example. The image must be processed to be useful for presence detection which is a quite heavy task. It requires a lot of power for continuously processing lots of images which results in a heavy power consuming system. For a light bulb power consumption, processing power and memory is very limited which makes image processing not suitable. In addition, a camera should be implemented in the light bulb which requires direct line of sight. Considering the light bulb housing there is no possibility to create an opening for such a camera.

The radar is a widely used system in commercial products these days for presence detection which makes it an interesting option for the light bulb application. The original acronym "RADAR" stands for **ra**dio **d**etecting **a**nd **r**anging, although nowadays the term radar is generally used. A radar is an electromagnetic system used to detect a target speed and/or distance with respect to the radar. Electromagnetic energy is radiated into space and energy of reflected signals are monitored and analyzed. The reflected signal is used to determine the direction and distance of the reflecting object. A visualization of the radar principle is shown in Figure 7 where the transmitted waves are shown with solid lines and the target reflected waves with dotted lines.

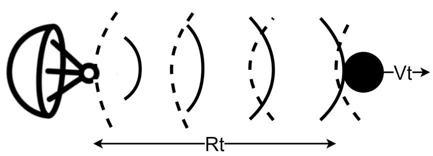

Figure 7: Simplified radar working principle

After receiving the reflected waves at the antenna the radar circuitry will process the data. Figure 8a and Figure 8b depicts two typical radar setups with basic component blocks which are defined in the list of definitions at the start of this thesis. The first uses one antenna for both transmitting and receiving (mono-static radar) and the latter uses separate antennas (bi-static radar). For a mono-static radar the transmit and receive antenna are defined to be one or close to each other (in terms of wavelength) and for a bi-static radar the Tx, Rx antennas are relatively separated far away from each other. The mono-static radar has an advantage of using only one antenna which is suitable for an implementation in a small housing such as a light bulb. The disadvantage of the mono-static radar is the poor transmit-receive isolation which is needed for e.g. FMCW radar. Using a bi-static radar has more transmit-receive isolation because of the separation distance. It also might enhance radar cross section of a target because of the geometrical effects. The disadvantages of such an antenna is the system complexity and the communication needed between the transmit and receive sites. For lighting applications the ground plane area is very limited and antenna spacing will not exceed several centimeters. For Industrial, Scientific and Medical (ISM) band frequencies under 100 GHz this would result in the transmit and receive antenna being relatively close to each other and are therefore considered as a mono-static radar system.

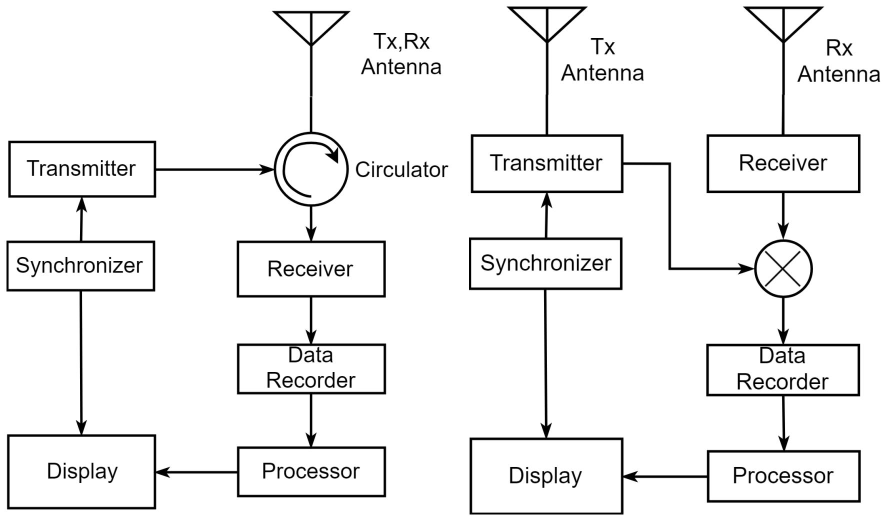

(a) One antenna system **(b)** Two antenna system

Figure 8: Basic blocks of a radar with one or two antennas

3.0.1 Radar Equation

Relevant factors that influence the radar performance can be described by the radar equation which gives the relation between the radar signal power and the target range. The common form of the radar equation is shown in Equation (6) [41, 42].

$$P_{Rx} = \frac{P_{Tx}G_{Tx}}{4\pi R^2}\frac{\sigma}{4\pi R^2}\frac{\lambda^2 G_{Rx}}{4\pi} \quad [W] \tag{6}$$

The first factor on the right is the power density radiated at a distance R [m] from the radar and with P_{Tx}[W], G_{Tx} defined as the transmitted power and gain respectively. The second term consist of the RCS σ $[m^2]$ on the numerator and the denominator accounts for the divergence of electro-magnetic waves on the reflected path. The denominators of the first and second term are identical which takes into account the traveled path of the waves. The third term is also defined as the effective antenna aperture, $A_e = \frac{\lambda^2 G_{Rx}}{4\pi}$ [m], which describes how much power is captured from a given plane wave. The parameters of Equation (6) are depicted in Figure 9. The plane wave in Equation (6) consists of the two first terms combined. The radar equation gives a rough estimate of the target range since losses in real environment are not included and the RCS and minimum detectable signal are statistical in nature.

For a radar implementation in indoor light bulbs a maximum range R of 10 meters is defined. This range is chosen by taking the placement of bulbs in consideration which is often not further than 10 meters away in one room.

The defined range as shown earlier in Figure 1a including the target velocity which ranges from 0 to 4 m/s. The transmit power is predefined by the transmitter chip and the transmit and receive gains of the antennas should be larger than 0 dB in the field of view (120°). With these parameters defined the received power can be obtained using the radar equation.

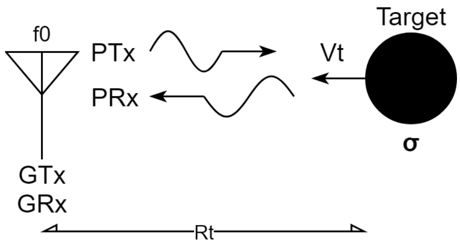

Figure 9: Radar equation parameters visualized

Another way to write the radar equation is by using the SNR where the thermal noise power is defined as [27,42]

$$N = kT_0BFL_r \quad [W] \tag{7}$$

where k is the Boltzmann's constant, T_0 the reference temperature in Kelvin, B the receiver bandwidth in Hz, F the noise figure and L_r the total receiver losses. The resulting radar equation is given by Equation (8).

$$\frac{S}{N} = \frac{P_{Rx}}{kT_0BFL_r} = \frac{P_{Tx}G_{Tx}\lambda^2G_{Rx}\sigma}{(4\pi)^3R^4kT_0BFL_r} \tag{8}$$

Radar Cross Section

The Radar Cross Section (RCS) is a measure of a target's ability to reflect radar signals in the direction of a radar receiver. It measures the ratio of backscatter power per steradian (unit solid angle) in the direction of the radar (from the target) to the power density that is intercepted by the target. The radar cross section of a target depends on its physical geometry and exterior features, the direction of the radar, the transmitted frequency and the target material. The radar cross section σ is defined as [41]

$$\sigma = \lim_{R\to\infty} 4\pi R^2 \frac{S_r}{S_t} \quad [m^2] \tag{9}$$

where S_t represents the power density $[W/m^2]$ that is intercepted by the target and S_r is the scattered power density $[W/m^2]$ in range. If all the incident radar signals on a target would be reflected equally in all directions, then the radar cross section would be equal to the target cross sectional area as seen by the transmitter. In practice, not all reflected signals are distributed equally in all directions and some energy is absorbed by the target.

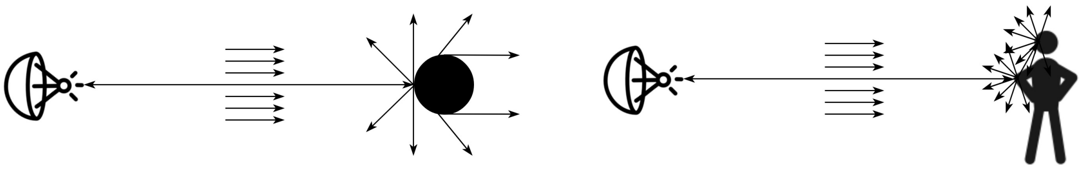

Figure 10: Radar cross section principle for a sphere and a human body

The human body (complex target) consist of multiple reflection points as shown in Figure 10 and the total RCS can be obtained by summing up all contributions of reflection points. It is thus a difficult task to estimate the radar cross section of a complex target and therefore the estimation is often determined by measurements. A method to determine a target radar cross section can be

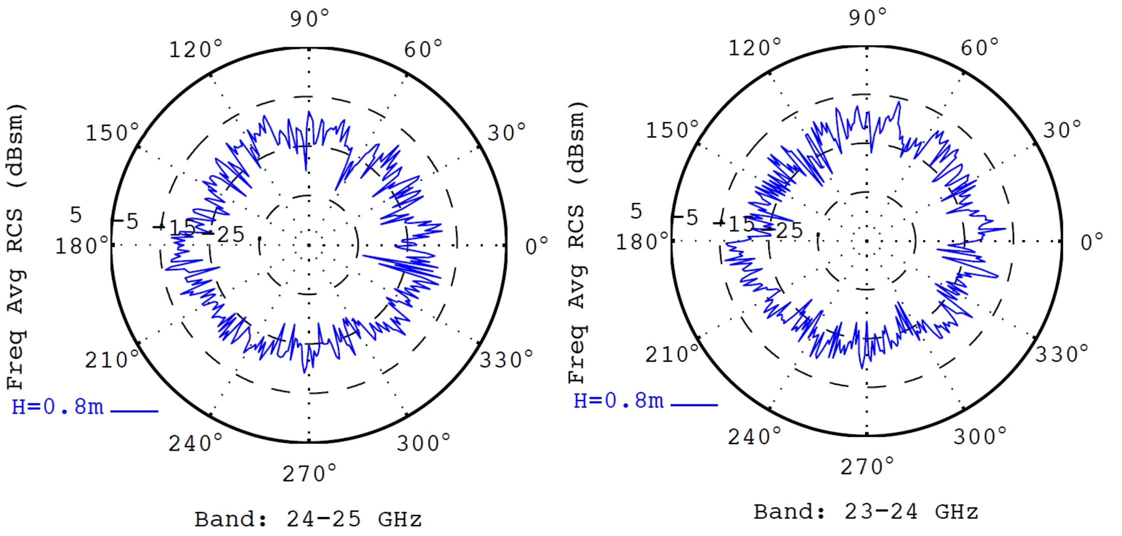

(a) Frequency 24-25 GHz

(b) Frequency 23-24 GHz

Figure 11: Measured radar cross section of a human body, obtained from [4]

done by measuring the backscattered radiation patterns in the antenna far field when the target is illuminated by mono-static microwave radiation and using Equation (9). By rotating the target around and measuring the received electric or magnetic field the RCS around the whole target can be obtained. For complex targets (multiple smaller reflections are present) the RCS is likely to fluctuate a lot at different measurement angles. Some research [4] has been done on measuring the RCS of different human targets and an example is given in Figure 11 [4] which is measured in a frequency range of 24 - 25 GHz. These measurements show that the RCS of a complex target (a human) fluctuates strongly over different measurement angles and with relatively low value. However, the measurements were done on a static human and in most cases, humans are moving with their arms or legs which create more micro-Doppler resulting in a typical RCS values for human of 1. Depending on the orientation of the radar on the person, the RCS of a person typically varies between 0.3 - 1.1 m^2 [27].

3.1 Operating Frequency of the Radar System

The operating frequency of the radar system influences the antenna size. For higher frequencies the antenna size will be smaller due to the wavelength dependency which decreases for increasing frequency ($\lambda = \frac{c}{f}$). Since licensed frequency bands can vary per region/country and are very costly, for the radar operating frequency only Industrial, Scientific and Medical (ISM) frequency bands are considered. Refer to Appendix A for more details on available ISM bands for short range devices (radar) and automotive [13]. The considered ISM bands for this radar are depicted in Table 2.

Table 2: ISM frequency bands for radio-wave sensing systems as stated by the Electronic Communications Committee (ECC) [13]

Band	Center Frequency [GHz]	Bandwidth [MHz]	λ[cm]	type
C	5.8	100	5.2	ISM
K	24.125	250	1.2	ISM
V	61.25	500	0.49	ISM
G/mm	122.5	1000	0.24	ISM

Integration of the radar system in a light bulb with limited space requires small component sizes, including antennas. Typical antennas such as monopoles or dipoles are most efficient when used close to one-fourth and half the operation wavelength. Therefore a higher operation frequency ($\lambda = \frac{c}{f}$) would result in a smaller antenna. The drawback of using a higher frequency of 122.5 GHz or 245 GHz is the limited detection range compared to a low frequency operating system. The lower detection range is caused by propagation loss, atmosphere absorption and refraction and reflectivity on the environment. To compensate for this limited detection, range more power is needed to obtain a reasonable detection range. Another reason to not go up to very high frequencies is due to the manufacturing margins that results in significant errors in terms of wavelength for the operating system.

Regarding the limitation in space, the antenna size around $\lambda/2$ will only fit in a lighting application covered by the bulb for a center frequency of 24.125 GHz and 61.25 GHz. From these two frequency bands the 24.125 GHz band is selected for the radar design since it is less prone to atmospheric losses and gives a reasonable trade-off between the detection accuracy and power consumption.

3.2 Radar Types

Radars can be divided into two different types: primary and secondary. Secondary radars emit pulses and listen for a special answer of digital data emitted by an aircraft transponder. Since this thesis focuses on lighting application secondary radars are not of interest. Primary radars work on reflections of all kinds and are therefore considered during this thesis. The primary radar can be divided regarding the type of transmitted waveform: continuous or pulsed. The former transmits and receives a signal continuously and the latter only transmits signal during a certain time interval and receives signals in the residual time.

Regarding target detection techniques the pulsed radar can be differentiated in Moving Target Indicator (MTI) or Doppler. The MTI radar distinguishes signals from fixed or slow-moving unwanted targets and retain for detection from moving targets. Since the lighting application also must be able to detect slow moving/almost fixed targets, e.g. person behind a desk typing, the MTI is not suitable for the lighting application. The pulsed Doppler radar transmits short and powerful pulses in a short period and receives the echoes in the silent period afterwards. It uses the phase change in a series of pulses to determine the frequency shift.

The continuous transmitting radar can be divided in modulated and unmodulated forms. Unmodulated Continuous Wave (CW) radar is only capable of detecting a moving target velocity and does not detect static targets at all, while modulated CW radar can also detect range of static or moving targets. The linear frequency modulated CW radar uses a linear frequency modulation to obtain the time mark for target range acquisition. Therefore, it can detect static targets which is one of the main advantages of FMCW over unmodulated radar waveforms. For indoor lighting applications where target speeds can vary from walking speed to almost static a modulated CW is most interesting.

3.2.1 Pulsed-Doppler Radar

A traditional radar type that is widely used for military purposes is the pulsed-Doppler radar. The pulsed-Doppler radar compares the received pulse time delay to the transmitted one to obtain the target range and velocity. The principle of the transmitted and received waveform are depicted in Figure 13. The radar transmits pulses and has a silent period to listen to the received echoes. During the transmit time the radar however cannot receive and therefore has a blind time period where no target can be detected.

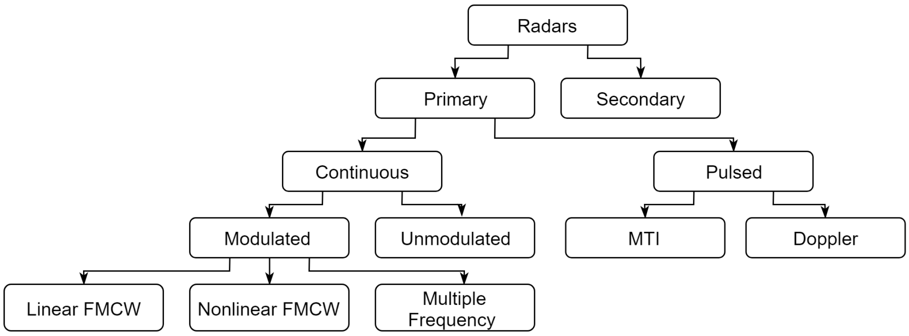

Figure 12: Radar waveform hierarchy

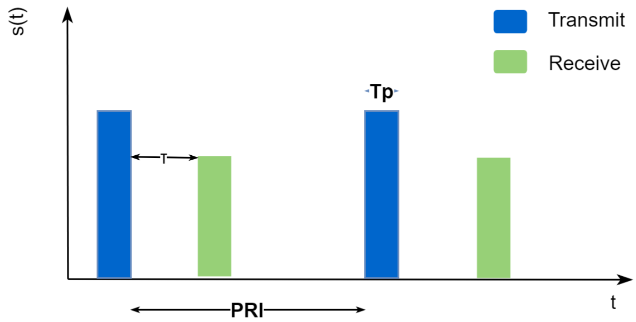

Figure 13: Pulsed transmit and receive waveform

The target range R [m] of a pulsed radar can be obtained by [41]

$$R = \frac{c\tau}{2} \quad [m] \tag{10}$$

where c is the propagation speed (speed of light) [m/s] of the signal and τ is the propagation time [s] of the transmitted pulse. This principle however creates an uncertainty for the radar when a second pulse is sent out while the first pulse has not been received yet which results in the radar failing in assigning the original pulse timing. The maximum range where the transmitted signal is reflected to the radar before the next signal is transmitted is called the maximum ambiguous range and can be obtained with [41]

$$R_{ua} = \frac{c}{2PRF} \quad [m] \tag{11}$$

where PRF [Hz] is the reciprocal of the Pulse Repetition Interval (PRI) [s] and the factor $\frac{1}{2}$ is introduced because of the two way propagation of the signal. The maximum unambiguous Doppler velocity V_{ua}[m/s] is defined as the maximum velocity the radar is possible to assign the pulse timing and is defined as Equation (12) [41].

$$V_{ua} = \frac{PRF\lambda}{4} \quad [m/s] \tag{12}$$

The range resolution ΔR [m] is defined as the minimum range difference between two targets where the radar can detect both and can be obtained by [41]

$$\Delta R = \frac{cT_p}{2} \quad [m] \tag{13}$$

where T_p [s] is defined as the transmit pulse time duration. The range resolution determines the minimum target spectra separation which is still detectable by the radar. To measure the Doppler frequency f_D [Hz] the sampling rate (PRF) [Hz] must be at least twice the maximum frequency of interest (maximum Doppler frequency) according to Nyquist sampling theorem.

$$PRI = \frac{1}{PRF} = \frac{1}{2f_D} \quad [s] \tag{14}$$

With the measured Doppler frequency, the radial velocity V_t [m/s] of a target in meters per second can be obtained.

$$V_t = -\frac{f_D \lambda}{2} \quad [m/s] \tag{15}$$

A drawback of the pulsed radar is the minimal measuring range (blind range) R_b [m] which equals the range needed to transmit an entire pulse. The blind range is defined as [43]

$$R_b = \frac{c(T_p + t_{rec})}{2} \quad [m] \tag{16}$$

where c [m/s] equals the speed of the transmitted signal, T_p [s] is the pulse duration and t_{rec} [s] is the recovery time that is needed to switch to receiving signals. With a typical value of 1 μs pulse duration and a pulse recovery time of 0.1 μs, the pulse radar will result in a minimum range around 150 meters. Therefore with distances closer than 150 meters the radar cannot detect any target.

For the indoor lighting application the target distance towards the radar is expected to be within a few tens of meters. To apply the pulsed radar for indoor lighting the minimum range as defined in Equation (16) should be 49 centimeters as stated in the final system requirements in **??**. With 0.49 m taken as minimum range and keeping the pulse recovery time on 0.1 μs the term $\frac{2R_b}{c} = T_p + t_{rec}$ results in 3.3 ns. Therefore the pulse duration and recovery time should be within a few nanoseconds which is not easily achievable for a simple (low cost) pulsed radar. Therefore a pulsed radar for indoor lighting application is not further considered during this thesis.

3.2.2 Unmodulated Continuous Wave Radar

Another type of radar that is mainly used for motion detection and human gait analysis [44, 45] and is therefore considered in more detail. The working principle of unmodulated CW radar is relatively simple by sending out a continuous signal on a single frequency. The transmitted signal reflects by impinging on a target resulting in a Doppler frequency shift at the radar receiver side. To detect the Doppler frequency shift only a down-conversion and a Fourier transformation is needed to obtain the spectrum with a resulting peak at the Doppler frequency. Nevertheless, Fourier transforms are computationally and memory expensive. Another method to obtain the velocity information is by thresholding the mixed transmit and receive signal and gating it to a zero-crossing counter which will measure the beat frequency. Afterwards the Doppler frequency can be used to obtain the corresponding velocity. Regarding the computational intensity the second method is very beneficial. However, this method will suffer when (many) multiple targets have to be detected.

The equation used to obtain the radial velocity V_t [m/s] of the target is given by Equation (17) [41].

$$f_D = -\frac{2}{\lambda} V_t \quad [Hz] \tag{17}$$

The velocity resolution is defined as the smallest velocity difference between two distinguishable measurement points in the measurement and depends on the coherent processing interval time T_{CPI} [s]. In case of a limited measurement time T_{CPI} [s], the velocity resolution can be obtained by Equation (18).

$$\Delta v = \frac{\lambda}{2T_{CPI}} \quad [m/s] \tag{18}$$

Many CW radar have unlimited measurement time which makes the velocity resolution limitless and therefore the CW radar does not suffer from velocity ambiguities. Other advantages for using CW radar include a small and simple design compared to other motion detection sensor types which translate to lower cost. CW radar is especially suitable for moving target detection since no blind ranges are present compared to the pulsed radar and with the lower power the probability of interception is relatively small. The CW radar is also better suited for solid-state active devices [46] compared to the pulsed radar. Solid-state active devices have shorter thermal and comparable active time constants compared to a vacuum tube. They cannot average power over PRF but nears its dissipation limit within a single pulse. The reasons to favor solid-state active devices over vacuum tubes is due to their lighter and more compact design and the life-cycle of a solid state transmitting device is about an order of magnitude greater than for vacuum devices [46].

The main disadvantage of the CW radar is the limitation to target velocity detection only which makes the detection of static targets inpossible. This is one of the main reasons a modulated CW radar is preferred over an unmodulated CW radar for many applications. In addition, the CW radar is relatively power consuming due to its continuous peak power signal transmission. By transmitting with a CW radar part of the time, the average power consumption can be lowered. Considering a high power CW radar, the transmitter-to-receiver leakage becomes significant. With a high transmitter-receiver leakage, the mixed signal results in a faulty beat frequency (and therefore a wrong target range/velocity) which is undesirable. With the need of range information of a target for almost static human detection in the lighting application the unmodulated CW radar will not satisfy.

3.2.3 Frequency Modulated Continuous Wave Radar

With the need of static target detection for the lighting application, the frequency modulated CW radar is an interesting candidate. FMCW radars have already been around for some time. During the 1940s to early 1960s the significant part of the theoretical analysis has been performed on FMCW radars [41, 47–51]. Using FMCW principles a target range and velocity can be obtained simultaneously and a continuous phase and frequency change between the transmit and receive signal can be carried out using different waveforms. Some advantages [46, 52] of FMCW over CW radar are better transmit-receive signal separation, short measurement time, high time-bandwidth product, different transmit waveforms and high processing gain. However, due to the lower peak output power the FMCW radar is mainly used at very short ranges compared to pulse radars. The low transmit power also results in an attenuated signal which is affected by the atmosphere and channel before it is received. Regarding the implementation, an FMCW radar is more complex compared to the CW and pulsed radar. The next two sections cover two waveform types for FMCW radar.

Fast Chirp Frequency Modulated Continuous Waveform Radar

To the best of the author's knowledge the first fast-chirp FMCW radar was described by Donald E.Barrick [53] in 1973 and A.G. Stove [46,54,55] described the concept in more detail from 1985 to 1987. The Fast Chirp waveform consist of a linear swept frequency signal which can be compared to some pulsed radar terms and with a 100% duty cycle. The ramps of a Fast Chirp FMCW are defined as fast when a moving target appears to be constant during that chirp. Typical chirp durations ranges from a few tens to hundreds of microseconds. The received signal will be mixed with a replica of the transmitted signal with an offset in frequency and time resulting in a velocity and range information of the reflected target. The Fast Chirp waveform resolves the multiple target ambiguity of Linear Frequency Modulated Continuous Wave (LFMCW) by using many chirps of short duration to obtain the velocity and range information. Figure 14 shows the waveform of fast chirps, where T_{chirp} [s] is the duration of one chirp ramp, T_{CPI} [s] the duration of the chirp sequences together which equals the number of chirps K times T_{chirp} and τ [s] represents the time delay between transmit ramp and corresponding received ramp. The radar transmits K

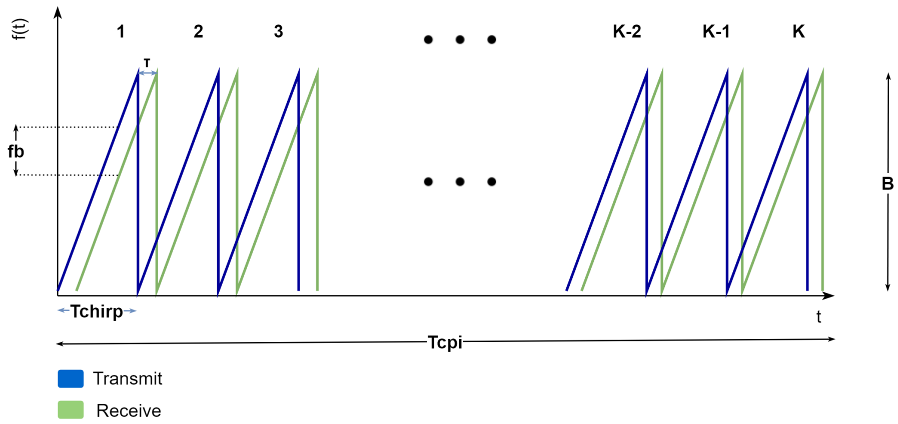

Figure 14: Fast chirp transmit and receive waveform K chirps

chirps and receives a time delayed (τ [s]) chirp sequence which is also shown in Figure 14. Since the chirps have very short time duration, during each chirp the target can be considered as static and therefore the time delay will mainly be induced by the range estimation [42, 56].

Applying a Fourier transformation (i.e. Discrete Fourier Transform (DFT), FFT) on each of the chirps separately gives a rough range estimation. This first FFT is also said to be done within a PRI. The resulting spectrum of each chirp ramp will have a peak value at the beat frequency which can be used to obtain the target range. The beat frequency as defined in Equation (37) will mostly consist of the range beat term and can be rewritten to obtain the rough range estimate as shown in Equation (19).

$$R \simeq \frac{cf_b}{2\alpha} \quad [m] \tag{19}$$

With only one FFT done and Equation (19), the range of a target can be detected. However, when multiple targets located on equal ranges from the radar have to be detected the spectrum only shows one peak which makes it impossible to separate the targets. To separate those targets the phase could be used of the reflected signals since these will differ for each target. This phase difference can be used to measure the target velocity and its more accurate range. To compare the phase differences between the chirp sequences, a second Fourier Transform will be used over the different chirp ramps to obtain the Range-Doppler plot. The principle of fast chirp waveform to range and Doppler frequency plot is shown in Figure 15, where the storing process of data is shown in the first matrix, then the first FFT (Range FFT) is performed on each row and as last step the second FFT (Doppler FFT) is applied to the columns to get a resulting Range-Doppler plot.

With this method multiple targets at the same distance from the radar can be detected separately as shown in the last plot of Figure 15. Doing two Fourier Transforms on a matrix requires a lot of data processing and a large matrix must be stored which is memory consuming. If an improvement in velocity resolution is required, the number of chirps in one transmit period can be increased to have a longer measurement time over a target's speed resulting in a finer matrix. This requires a larger number of FFTs and thus more computation power, which shows the trade-off between the resolution and computation power. For a typical lighting application, the computing power is quite limited and so is the memory since these must fit in the light bulb. However, there are several methods for flourier transforming a signal to make it more less memory intensive such as Chirp-Z transform and therefore this waveform is studied in more detail.

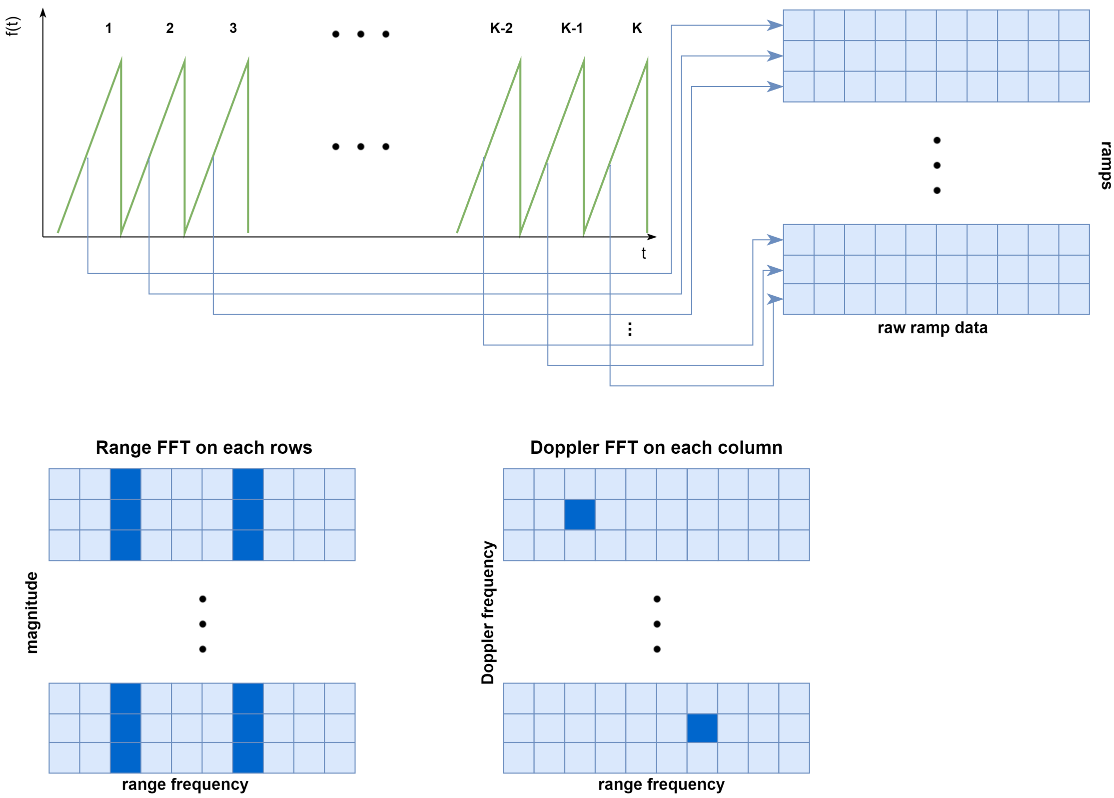

Figure 15: 2D FFT processing of fast chirps where two targets are present at a different range

The transmitted signal of a FMCW radar [46, 54, 55] can be modeled as

$$S_{Tx}(t) = A_{Tx}cos(2\pi f_c t + 2\pi \int_0^t f_{Tx}(t')dt') \tag{20}$$

where f_{Tx} [Hz] is the transmit signal frequency which is defined as

$$f_{Tx}(t') = \frac{B}{T} \cdot t' \quad [Hz] \tag{21}$$

where the term $\frac{B}{T}$ is also specified as the frequency slope and is represented by α. The received frequency will be shifted both in time τ [s] and in frequency f_D [Hz].

$$f_{Rx}(t) = \alpha(t - \tau) + f_D \quad [Hz] \tag{22}$$

$$\tau = \frac{2R}{c} \quad [s] \tag{23}$$

$$f_D = -2 \cdot \frac{f_c V_t}{c} \quad [Hz] \tag{24}$$

The received signal with the Doppler shift and time delay taken into consideration can be modeled as Equation (25).

$$S_{Rx}(t) = A_{Rx}cos(2\pi(f_c(t - \tau) + \alpha(\frac{1}{2}t^2 - \tau \cdot t) + f_D \cdot t))) \tag{25}$$

The mixed signal in time domain will consist of the product of S_{Rx} and S_{Tx} and with expanding Equation (26) is obtained for the received signal.

$$\begin{aligned} S_{Tx} \cdot S_{Rx} =& \frac{1}{2} cos(2\pi t(2f_c - \alpha\tau + f_D) + 2\pi t^2\alpha - 2\pi f_c \tau) + \\ & \frac{1}{2} cos(2\pi f_D \tau + 2\pi \alpha \tau t - f_D 2\pi t) \end{aligned} \tag{26}$$

Equation (26) has two components where the first cosine describes the chirp signal close to twice the carrier frequency with a phase shift proportional to the delay time. The second term of Equation (26) describes the beat frequency that is used to get the range and velocity information of the target. Therefore, only the second term is of importance and the first cosine term can be filtered out. The chirp frequency is larger than the beat frequency, therefore a low pass filter can be used.

The resulting IF signal is:

$$S_{IF} = S_{Rx} cos\left(2\pi\Big[2\alpha t\big(1-2\frac{V_t}{c}\big)/c + 2f_c t\frac{V_t}{c} + 2\alpha V_t t^2\big(1-\frac{V_t}{c}\big)/c + 2\big(f_c - \alpha R/c\big)\Big]\right) \tag{27}$$

The unambiguous range and velocity are given in Equations (28) and (29) which are comparable to the pulsed radar unambiguity equations with the PRF equal to $\frac{1}{T_{chirp}}$.

$$R_{ua} = \frac{f_c \cdot c}{2 \cdot B \cdot PRF} \quad [m] \tag{28}$$

$$V_{ua} = \frac{c \cdot PRF}{4 f_c} \quad [m/s] \tag{29}$$

Triangular Frequency Modulated Continuous Waveform Radar

Another well-known modulated CW radar is based on a triangular waveform. The basic operation principle of a triangular linear frequency modulated radar has an up-and-down slope $\pm\alpha = \frac{B}{T_{CPI}}$. The transmit waveform of LFMCW consist of a chirp signal with a specific bandwidth B [Hz] which is transmitted within a certain time T_{CPI} [s]. A reflected waveform will be shifted in time with

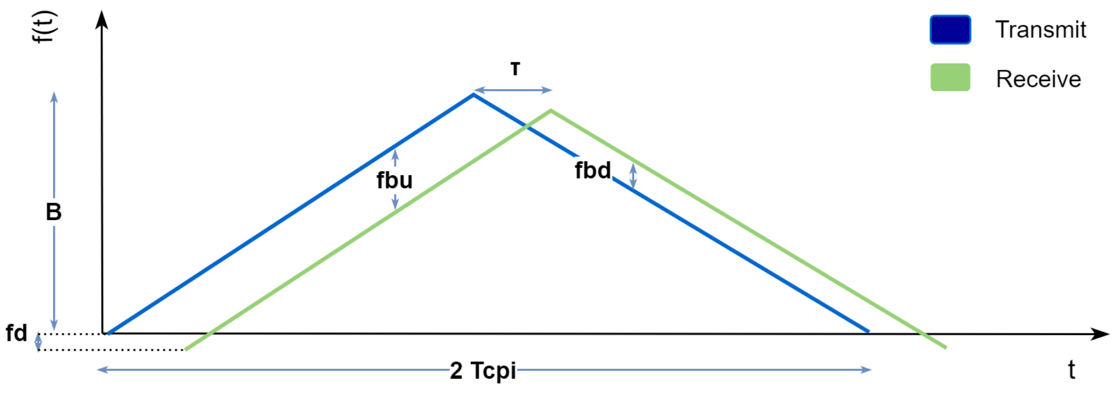

Figure 16: LFMCW transmit and receive waveform

a delay τ [s] (Equation (23)) and the center frequency changes due to a target induced Doppler frequency. The change in center frequency will result in two beat frequencies from the up/down slope which will hold information on the velocity and range of a target. The beat frequency is therefore defined as

$$f_b = f_D - f_\tau \quad [Hz] \tag{30}$$

where f_τ [Hz] is the frequency shift caused by the signal propagation time.

The transmitted signal for a triangular waveform can be described by

$$S_{Tx,up}(t) = A_{Tx}e^{j(2\pi f_c t + \pi\alpha t^2)} \quad -T_{cpi}/4 \leq t \leq T_{cpi}/4 \tag{31}$$

$$S_{Tx,down}(t) = A_{Tx}e^{j(2\pi f_c t - \pi\alpha t^2)} \quad -T_{cpi}/4 \leq t \leq T_{cpi}/4 \tag{32}$$

where the up and down chirp is defined separately. A_{Tx} is the amplitude of the transmitted signal, f_c[Hz] the center frequency, t [s] the time vector and α the ramp slope. Using the time delay τ [s] and the target induced Doppler frequency shift f_D [Hz], the received signal can be obtained with formulae as shown below.

$$S_{Rx,up} = A_{Rx}e^{j\Phi_{Rx,up}} \tag{33}$$

$$S_{Rx,down} = A_{Rx}e^{j\Phi_{Rx,down}} \tag{34}$$

$$\Phi_{Rx,up} = 2\pi f_c(t-\tau) + \pi\alpha t^2 - 2\pi\alpha\tau t + 2\pi f_D t \tag{35}$$

$$\Phi_{Rx,down} = 2\pi f_c(t-\tau) - \pi\alpha t^2 + 2\pi\alpha\tau t + 2\pi f_D t \tag{36}$$

By mixing the transmit and receive signal and taking the Fourier transform, two peaks (one corresponds to the up ramp and the other to the down ramp) in the spectrum are visible which contains information about the target range and velocity.

The up and down beat frequencies can also be calculated using theoretical formulae. For a static target ($V_t = 0$ m/s) the resulting beat frequency can then be computed as

$$f_b = \frac{2BR}{cT_{CPI}} = \frac{2R\alpha}{c} \quad [Hz] \tag{37}$$

where the beat frequency equals f_τ since there is no frequency Doppler shift present. For a moving target object the frequency Doppler shift is nonzero and is defined as Equation (38) which results in a total beat frequency given in Equation (37) and the beat frequency resolution in Equation (39).

$$f_D = -\frac{2V_t}{\lambda} \quad [Hz] \tag{38}$$

$$\Delta f_\tau = \frac{1}{T_{CPI} - \tau_{max}} \quad [Hz] \tag{39}$$

$$f_{bd,u} = -\frac{2V_t}{\lambda} \pm \frac{2R\alpha(1-2V_t/c)}{c} \approx -\frac{2V_t}{\lambda} \pm \frac{2R\alpha}{c} \quad [Hz] \tag{40}$$

Since the target velocity is often very small compared to the speed of light, the factor $\frac{V_t}{c}$ can be assumed to be zero which results in a Doppler frequency given by Equation (38) and an up-chirp and down-chirp beat frequency given in Equation (40) where $\alpha = \frac{B}{T_{CPI}}$ represents the slope of the waveform.

With the obtained up and down beat frequency, the target range and velocity can be obtained with the equations below.

$$R = \frac{(f_{bd} - f_{bu})cT_{CPI}}{4B} \quad [m] \tag{41}$$

$$V_t = \frac{(f_{bd} + f_{bu})\lambda}{4} \quad [m/s] \tag{42}$$

The maximum unambiguous velocity is computed using maximum Doppler frequency [57] as given in Equation (43).

$$V_{ua} = \frac{c^2}{4f_c R}\frac{f_b}{2B} \quad [m/s] \tag{43}$$

Comparing the unambiguous velocity in Equation (43) with Equation (12) of the pulsed radar, it can be seen that the unambiguous velocity for LFMCW is larger with a factor $\frac{c^2}{4f_c R}$ than the one defined for a pulsed radar since the V_{ua} of the pulsed radar is defined as $\frac{f_b}{2B}$ [57].

Equation (37) has two unknowns V_t, R which requires two equations to solve the unknowns. To obtain these equations both the beat frequency of the up- and down-chirp are used to solve for the range and velocity. This method however suffers when more than one target has to be detected, since more interceptions on a V_t,R plot occur compared to the number of targets. Ghost targets will appear as shown in Figure 17 which points out that the Fast Chirp FMCW is better suitable in case of a multiple target environment which does not suffer from this ambiguity.

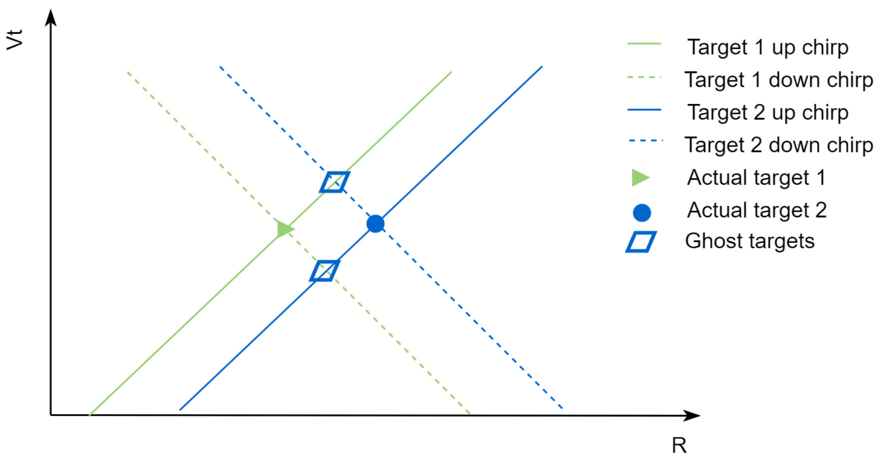

Figure 17: Interception of up and down chirp radar signals with 2 targets

In a realistic radar system there is an Analog Digital Converter (ADC) which changes Equation (39) with a ADC sampling frequency f_s [Hz] and samples N_s which results in a digital frequency resolution as shown in Equation (44).

$$\Delta f_{b,dig} = \frac{f_s}{N_s} \quad [Hz] \tag{44}$$

Since the target of interest are humans with a limited velocity, the frequency can be decimated by a factor D to minimize the computation load for the system. The new decimated sample frequency is then defined as Equation (45) with the resulting digital beat frequency resolution given in Equation (46).

$$f_{s,D} = \frac{f_s}{D} \quad [Hz] \tag{45}$$

$$\Delta f_{b,dig} = \frac{f_{s,D}}{N_{FFT}} \quad [Hz] \tag{46}$$

The digital beat frequency resolution after decimation and range compression FFT denoted as ΔR_{dig} is defined as

$$\Delta R_{dig} = \left(\frac{T_{CPI}}{T_{s,D} N_{FFT}}\right) \cdot \left(\frac{c}{2B}\right) \quad [m] \tag{47}$$

where $T_{s,D}$ [s] is the decimated sampling period which equals $\frac{D}{f_s}$.

For ADC data sampling the Nyquist criterion should hold $2f_{b,max} \leq f_{s,dec}$ where the right part should be a power of 2 for an efficient FFT computation which results in the following equation when $f_{b,max}$ is substituted using Equation (37)

$$2B\tau_{max} \leq 2^n \tag{48}$$

which can be used to obtain the minimum number of samples that should be used.

Due to the decimation and FFT processing an improvement in gain is obtained in SNR and can be obtained with the decimation factor and the number of samples for the FFT computation.

$$G_{D,FFT} = 3log_2(D) + 10log_{10}(N_{FFT}) \quad [dB] \tag{49}$$

The time-bandwidth product is also recognized as processing gain and is defined as shown below.

$$BT = B(T_{CPI} - \tau_{max}) \tag{50}$$

The dwell time in the radar SNR equation is also considered as gain and is defined as the product between the number of pulses gathered in a Coherent Processing Interval (CPI) and the sweep time.

$$T_{dwell} = n_{CPI}T_{CPI} \quad [s] \tag{51}$$

The waveform outlined in this section is considered to be perfectly linear, as shown in Figure 16. Considering the beat frequency for the up and down ramp would therefore be equal at all time, however in practice this is never the case. Nonlinearity will influence the beat frequency over time and influences the sweep bandwidth. More details on the frequency linearizer will be given in the next section.

3.3 Frequency Sweep Linearization

Performance of FMCW radars depends on the transmitted chirp linearity, with instantaneous deviations from the ideal linear sweep causing smearing of the target beat signal in the frequency spectrum. This may constrain the range resolution and other aspects of system behavior.

Deviations from linearity are caused by a common nonlinear behavior of the VCO as shown in Figure 18 resulting in an incorrect operation of the FMCW radar. One way to measure the frequency sweep linearity is by using the Frequency Slope Variation (FSV) [5] in Equation (52).

$$FSV = \frac{\Delta f'}{f'} = \frac{\Delta f' T_{CPI}}{B} \tag{52}$$

The $\Delta f'$ is the mean of the nonlinear frequency slope, B [Hz] the linear sweep bandwidth and T [s] the linear sweep time as depicted in Figure 18. The deramped frequency resulting from a predefined target can be approximated by the product of the frequency slope and round-trip delay [5]

$$f_d(t) = \tau \frac{df}{dt}(t) = \frac{2R}{c}\frac{df}{dt}(t) \tag{53}$$

For an ideal linear frequency sweep the $\frac{df}{dt}(t)$ in Equation (53) equals B/T, resulting in Equation (37). In contrast, a strong non-linear frequency sweep results in a time variant deramped frequency over the sweep duration time. The Doppler frequency deviation Δf_d [Hz] is then obtained by [5]

$$\Delta f_d = \frac{2R\Delta f'}{c} = \frac{2BR(FSV)}{cT_{CPI}} \tag{54}$$

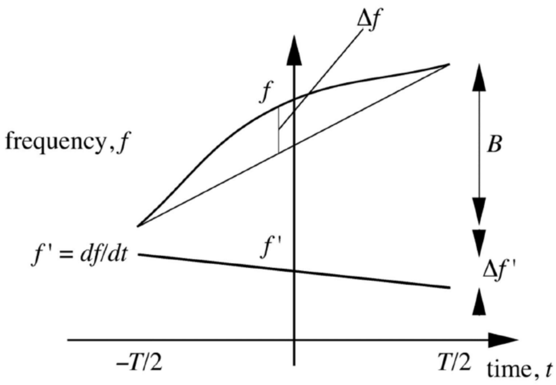

Figure 18: Chirp non-linearity for voltage-frequency response, obtained from [5]

A chirp linearity in the order of the pulse duration reciprocal, $\frac{1}{T_{CPI}}$, results in a significant degradation in range resolution. An upper limit for the frequency delinearization can be obtained by using the expression for the required FSV

$$FSV = \frac{ac}{2BR} = \frac{a\Delta R}{R} \tag{55}$$

where a [Hz] is the resulting non linear frequency bandwidth and ΔR the classic range resolution as given in Equation (13). Equation (55) shows that the linearity requirement increases for larger ranges. With a 1 dB sensitivity reduction criteria the maximum of a is limited by 2-4 for different types of waveform weighting as documented by [5]. For a ideal radar resolution of 0.75 m and a 10 m maximum range this would result in a linearity of 0.3%.

To compensate for the non-linear voltage-frequency response one could define two methods that can be used, one is software based and the other one is hardware based. The former might use a beforehand known Look Up Table (LUT) consisting of the voltage-frequency response to generate a designed control signal for compensating voltage characteristic frequency sweep linearization. The latter consist of an additional circuitry to control the voltage and to linearize the frequency sweep in a closed-loop, contrasting the software one which is an open-loop concept. More advanced linearizing options such as an both analog and digital phase locked loop are outside the scope of this thesis.

3.3.1 Software-Based Frequency Linearizer

The linearity of the frequency sweep is roughly proportional to the number of range cells that are required for the radar [46]. It can be defined as the ratio between the nonlinear bandwidth and the frequency deviation. With the frequency sweep slope deviation, the resulting beat frequency spectrum will also be nonlinear. This results in frequency side-lobes which appear at harmonics of the nonlinearity frequency. Using a linearizer, the source tuning nonlinearity can be compensated. A sinusoidal nonlinearity can be assumed which is reasonable for describing the variation in frequency sweep due to residual errors after the linearizer. For this linearizer the number of harmonics or bandwidth which is required for a good frequency sweep linearity should be taken into account. Overall, the nonlinearities decrease with increasing harmonics [58]. Comparing the standard FMCW waveforms, the sawtooth requires a very wide bandwidth linearizer while a triangle waveform require much less bandwidth.

3.3.2 Hardware-Based Frequency Linearizer

A hardware-based solution like the Phase Locked Loop (PLL) is often used for FMCW radar which is a closed loop concept where the frequency and phase are continuously compared in order to generate the correct tuning voltage and resulting frequency for the VCO.

A typical PLL model is shown in Figure 19 [59] with the basic blocks present. For N and R presented by integers the model is an integer-N PLL and for fractional value possibilities for the two parameters the model becomes a fractional-N PLL. The error detector is composed of the Phase Frequency Detector (PFD) and a Charge Pump (CP). The PFD generates a voltage corresponding to the error of the reference frequency and the scaled down VCO frequency and serves as input for the CP which converts this voltage to a current flow. For a phase difference between the reference and VCO, the CP output will generate a current flow which can be considered as a high signal (logical 1). In case of no phase error between these signals the current flow is low (logical 0) and for switching in between the two stated a high impedance mode output could occur. In the high impedance mode output the current output of the CP is nor positive nor negative. Such mode happens in the CP due to the finite speed of the logic circuitry and results in current spikes and spurious signals in the VCO output. By using a filter, the current spikes can be filtered out before reaching the VCO. This current goes into the loop filter which converts it to a corresponding tuning voltage for the VCO.

The basic elements of a PLL include a:

- error detector: compares the phases of two signals and generates a voltage according to the differences. The error detector is built up with the phase detector and charge pump.
- loop filter: filters the output from the phase comparator in the PLL and defines the PLL loop characteristics and stability.
- VCO: voltage-controlled oscillator with a sensitivity of Kv/s.
- feedback divider: negative feedback will force the error signal to approach zero when the frequency divider output and reference frequency are in phase and frequency lock.

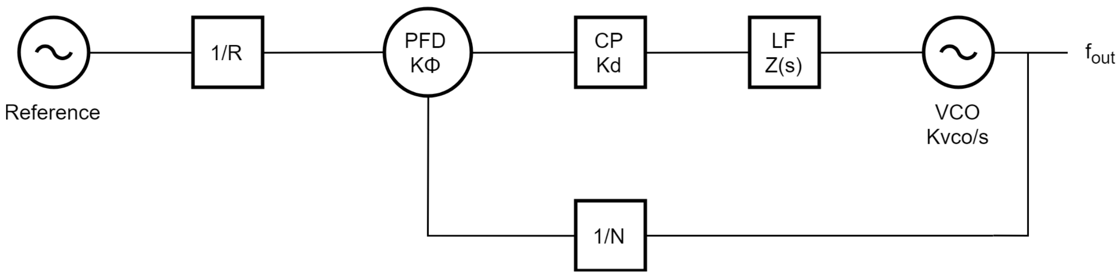

Figure 19: A basic integer-N PLL model with gain defined per block

3.3.3 Noise Sources

Frequency stability in oscillator sources is of critical importance and can be divided in long-term and short-term stability. For long term stability the output signal can vary over a long period of time (hours, days, months), while a short-term stability on the other hand is concerned with random or periodic oscillator variations that occur over a few seconds or less. For radar applications the focus lies on the short-term stability due to its randomness and significant impact on the detection performance. A typical noise spectrum of a oscillator is shown in Figure 20a where the shape around the center frequency consist of the random noise fluctuation and the small peaks besides the center frequency are discrete spurious signals. In general, the phase noise in radar transmitters is known to raise the noise floor around larger targets making the detection and tracking of small targets almost impossible. If two targets are detected with a certain beat frequency f1 and f2, the resulting spectrum could look like Figure 20b which shows that target 1 cannot be detected due to the high noise level around the carrier frequency. To reduce masking of lower signal targets the overall oscillator noise should be kept as low as possible within beat frequency ranges.

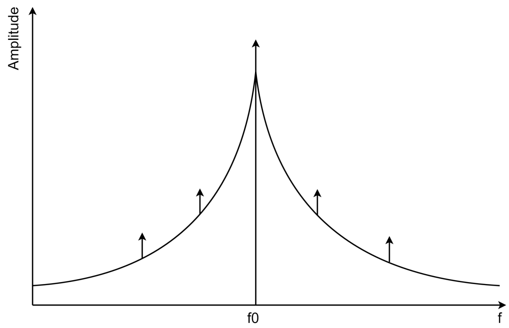

(a) Oscillator noise, adapted from [60–62]

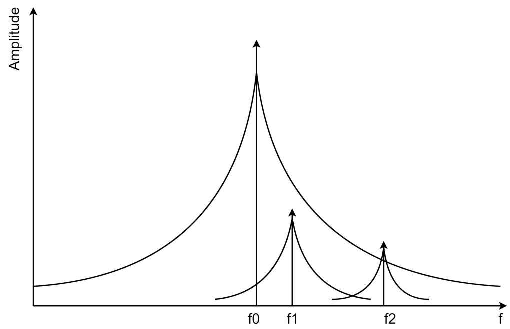

(b) Oscillator noise with targets, adapted from [60–62]

Figure 20: Oscillator noise around center frequency f0 and for target detection with beat frequencies f1 and f2

The broadening of the random noise fluctuation is caused by phase noise. From the basic elements in the phase locked loop one of the dominant phase noise sources is the VCO. Reducing the VCO noise can be done by a PLL where the phase noise especially in the beat frequency range should be kept as low as possible.

3.3.4 Presence Detection Threshold

A fixed threshold for target detection or simply peak detection might work in environments with low reflection and clutter interference. If the background noise is in the same order of magnitude as the target of interest, a fixed threshold or peak detection will not work. With a CFAR detector an adaptive threshold is used which distinguish targets from clutter interference and background noise. The adaptive threshold is obtained by using a fixed-size reference window surrounding the cell under test surrounded by guard cells. By averaging the values in the reference window, a threshold point can be obtained which is compared with the mixed signal at the same point to conclude if there is a positive or negative detection. This principle is depicted in Figure 21.

3.4 FMCW Radar Model for Human Presence Detection

A linear FMCW radar model for human presence detection is developed to evaluate the radar parameters needed for human presence detection. The relevant Matlab code for these models can be found in Appendix J. The formulae of the model is earlier described in the fast chirp and triangular waveform descriptions.

3.4.1 Radar Parameter Selection

The radar parameters obtained for the radar model are given in Table 3. Although the ISM band covers a bandwidth of 250 MHz, to take frequency overshoot and undershoot into account a frequency sweep of 200 MHz is used, leaving 25 MHz left as upper and lower overshoot margin.

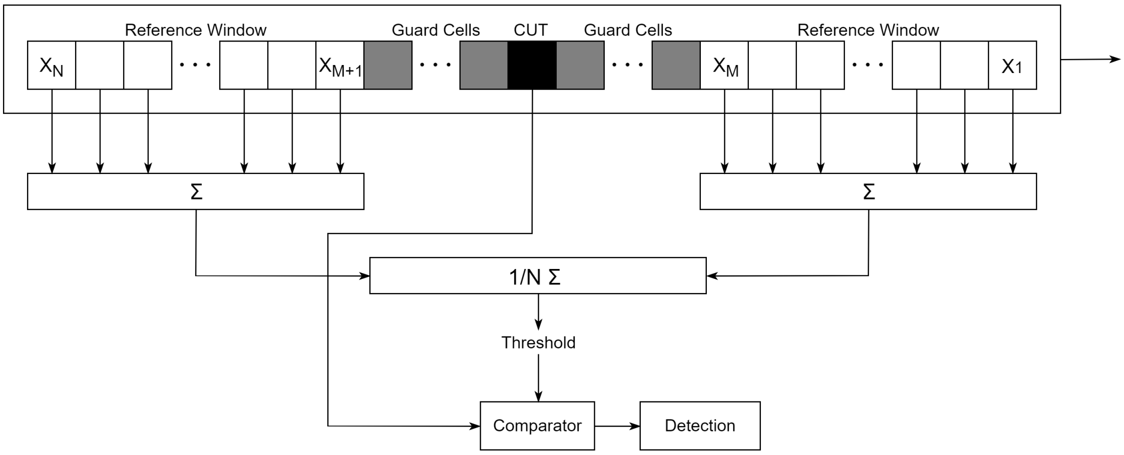

Figure 21: CFAR working principle

The sweep repetition interval differs for the Fast Chirp and triangular waveform. For the fast chip this time interval should be within a few ms.

Table 3: Radar parameters used for radar model

Parameter	Symbol/Formula	Value	Unit
RF center frequency	f_c	s 24.125	GHz
RF wavelength	λ	12.4	mm
Transmit power	P_{Tx}	-6	dBm
Antenna gain	G_{Tx}, G_{Rx}	0	dB
Frequency sweep	B	200	MHz
Ideal time resolution	1/ B	5	ns
Ideal range resolution	c/2B	0.75	m
Sweep Repetition Interval Fast Chirp	T	0.1	ms
Sweep Repetition Frequency Fast Chirp	1/T	10	kHz
Sweep rate Fast Chirp	α=B/T	$2 \cdot 10^{12}$	-
Beat frequency/range ratio Fast Chirp	2B/cT	13.343	kHz/m
Range/beat frequency ratio Fast Chirp	cT/2B	0.74948	μm/Hz
Sweep Repetition Interval Triangular	T	1	ms
Sweep Repetition Frequency Triangular	1/T	2	kHz
Sweep rate Triangular	α=B/T	$4 \cdot 10^{11}$	-
Beat frequency/range ratio Triangular	2B/cT	2.6685	kHz/m
Range/beat frequency ratio Triangular	cT/2B	0.37474e	mm/Hz
Maximum range	R_{max}	10	m
Maximum velocity	V_{max}	4	m/s
Maximum transit time	$\tau_{max} = 2R_{max}/c$	66.71	ns
Maximum beat frequency	$f_{b,max} = B\tau_{max}/T$	6.6713	kHz
Minimum beat frequency interval	$T - \tau_{max}$	2	ms
Minimum beat frequency resolution	$1/(T - \tau_{max})$	500.02	Hz

As defined in Table 3 the maximum range and velocity equals 10 meter and 4 m/s, respectively. The minimum range should equal 0.49 and the minimum velocity equals 0 m/s (static target). The total beat frequency for a FMCW radar is given by Equation (56).

$$f_{b,tot} = \frac{2BR}{T_{sweep}c} + \frac{2V_t}{\lambda} \tag{56}$$

Assuming the largest sweep time for a triangular FMCW to be within 1 - 10 ms and the shortest sweep time for a Fast Chirp FMCW of 50 μs results in a minimum beat frequency of 65.33 Hz and a maximum beat frequency of 267.31 kHz. Therefore the beat frequency range is equals Equation (57).

$$65.33Hz \leq f_{b,tot} \leq 267.31kHz \tag{57}$$

For the antennas gain in the simulations, the worst case is assumed resulting in a gain of the transmit and receive antennas equal to 0 dB. For an SNR above 10 (without processing gain), the minimum transmit power should be -12 dBm if Equation (8) is used.

With Equation (45) to Equation (48) a Tcpi of 0.72 ms is required for a range resolution of 0.5 m with at least 540 NFFT points. The theoretical minimum received power equals -109 dB for a -80 dBc/Hz phase noise close in to the carrier and with a transmit power of 1 dBm.

3.4.2 Fast Chirp

The result of the Fast Chirp waveform is shown in Figure 22a. The transmitted signal modeled by Equation (20) will reflect from two targets on a distance of 6 and 8 meters and a velocity of -1 and -1.5 m/s, respectively, which results in a received signal Equation (25) with induced time delay and Doppler shift. Mixing a replication of the the transmitted signal with the received signal and applying a 2D FFT results in a range, velocity plot. The axis of the plot are scaled by using the ambiguous velocity and range for the maximum defined values, which is 10 meters and 4 m/s for this radar model. The velocity axis is from the negative to positive unambiguous velocity (Equation (29)) and the range axis is defined by Equation (28). The resulting mixed signal with two targets present is shown in Figure 22a for a transmit power of -6 dBm. As one could see, the static target at 10 m only has a resulting magnitude of -40 dB. Some smearing can also be seen in the Range-Doppler spectrum which is caused by the sidelobes around the targets. For the moving target these sidelobes are present in both frequency and range, while the static target has mainly sidelobes in range. A similar plot was made by changing the RCS to 0.3 m^2 as shown in

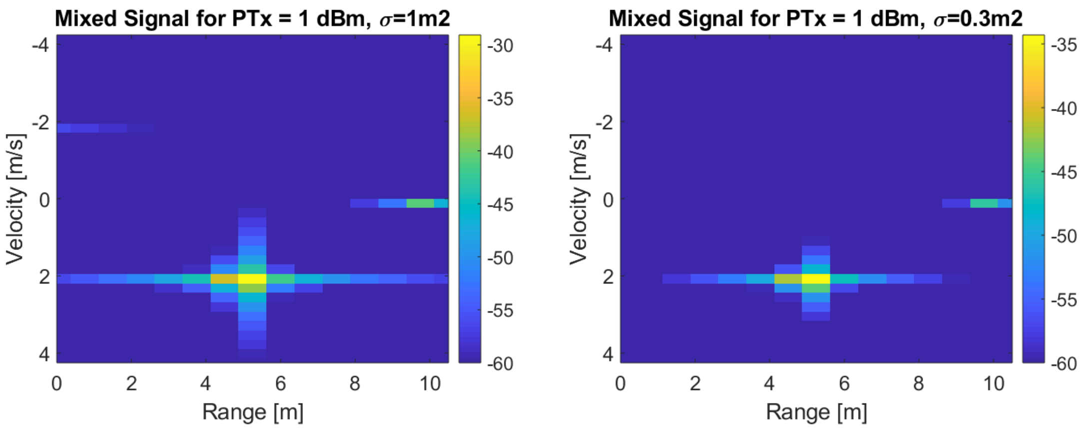

(a) RCS of 1 m^2 **(b)** RCS of 0.3 m^2

Figure 22: 2D FFT result of mixed signal with two targets at 5 and 10 meters with a relative velocity of 2 and 0 m/s

Figure 22b. The smearing of the targets due to sidelobes have decreased compared to the larger RCS target. The static target is still detectable in Figure 22b, however its magnitude decreased with 5 dB compared to the 1 m^2 RCS target.

3.4.3 Triangular FMCW

The simulation result of the triangular FMCW radar model with added CFAR detection is given in Figure 23a. The human target is modeled as a point target with a radar cross section of 1 m^2. Figure 23a has a up and down beat frequency of $-2.7 \cdot 10^4$ and $2.7 \cdot 10^4$, respectively, which results in a static range and speed of 10.12 m and 0 m/s using Equations (41) and (42). The slight error is introduced because of the limited samples used. The theoretical beat frequency should be $-2.6685 \cdot 10^4$ and $2.6685 \cdot 10^4$. For the triangular waveform the target RCS is also decreased to 0.3 m^2, resulting in Figure 23b. The magnitude changed from a 1 m^2 RCS target to a 0.3 m^2 RCS target with 5 dB.

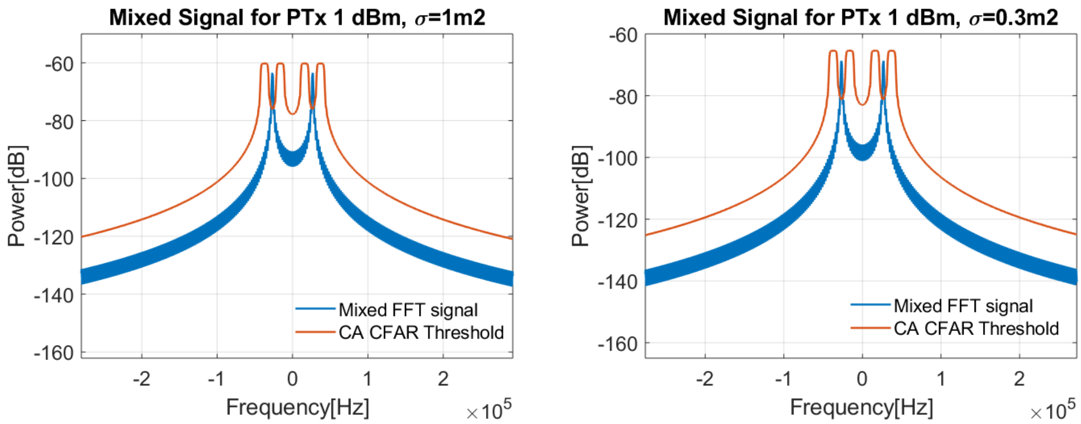

(a) RCS of 1 m^2 **(b)** RCS of 0.3 m^2

Figure 23: FFT result of mixed signal of a static target at 10 m with sweep time 1 ms, resulting in a beat frequency of $\pm 2.7\cdot$ m/s

3.5 Conclusion

With limited space on the LED board for the antenna placement, the 24 GHz radar will be a mono-static system with one or two antennas. The linear frequency modulated continuous wave radar is the most suitable option for the integration in a light bulb and human presence detection because of the possibility for both static and moving target detection. The FMCW radar however suffers from slope linearization problems (which results in a faulty target range readout). In addition, the phase noise can be a big problem of the system since this can mask targets close to each other or make targets with beat frequencies close to the center frequency of the system not detectable at all. Especially when environmental noises are also present which add up to these system phase noises the targets might be undetectable.

The RCS of a person is assumed to be 1 m^2 for a moving person towards or away from the radar. For targets moving underneath the radar, the RCS is assuming to fluctuate between 0.3 and 1.1 m^2. The expected beat frequencies are ranging from 65.33 Hz to 267.31 kHz. Therefore within this range from the carrier frequency the phase noise should be kept low. In addition, to get a SNR of 10 for detection, the minimum transmit power should equal -12 dBm for a transmit signal of 1 dBm.

4 Optically Transparent Dielectric Resonator Antenna

The Dielectric Resonator Antenna design considerations are described in this section including the simulation model in CST MWS (CST Microwave Studio) to obtain antenna characteristics while taking the radar requirements into account. The radiation pattern must at least have 0 dB gain in the 120° field of view. The dielectric resonator material must be optical transparent and easy to fabricate, which limits the possible materials as resonator and its shape. In addition, the feed of the dielectric resonator antenna should be selected to be applicable on the led board.

4.1 Dielectric Resonator Material

The dielectric resonator material must be optical transparent at visible light wavelengths (380 - 750 nm) and relatively easy to fabricate to keep the cost low. Table 4 shows a selection of considered materials for the resonator with relevant parameters. The expected dielectric permittivity is given over frequencies up to tens of GHz, unless otherwise specified. Exact values however are not known and can differ depending on manufacturer. Especially materials which are not made for microwave purposes such as acrylic and polycarbonate can have different electric properties as specified by manufacturers at higher frequencies. These materials require a dielectric permittivity measurement. In addition, the transparency is given which however is just an indication since this depends strongly on material thickness. The fabrication complexity and price are given relatively to the other materials, where more +-signs are good and + can be regarded as poor.

Table 4: Considered transparant dielectric materials

Material	ϵ_r	Transparency [%]	Fabrication	Price
Polycarbonate [63, 64]	2.4-3.1	85-88	+++	+++
Pyrex [65]	5.4	80-99	+	+
Acrylic [66]	2.9-4.26	88-94	+++	+++
Rexolite [67]	2.53	87	+++	+
Gorilla glass [68]	7.08 @1MHz	> 91.5	+	+

Glass materials such as Pyrex (K9 Borosilicate Crown glass) and Gorilla glass have an excellent optical transparency compared to the plastics. Gorilla glasss [68] is typically used as screen material on smart devices which makes the material scratch resistant. This type of glass however is only available in thicknesses up to 1.3 mm which is too thin for resonator purposes. Stacking them to the designed thickness would require adhesive which should also have relative stable dielectric permittivity properties over frequency and temperature and air bubbles are likely to appear which lowers the overall relative dielectric permittivity. Pyrex [65] is available in large blocks which can be machined to the desired resonator shape. However, machining glass in general is prone to chipping and scratching, resulting in a delicate manufacturing task which makes the overall cost too high for the light bulb application. Rexolite [67] is a high performance plastic mainly for military purposes with very stable electrical material properties. It is chemically resistant, light weight and resists water absorption. Rexolite is relatively easy to manufacture by machining, however the price is still on the high side for application in a commercial product.

The two plastics left are acrylic [66] and polycarbonate [63, 64]. Both materials are easy to manufacture by milling, molding or 3D printing and have a reasonable transparency. These plastics are half the weight of glass and yet both stronger than glass. The dielectric permittivity of polycarbonate varies less compared to the one of acrylic, thus the material is likely to vary less over frequency and/ or temperature. The operating temperature in the bulb which heats up to 100 degrees melts acrylic with its deforming point at 80°. Polycerate however can withstand temperatures up to 155°. Regarding the manufacturing process, acrylic cracks more easily under stress compared to polycarbonate [69]. In addition, polycarbonate is already used in many lighting products for the cap and bulb case and is therefore favored for the thesis application.

4.2 Dielectric Resonator Antenna Feed Structure

The LED board as shown earlier in Figure 3a has limited space left for an antenna feed structure. The LED board consist of different layers as shown in Figure 24 with the layer thicknesses given in Table 5.

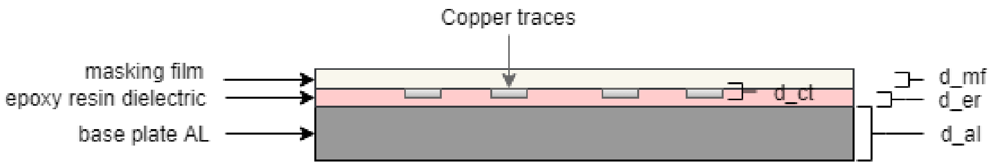

Figure 24: MCPCB layers

Table 5: Dimension of MCPCB layers

Parameter	Value
d_mf	$63.5\mu m$
d_ct	$30.3\mu m$
d_er	$110-130\mu m$
d_al	0.97 mm

For a microstripline feed the epoxy resin will function as dielectric. However, the exact dielectric value for this dielectric is not specified and it is a really thin layer which requires a very wide microstrip to match 50Ω. The current traces for the LEDs are also already placed in this dielectric which would interfere with the antenna microstripline feed when placed too nearby. It is therefore chosen to use a slot fed microstripline for the antenna. The slot in the aluminium core requires minimum impact on the LED board as shown in Figure 25. A microwave dielectric (Rogers 4350B) on the back of the MCPCB with a microstrip will feed the slot and the antenna.

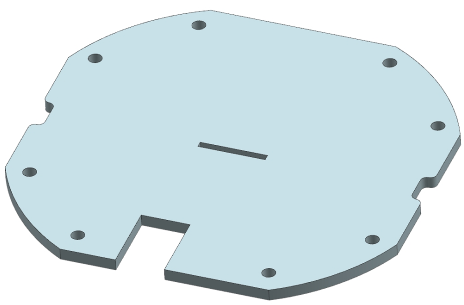

Figure 25: MCPCB aluminium board with slot

The prototype antenna must be fed with a SMA connector with a certain pin size which should be matched to the microstripline feed for the antenna to keep the feed-line matched to 50Ω at all times. To make such an transition the grounded coplanar waveguide is used which tapes the microstrip antenna feed towards the connector pin. The used connector is from Cinch Connectivity Solutions from Johanson and can be used for frequencies up to 26.5 GHz. The substrate thickness that is suitable for this type of connector is 0.36 - 0.51 mm which covers the dielectric substrate thickness that is selected. The substrate used for the Moreover, the probe inner diameter with the connector has a diameter of 0.38 mm.

4.2.1 Microstrip-Slot Antenna Feed

The considered PCB thickness d_g [mm] for Rogers 4350B are 0.254 mm and 0.508 mm because these are not too thick in terms of wavelength to get surface waves in the substrate and are not too thin to have a very versatile prototype. Given the board thickness and relative dielectric permittivity of Rogers 4350B (3.66), the width of the microstripline w_{strip} [mm] can be obtained as given in Table 6 with the formulae defined in Appendix D.

Table 6: GCPW theoretical dimensions for 50Ω matching

Parameter	value [mm]	d_s [mm]
w_{strip}	0.56	0.254
w_{strip}	1.121	0.508
d_g	0.42	0.254
d_g	0.85	0.508

With the microstripline widths obtained, the transition from microstrip to feed pin is made using a taper based on a grounded coplanar waveguide.

The slot resonates at a frequency slightly higher than half the resonance frequency because the dielectric resonator will lower the resonating frequency. The slot length is chosen to be 5.5 mm resulting in a slot resonance of 27.27 GHz and the width of the slot equals $\frac{1}{10}$ slot length.

4.2.2 Grounded Coplanar Waveguide

For the connection towards the antenna microstripline to the pin of the connector several types of transitions are possible. A microstrip line is the most straightforward one, also a microstripline with a ground can be used and another option is the coplanar transition. It was shown that a microstripline has more significant radiated losses for operating frequencies above 30 GHz [70]. Line widths are much larger than a coaxial line in order to match the board thickness due to low dielectric constant materials. Without a top ground placed on the board, [70] found that the performance at frequencies above 30 GHz degrades rapidly. Using a GCPW these drawbacks are addressed; the impedance is more stable over a frequency range up to 40 GHz and with properly implemented ground vias, the radiation loss is significantly reduced. Using a GCPW has an extra design parameter to adjust to match the connector pin with 50Ω.

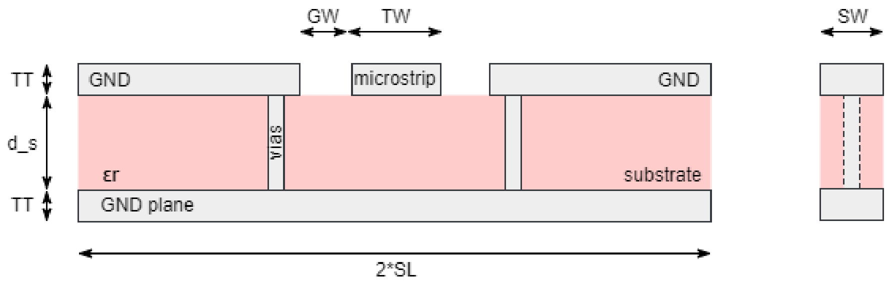

Figure 26: Grounded coplanar waveguide with parameters defined

Losses for a straight microstrip, top ground microstrip and the grounded coplanar waveguide for frequencies up to 25 GHz were demonstrated to be quite comparable [70]. At frequencies higher than 25 GHz the losses for a straight microstrip decreases rapidly with the top ground microstrip following and the grounded coplanar waveguide has the worst losses. However, for the performance that it delivers and the amount of design freedom it has to get proper matching with the coax pin it is still preferred to use the GCPW for this prototype.

A cross section of a GCPW is shown in Figure 26 where the GND plane is placed on the back of the metal core LED board. By using the GCPW formulae as described in Appendix E, with trace thickness (TT) equal to $35\mu m$, substrate thickness d_s of 0.508 mm and relative dielectric permittivity ϵ_r of 3.66, the gap width GW and track width can be obtained to have a 50 Ω impedance match. The strip width SW is also shown in Figure 26 which is used to generate the taper while keeping the total width of the ground plane (2*SL) constant.

Via holes are small plated holes through a PCB from one ground plane to another one which act like a microwave wall in the substrate. The microwave energy will be reflected by these holes when the spacing between the holes are less than a quarter signal wavelength. For high frequency performance the spacing between the via holes also influence the cutoff frequency. The wider the spacing, the lower the cutoff frequency and vice versa. The critical part of the via hole design is the spacing between them, measured from edge to edge of adjacent holes. Spacing of these via holes and the spacing between the via rows around the microstripline is also determinant for the performance of the board. Closer spacing of between the via rows also results in a higher frequency operation. Making the via row spacing around the microstripline closer to each other results in an increasing bandwidth [70]. The via row spacing is thus placed as close to the ground plane edge as possible (0.125 mm) is preferred while keeping the costs for a PCB reasonable. The resulting taper attached to the antenna ground plane is shown in Figure 27.

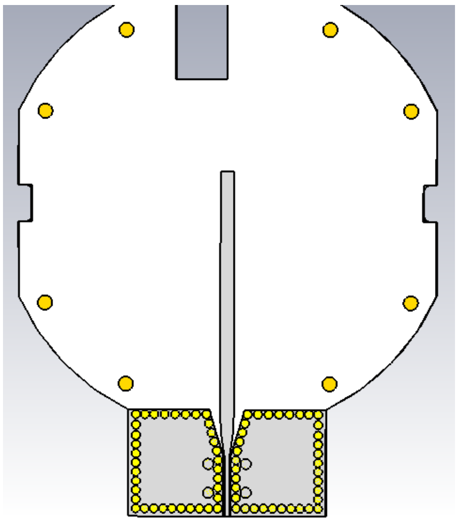

Figure 27: Grounded coplanar waveguide attached to antenna led board

4.3 Dielectric Resonator Antenna Shape

With a microstrip-slot fed antenna possible resonant modes for the hemispherical, rectangular and cylindrical DRA are $TE_{11\delta}$ for the first two shapes and $TE_{01\delta}$ or $HE_{11\delta}$ for the last one. The cylindrical DRA resonates at $TE_{01\delta}$ mode when it is cut into half and placed on the ground plane and $HE_{11\delta}$ where the CDRA is placed with the flat surface on top of the slot. Furthermore, varying the height of the DRA will change the δ to higher values and with that higher resonant modes.

The cylindrical shaped resonator was selected before because of the ease of manufacturing and thus the DRA will radiate at $HE_{11\delta}$ resulting in a comparable magnetic dipole radiation pattern. To have a reference antenna with similar radiation pattern as the designed DRA, a simple patch antenna was made as described in Section 4.7.

Table 7 define the design parameters that were used for the DRA simulations in CST MWS which are visualized in Figure 28.

Table 7: Design parameters DRA.

Parameter	Value [mm]	Description
a_DRA	4.3	radius DRA
h_DRA	5.5	height DRA
l_slot	5.5	length slot
w_slot	$0.1 * l\_slot$	width slot
d_fl	0.035	thickness feedline
d_s	0.508	thickness substrate
e_fl	2.2	extension feedline
w_fl	1.05	width feedline
ϵ_r	2.9	relative dielectric permittivity

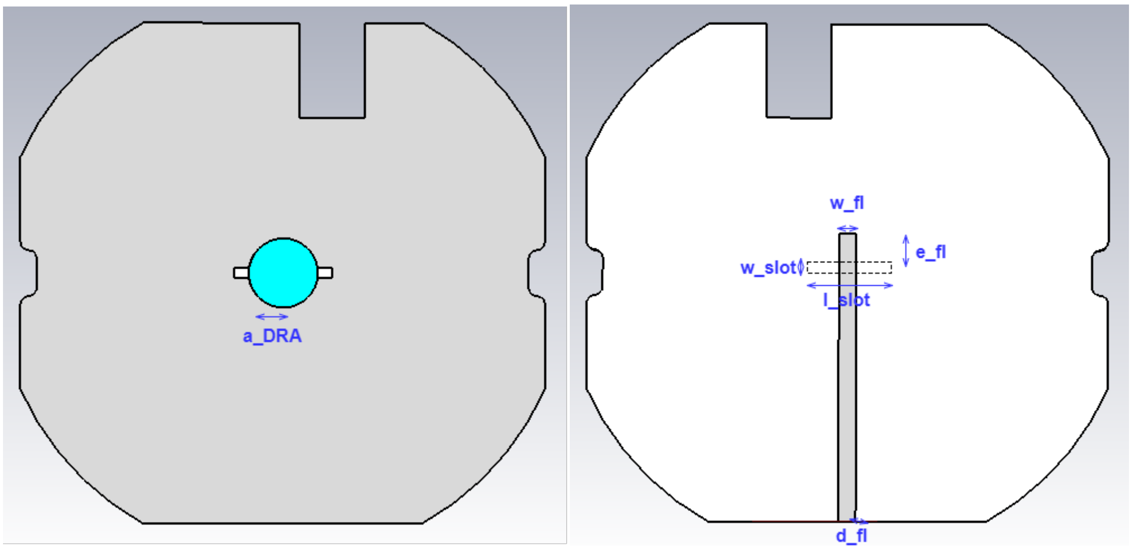

(a) Front of antenna **(b)** Back of antenna

Figure 28: Front and back of antenna depicted with defined parameters

4.4 Sensitivity Analysis

This section covers the influence of the light bulb environment on the DRA and considers the manufacturing tolerances which are of importance for a lighting system.

4.4.1 LED Placement Influence on Dielectric Resonator Antenna Characteristics

The influence of the LEDs on top of the LED board is simulated by placing square gallium arsenide (GaAs) blocks of 3x3x0.66 mm close to the antenna feed as shown in Figure 29b. The simulation consists of changing the LED position from the slot edge by moving it further away with steps of 1 mm downwards (towards edge) or side wards (towards the cut). The LED placement influence on the radiation pattern and S11 parameters were compared resulting in Figure 29a. As one could see, a LED placement 2 mm or further away from the slot feed edge does not influence the impedance matching significantly. The result of the radiation pattern is not included in here because these were barely affected by the LED placement.

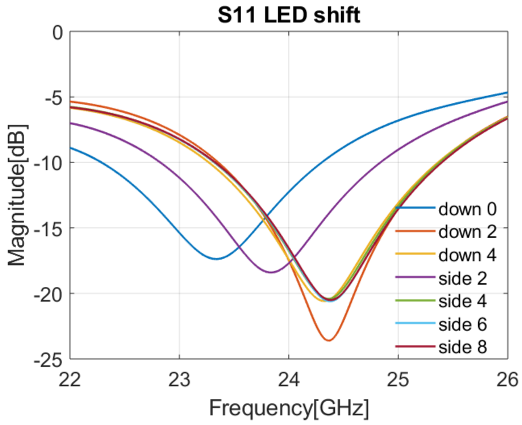

(a) S11 change for LED shifting

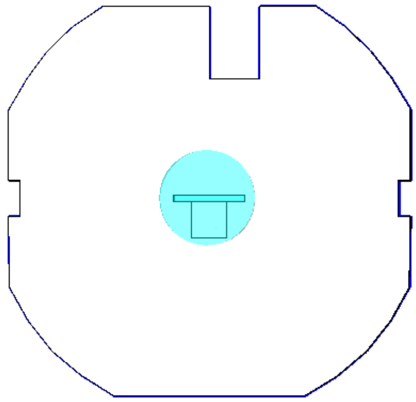

(b) L2 board with LED shifter

Figure 29: S11 influence of LED shifting

Another simulation is carried out by adding the colored LEDs with in a similar pattern as shown in Figure 30b to observe the effect on the DRA S11 parameter and radiation pattern. As seen in the S11 parameter in Figure 30a, the LEDs shift the center frequency slightly downwards. Again, the far field radiation pattern has not been significantly affected by adding these LEDs.

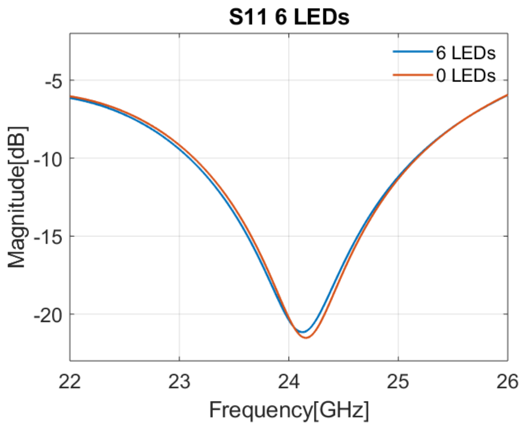

(a) S11 change for 6 LEDs

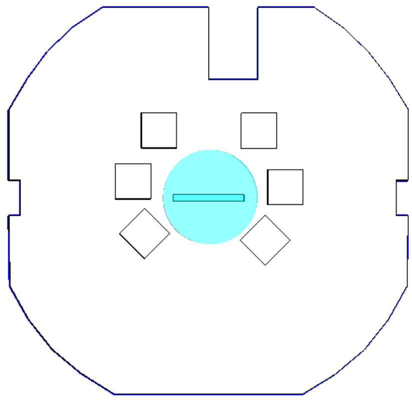

(b) L2 board with LED placement

Figure 30: S11 influence of LEDs

4.4.2 Dielectric Resonator Antenna Manufacturing Tolerances

Manufacturing tolerances are typically 0.2 mm for low cost machining and injection molding. This tolerance influence on the antenna is simulated by varying DRA dimensions with ±0.2 mm to see the influence on the antenna characteristics. Figure 31 depicts the effect on the impedance matching(S11 parameter or return loss) due to small variating CDRA dimensions. The S11 parameter shifts slightly due the dimension changes but stays within the 24 GHz ISM band below -10 dB which is sufficient for radar applications. The DRA manufacturing tolerance dependence on the far field radiation pattern was small, which is to be expected since small variations in terms of wavelength does not directly change the resonating mode to a different (higher) order mode.

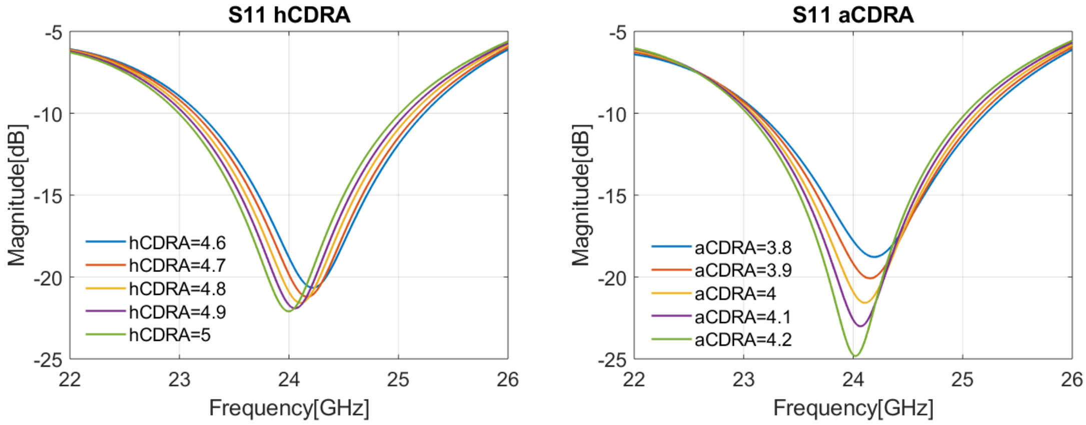

(a) DRA height sweep   **(b)** DRA radius sweep

Figure 31: CDRA dimension sweep influence on S11 for l=6mm, eps_r=2.712, l_ext=3mm

The slot length and micro-strip extension length tolerances are also considered which are expected to influence on the antenna characteristics more significantly. The impedance matching is most influenced by variations on the microstrip extension line as shown in Figure 32. The impedance matching characteristic in Figure 32 shifts the center frequency to much lower/higher frequencies causing the -10 dB bandwidth shifting out of the ISM band. Again, the far field radiation patterns barely changed and are therefore not included in these results.

Regarding the manufacturing tolerance analysis, it can be concluded that the slot length and micro-strip extension stub must be accurately fabricated to have the antenna well impedance matched in the frequency range of interest.

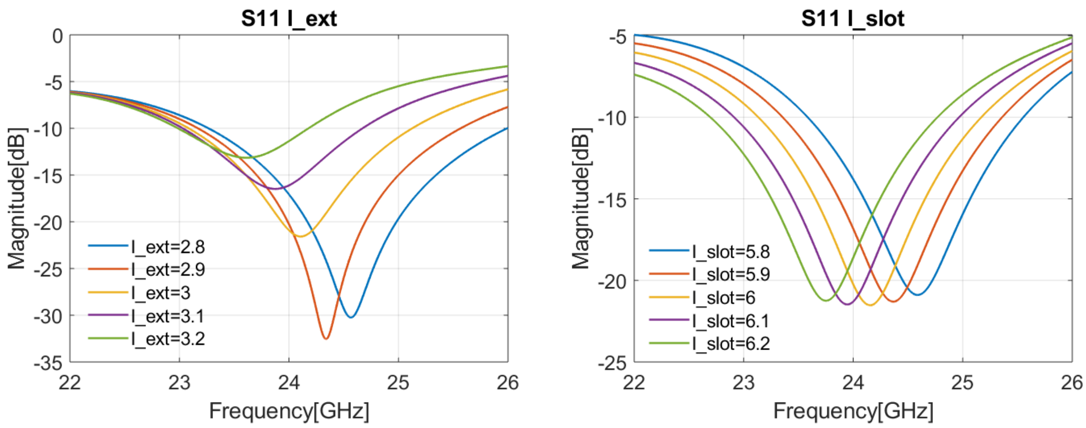

(a) microstrip extension sweep   **(b)** slot length sweep

Figure 32: CDRA feed sweep influence on S11 for a=4mm, h=4.8mm, eps_r=2.712, l_ext=3mm

4.4.3 Relative Dielectric Permittivity and Loss Tangent Variations

Another design parameter that typically influences the antenna radiation characteristics is the relative dielectric permittivity ϵ_r and loss tangent $(tan\delta)$ of the resonator. For polycarbonate the ϵ_r is typically 3.1 at 1 MHz, however at 24 GHz it is expected to be lower, but no exact data is available of the used polycarbonate material. Some polycarbonate measurements were documented [63, 64]. However, since polycarbonate is not a microwave fabricated material, the used polycarbonate electric properties can vary from the ones measured in these documentations. Riddle et al. [63] showed with measurements on polycarbonate at 11 GHz a permittivity varying between 2.75 - 2.81 at room temperature and loss tangent of $4 \cdot 10^{-3} - 6 \cdot 10^{-3}$. Kilian et al. [64] measured relative dielectric permittivity of thin films and paint foils at 24 GHz, which also included polycarbonate. They measured a dielectric permittivity value between 2.7125 - 2.73 depending on the dried or freshly molded condition and the loss tangent had a value between $4.5 \cdot 10^{-3} - 6 \cdot 10^{-3}$.

Varying the dielectric permittivity influences the S11 for frequencies around 24 GHz as shown in Figure 33a. A smaller dielectric permittivity results in a lower center frequency and a higher permittivity shifts the center frequency upwards. The far field radiation pattern as depicted in Figure 33b for a various ϵ_r varies slightly in magnitude within a few dB but keeps its shape and is therefore not significantly influenced. Since the dielectric permittivity of polycarbonate is not very well documented and might vary from one manufacturer to another, an estimate measurement of the used polycarbonate dielectric permittivity is done at 24 GHz. This measurement is described in more detail in Section 4.5.

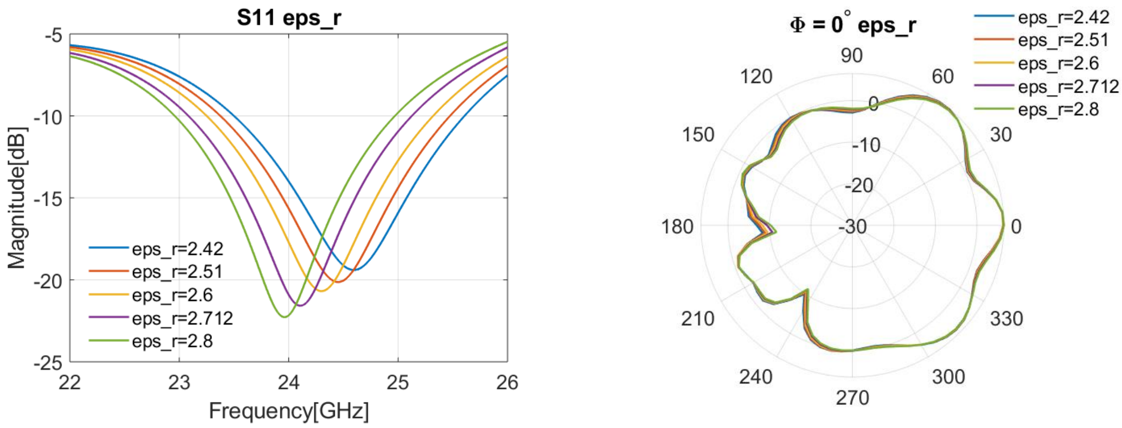

(a) ϵ_r sweep

(b) $\Phi = 0^\circ$

Figure 33: Relative dielectric permittivity sweep influence on S11 and $\Phi = 0^\circ$ radiation pattern for l=6mm, a=4mm, H=4.8mm, l_ext=3mm

The loss tangent was varied from 0.001 to 0.015 and the resulting S11 parameter variation is shown in Figure 34. The loss tangent does not influence the resonant frequency but only the impedance matching which becomes worse for higher loss tangent. The influence is not that significant since the S11 magnitude is still under -10 dB in the ISM band.

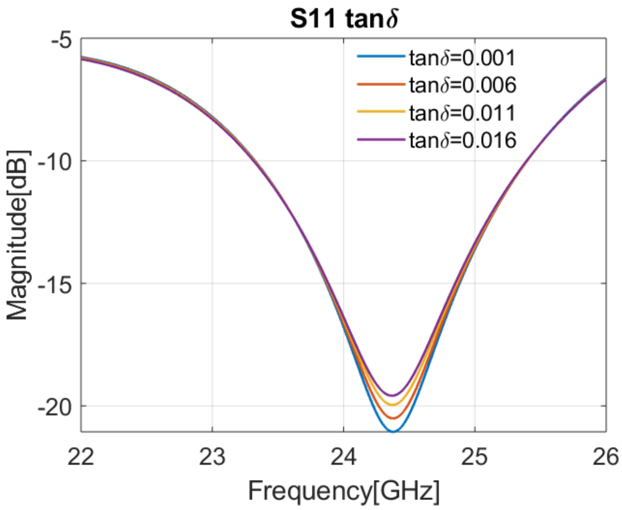

Figure 34: Loss tangent sweep influence on S11 for l=6mm, a=4m, H=4.8mm, l_ext=3mm

4.4.4 Cap Influence

The influence of the polycarbonate cap on the antenna characteristics is considered because this will cover the antenna. The cap has several round curves as shown in the cross section of the bulb(Figure 3b) which is likely to influence the antenna radiation pattern because of reflected waves in these round curves.

The influence of the polycarbonate cap on a CDRA is simulated and results are shown in Figure 35a and Figure 35b for the Φ 90° and 0° cut, respectively. The reference is the radiation pattern of a DRA on a LED board without cap or backplate. For this simulation the cap is placed on top of the antenna with LED board included resulting in dips on the radiation pattern and worse back radiation.

Figure 35a shows the increase in magnitude around 30 and 330 degrees, which happens to be close to the round surfaces of the cap which might function as a lens. Looking at the S11 parameter(Figure 36), one could see that the cap introduces a second resonance resulting in two dips. Whenever a back plate is added to fully enclose the antenna, the second S11 resonance dip becomes smaller as depicted in Figure 36.

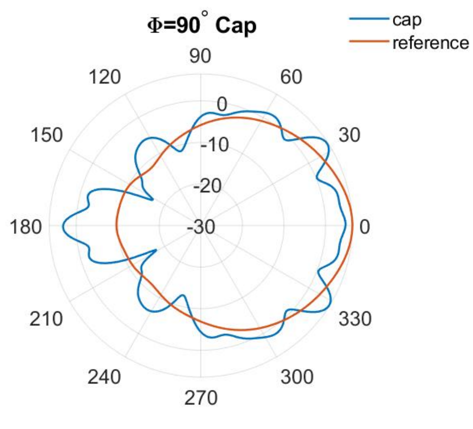

(a) CDRA $\Phi = 90^{\circ}$

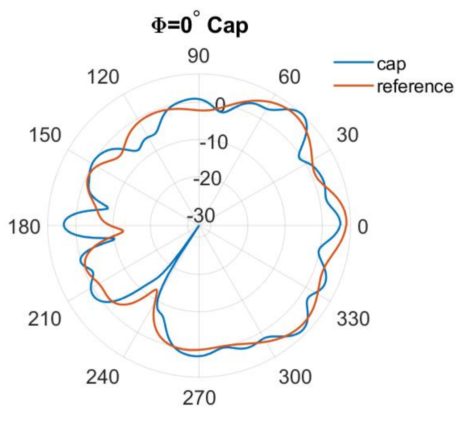

(b) CDRA $\Phi = 0^{\circ}$

Figure 35: CDRA radiation patterns with and without cap for l=6mm, a=4mm, H=4.8mm, l_ext=3mm

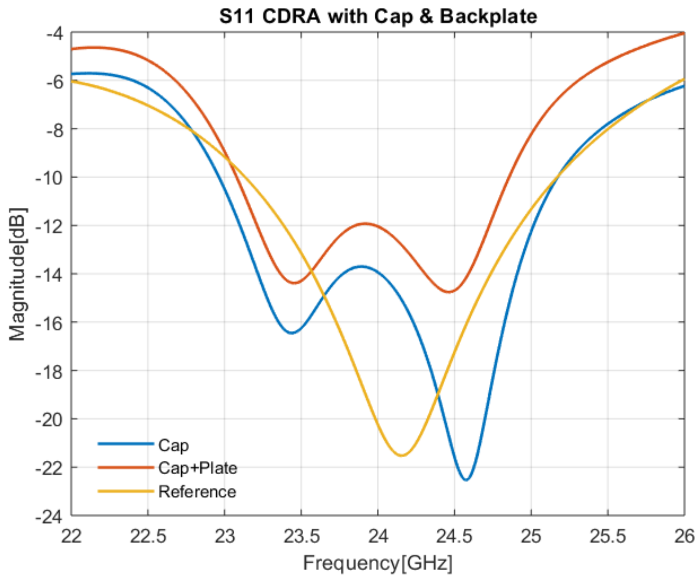

Figure 36: S11 of CDRA with cap, cap and backplate combined and a bare CDRA as reference

The farfield radiation pattern of the enclosed antenna is shown in Figure 37, again for the two Φ cuts of 90° and 0°. The influence of the cap is likely because of Electro-Magnetic (EM) fields interacting with its environment, which is demonstrated by the cap in this case due to its round surfaces. Impedance matching can be influenced by tweaking the DRA design parameters to obtain better return loss in the ISM band. By adding the plate on the back of the antenna structure to enclose the bulb, significant dips with values as low as -10 dB are obtained in the field of view which covers the 300° to 60° angle. Such dips as shown in Figure 37b with small magnitudes will create blind spots for the radar which is a problem for human motion detection.

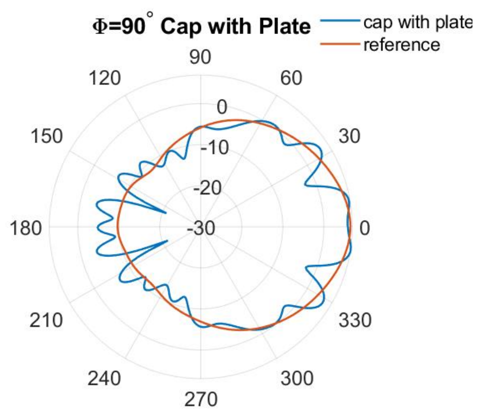

(a) CDRA $\Phi = 90°$

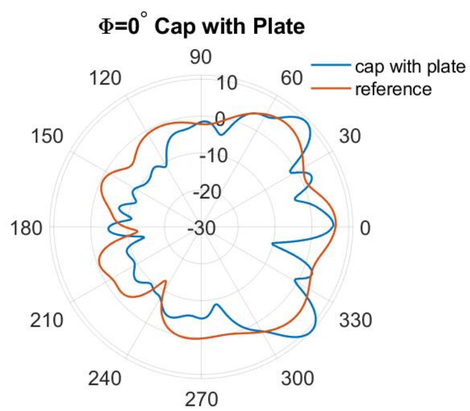

(b) CDRA $\Phi = 0°$

Figure 37: CDRA radiation patterns with cap and backplate for l=6mm, a=4mm, H=4.8mm, l_ext=3mm

4.5 Optically Transparent Polycarbonate Dielectric Permittivity Measurement

To verify the dielectric permittivity of the DRA, several measurement techniques can be used. In this thesis the time delay measurement and the dielectric rod resonator method is used which are elaborated hereafter. These methods were selected because of their simplicity and due to available materials.

Time Delay Measurement

First, to get an idea of the dielectric permittivity value at 24 GHz, a simple horn antenna setup is used to determine the real part of the dielectric permittivity. The time delay between the horn antenna setup and one with a polycarbonate plate of 1 cm thickness inserted is used to get the real dielectric permittivity.

$$real(\epsilon_r) = \left(\frac{t_{PC}}{t_{air}}\right)^2 \tag{58}$$

Equation (58) with a propagation time in polycarbonate equal to 55.966 ps and a free space measurement time of 35.978 ps results in a real dielectric permittivity of 2.42. Doing the same measurement while considering the phase shift, resulted in a dielectric permittivity of 2.51.

Compared to the performed measurements on polycarbonate in literature resulting in 2.75-2.81 at 11 GHz [63] and 2.7125-2.73 at 24 GHz [64], the measured value is significantly lower. This is possible since polycarbonate is not a microwave fabricated plastic and might therefore differ in specifications for different manufacturers. Another dielectric permittivity measurement has been done using a dielectric rod. The advantage of this technique is that is also obtains the loss tangent and computed Q factor.

Dielectric Rod Resonator Method

To obtain the relative dielectric permittivity, loss tangent and Q factor of the fabricated polycarbonate resonator, a measurement can be done based on resonant modes of a dielectric rod resonator which is short-circuited at both ends by parallel conducting plates [6, 11] as depicted in Figure 38.

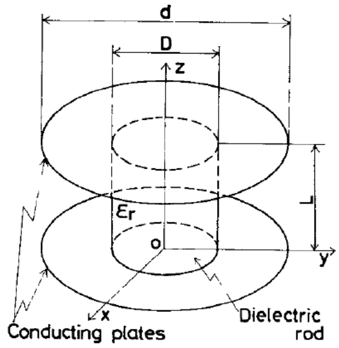

Figure 38: Dielectric rod resonator configuration, obtained from [6]

Figure 81 in Appendix G displays the mode chart that is used for the dielectric rod measurement as described by Kobayashi et all. [6, 11]. The rod dimensions and corresponding resonant modes based on the expected relative dielectric permittivity are obtained using this mode chart. For a relative dielectric permittivity around 2.7, the rod dimension $(D/L)^2$ for $TE011$ mode must be between 3.2 - 4, 5.8 - 6, 7.3 - 9.8, 11.2 - 12.6. This rod dimension range is chosen such that no other resonant modes are nearby which could influence the measurement. For the TE011 mode, lower order TM modes are also present at certain rod dimension ranges as shown on the right side of the graph. The reason to use $TE011$ mode is because of its resonant field pattern, which pattern does not suffer from small air gaps between the copper plates and the rod compared to the TM and HE modes [6].

Kajfez et al. [71] made a program to obtain the dielectric rod dimensions which was used during this thesis. The rod dimensions corresponding to 24 GHz have a radius of 5.7 mm and a height of 5, 10 and 20 mm for TE011, TE012 and TE014 mode, respectively. To obtain the complex dielectric permittivity, the following formula can be used [6]

$$\epsilon_r = \left(\frac{\lambda_0}{\pi D}\right)^2 (u^2 + v^2) + 1 \tag{59}$$

where λ_0 [m] is the wavelength in vacuum, D [m] the dielectric rod diameter and u and v can be obtained according to Equations (60) and (62). Furthermore, λ_g [m] in Equation (61) represents the guiding wavelength of an infinitely long dielectric rod waveguide and l represents the last number of the resonance mode.

$$v^2 = \left(\frac{\pi D}{\lambda_0}\right)^2 \left[\left(\frac{\lambda_0}{\lambda_g}\right)^2 - 1\right] \tag{60}$$

$$\lambda_0 = \frac{c}{f_0} \quad [m] \quad \lambda_g = \frac{2L}{l} \quad [m] \tag{61}$$

$$u\frac{J_0(u)}{J_1(u)} = -v\frac{K_0(v)}{K_1(v)} \tag{62}$$

With v known, u can be found by using the transcendental Equation (62), where the right side can be computed and the solution can be found by looking at u values between the first and second zero of the Bessel function of the first kind.

To obtain the tangent loss of the dielectric material, the conductivity of the copper plates is needed as shown in Equation (67). Because this value of the used plates is not exactly known, different length rods operating on the same frequency but with different modes are used to get a set of equations which can eliminate the copper conductivity. The loss tangent can then be obtained by using Equation (63) and the expressions given for A,B and W in Equation (76) to Equation (77), respectively.

$$tan\delta = \frac{A}{Q_u} - BR_s \tag{63}$$

$$A = 1 + \frac{W}{\epsilon_r} \tag{64}$$

$$B = \left(\frac{\lambda_0}{\lambda_g}\right)^3 \frac{1+W}{30\pi\epsilon_r l} \tag{65}$$

$$W = \frac{J_1^2(u)}{K_1^2(v)} \frac{K_0(v)K_2(v) - K_1^2(v)}{J_1^2(u) - J_0(u)J_2(u)} \tag{66}$$

$$R_s = \sqrt{\frac{\pi f_0 \mu}{\sigma}} \quad [\Omega] \tag{67}$$

The obtained measured resonant modes are shown in Figure 39. The spectrum of separate rods with theoretical modes are shown in Figures 40 and 41, where the rods were all cleaned with propanol and a bit of water. The complete computed theoretical values using the dielectric rod dimension program [71] for the chosen rod dimensions are elaborated in Appendix G.1. The rod resonating at TE012 as shown in Figure 40a consist of both the cleaned and dirty version, because the cleaning changed the resonant peaks completely. A possible explanation for this is the use of water to clean the rods since polycarbonate is a hydrophilic polymer which absorbs water. With the dielectric permittivity of water around 80 and polycarbonate having a very low permittivity, a little water absorbent can already change the dielectric characteristics of the material [72]. However, when the rod was heated up slightly above 90°C, the resonance peaks did not change at all. It is thus not clear what have caused this rod to change a lot in resonance frequencies and is therefore left out for the computation of the dielectric permittivity.

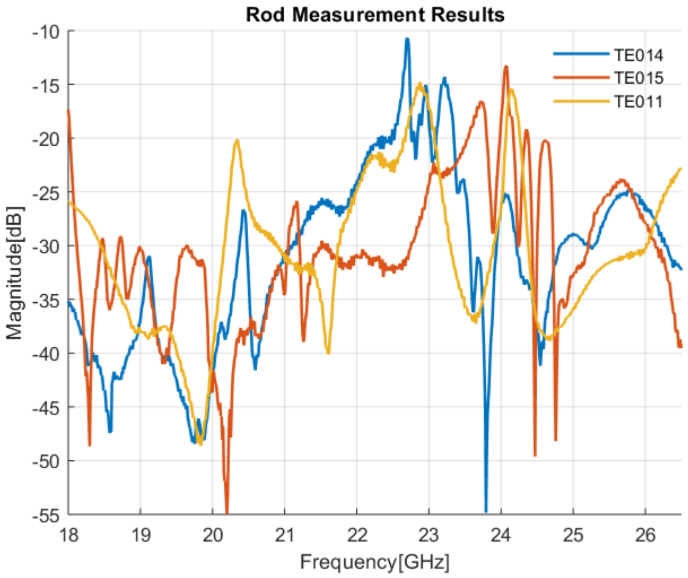

Figure 39: TE_{01x} cleaned

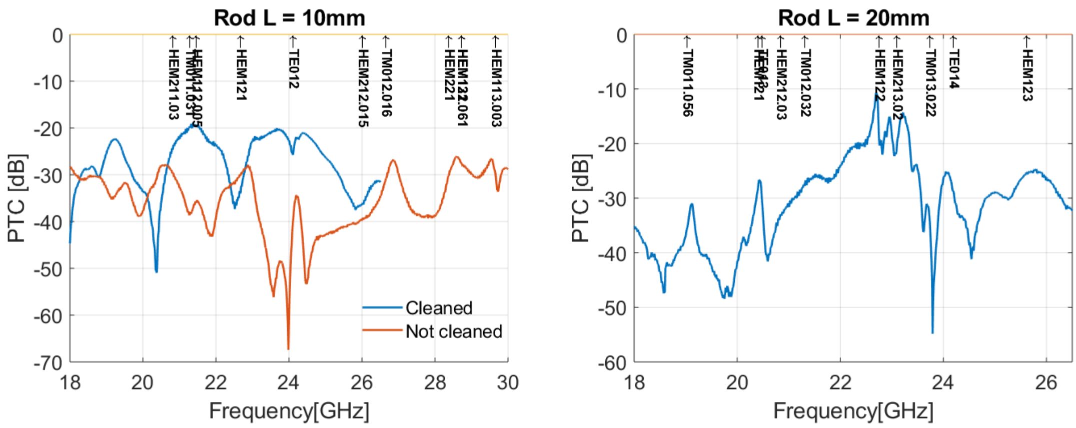

(a) TE_{012} cleaned and not cleaned

(b) TE_{014} cleaned

Figure 40: TE_{012} and TE_{014} mode resonator with a=5.7mm and L=10mm, L=20mm, respectively

Coupling between the two probes is not straightforward on 24 GHz and these loop probes should be mainly exciting TE modes. Noise sources were present at other modes sometimes as could be seen from Figures 40 and 41. The rods did have one clear overlapping peak close to 24 GHz in the measured spectrum. Because there are no other modes that occur so close to each other between

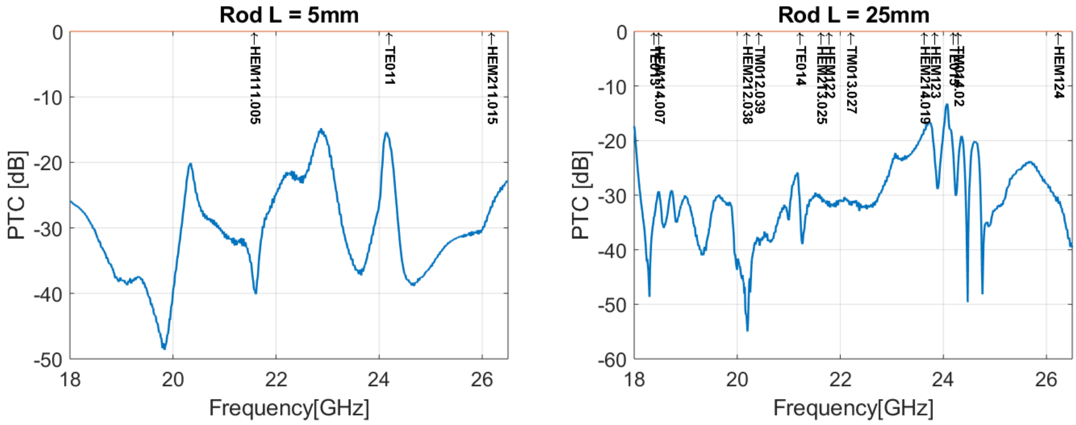

(a) TE_{011} cleaned

(b) TE_{015} cleaned

Figure 41: TE_{011} and TE_{015} mode resonators with a=5.7mm and L=5mm, L=25mm, respectively

the different rod sizes, it is likely that it is the TE01x mode as expected. With this resonance frequency f_0 [Hz], the Q factors can be obtained with the formulae given below.

$$Q_L = \frac{f_0}{f_{3dB}} \tag{68}$$

$$Q_0 = \frac{Q_L}{1 - 10^{IL/20}} \tag{69}$$

The resulting measured properties of the polycarbonate dielectric rod are shown in Table 8. An interesting result has been obtained for the TE014 rod Q factors. The Q factor for higher order modes are expected to be higher in value compared to lower order modes. However, the extracted Q values for TE014 are lower than the ones obtained for TE011. As pointed out earlier, the probe placement and spacing on the copper disks were quite sensitive. These might have not been placed ideally to obtain a high resonant peak at 24 GHz, resulting in a obtained Q factor.

Table 8: Cleaned rod parameters of TE_{011}, TE_{014} and TE_{015}

Mode	Q_L[dB]	IL[dB]	Q_0[dB]	f_0[GHz]	ϵ_r	tanδ
TE011	157.1875	-15.43	189.209	24.15	2.55314	$1.3 \cdot 10^{-2}$
TE014	114.5238	-25.11	121.2568	24.05	2.57652	$1.012971 \cdot 10^{-2}$
TE015	344	-13.27	439.3472	24.08	2.56948	$1.67 \cdot 10^{-3}$

The computed dielectric permittivity values were between 2.55-2.58 as shown in Table 8 which is close to the obtained values with the time delay measurement. The obtained loss tangent was in the order of $10^{(}-2)$ which is higher than the ones measured in literature. [64] measured a loss tangent in the order of $4.5 \cdot 10^{-}3 - 6x10^{-}3$ and [63] measured a loss tangent of $4 \cdot 10^{-}3 - 6 \cdot 10^{-}3$ which are both lower than the measured loss tangent for the transparent polycarbonate rod for the lower modes.

The dielectric permittivity measurement resulted in a low ϵ_r around 2.55-2.58, which will shift the simulated S11 resonant frequency upwards since these simulations were assuming an 2.9 dielectric permittivity.

4.6 Validation of the Antenna Models

A prototype was fabricated with antenna parameters defined in Table 7 and measurements were done in an anechoic chamber at TU Delft with support of the Microwave Sensing, Signals &

Systems group. The prototype was build up as depicted in Figure 42 including screws to fix and align the PCB with the aluminium (MCPCB) board. The three bottom layers as shown in Figure 42 are fabricated as a one layer PCB. The aluminium board mimics the led board (MCPCB) and is laser cut with holes to align the slot cutout.

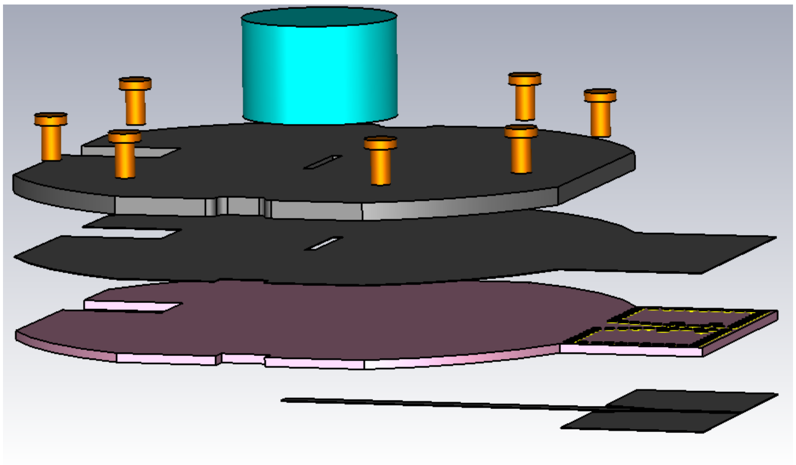

Figure 42: Prototype build up in separate layers

There were 6 versions in total of the prototype which were fabricated in a similar way and the connectors were soldered with different techniques, which is described in more detail in Appendix I. The different way of soldering the connectors likely effected the S11 parameter as shown in Figure 43. Versions 4 and 6 were not resonating close to the designed frequency with a strong resonance around 20-22 GHz and were excluded from the S11 comparison in Figure 43. The S11

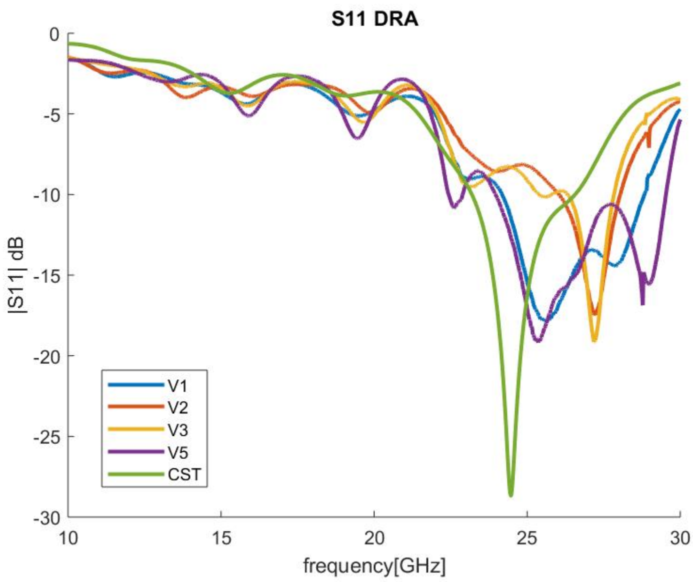

Figure 43: Measured S11 of different PCB versions

measurement differs a lot from the CST simulated values as shown in Figure 43.

This might be the SMA connector that is used for the antenna which is only specified until 26.5 GHz. Above this frequency the connector still works, but its performance is not known. A second

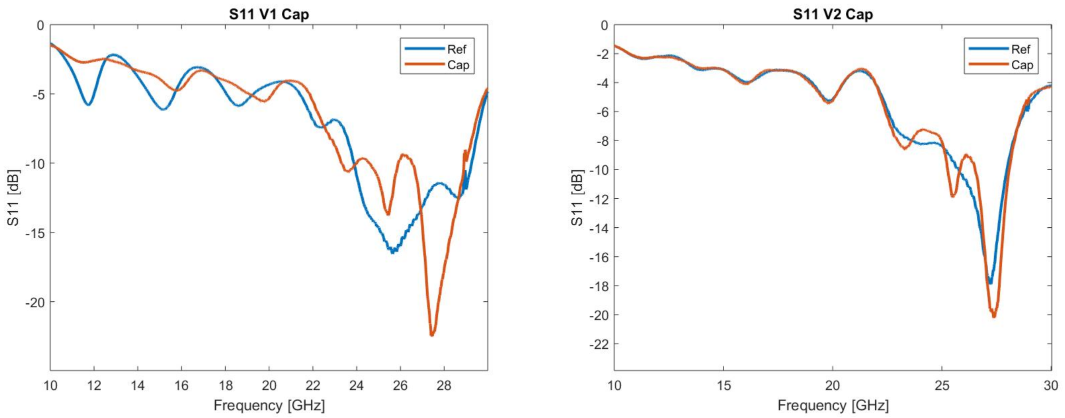

(a) S11 results of DRA,cap and PCB V1 **(b)** S11 results of DRA,cap and PCB V2

Figure 44: S11 measurement results of adding the bulb cap for different PCB versions

resonance could occur just above the maximum defined frequency of the connector, resulting in a different resonant mode in the connector which influences the measurement capability. Since the resonant frequency of the microstrip-slot feed is resonating at 27.3 GHz, which happens to be above the maximum frequency at 26.5 GHz of the connector, this might have influenced the S11 parameter significantly of the total system.

In addition, the way of soldering the connector to the PCB might also have influenced the S11 parameter. On 24 GHz a bit of extra solder on the microstrip could already result in a slight strip impedance mismatch. Other factors that could cause a shift in resonant frequency is the layering of the PCB. The one layered PCB is fabricated by adding copper layers on both side of the Rogers 4350B substrate. However, there can always be a slight error with aligning the two copper layers, resulting in a slightly non-perpendicular stripline under the slot. The PCBs were checked, and the alignment of the copper layers looked quite perpendicular for each board.

A cap was placed on top of the antenna structure for to observe the S11 change which is shown in Figure 44. The two dips of S11 as seen earlier in the simulations (Figure 36) was also observed in the measurements. For PCB version 1 the cap showed a significant change in S11 shape, which shows the strong two peak S11 due to the cap. It is thus of importance that the cap will be considered for the design.

The radiation pattern is measured in an anechoic chamber by rotating over 2 cuts which are defined as H and E cut as shown in Figure 45. The radiation pattern was measured over these cuts from 10 to 30 GHz. With use of a standard gain horn antenna the gain of the antenna under test (AUT) can be obtained. A simplified test setup is shown in Figure 46.

The E-cut and H-cut measured far field radiation pattern at 24 GHz compared to the simulation ones are shown in Figure 47 for PCB version 2. Definition of the E and H cut place are described in Appendix I and measurements of the other PCB versions are included. The H-cut shows a similar radiation pattern shape with some loss in gain which is likely to be caused by losses in cables or soldering of the connector. The E-cut however did not align very well compared to the simulation and even has a strong dip in its radiation pattern around 80 degrees. However, the radiation pattern in the field of view (between -60 to 60 degree) above 0 dB is already sufficient for detection and thus this antenna can be used for the validation of the system. The matching of the V2 however does not gets lower than the minimum of -10 dB, which means some losses due to impedance mismatching is expected.

To have a reference antenna a patch antenna was designed with a comparable gain and radiation pattern in the field of view as the DRA. The patch antenna S11 was measured which resulted

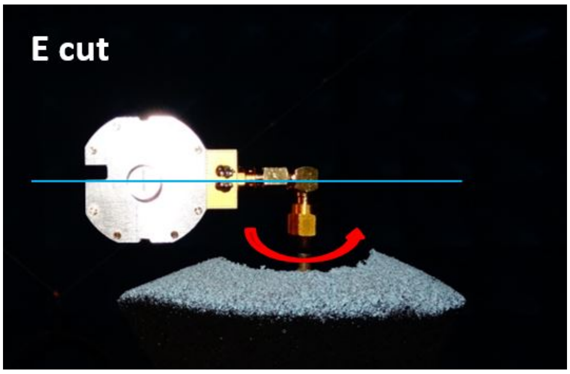

(a)

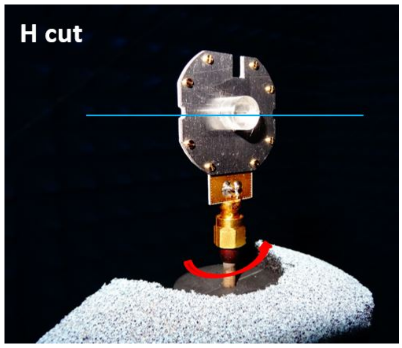

(b)

Figure 45: E and H cut definitions

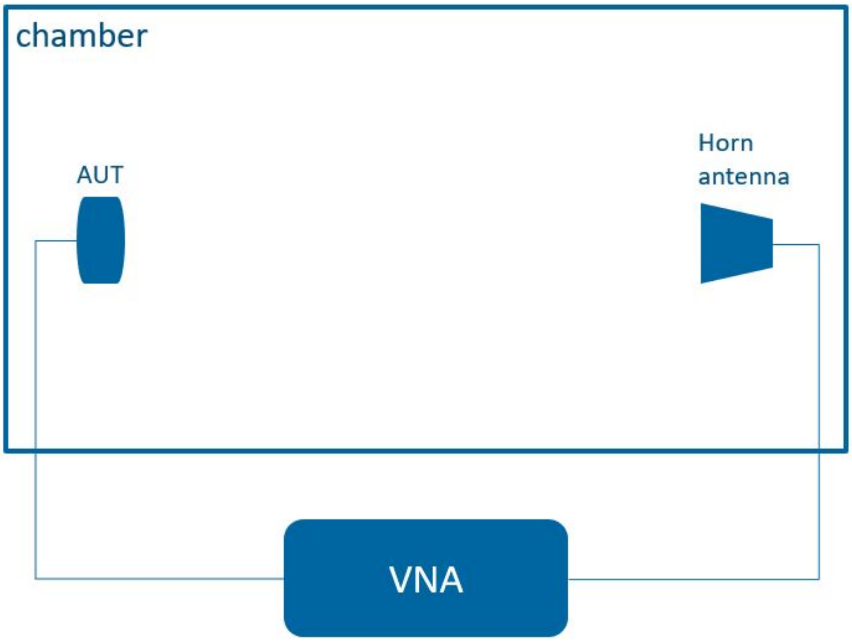

Figure 46: Measurement chamber setup

in a well impedance match at 24 GHz. More details on this patch antenna are given in Section 4.7.

4.7 Patch Antennas

Two patch antennas were designed which were functioning as a reference to the DRA, since the radiation pattern of a patch antenna is comparable to the one of the DRA. A simple quarter wavelength patch is used with an inserted microstripline to have a smooth impedance transition from 50 Ω stripline to patch. Figure 48 shows the reference patch antenna. A simple microstripline structure is used since this is easy to get milled compared to a grounded coplanar waveguide with via holes.

The width of the patch is 5.05 mm and the length equals 3.15 mm, which is around $\frac{\lambda}{4}$. One of the

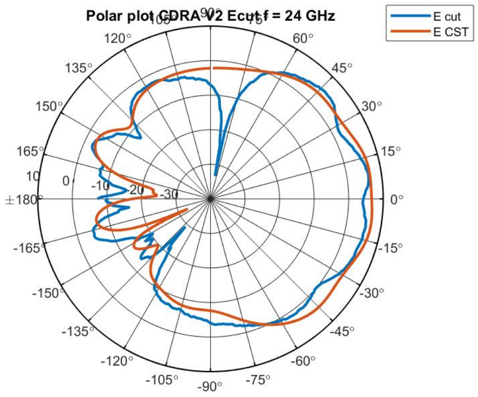

(a) E cut of V2 board at 24 GHz

(b) H cut of V2 board at 24 GHz

Figure 47: Comparison of measurement data of fabricated V2 DRA versus CST simulations for E- and H-plane

bigger uncertainties that happens with this milling machine is the fact that it is not exactly known how far the machine mills away the copper. Therefore, the soft Rogers substrate is easily to be milled out together with the copper. To take this into account, the patch antenna simulation is made with a slightly thinner rogers board assuming 0.05 mm being milled away and with a slightly larger patch (+0.05 mm) to match this board thickness.

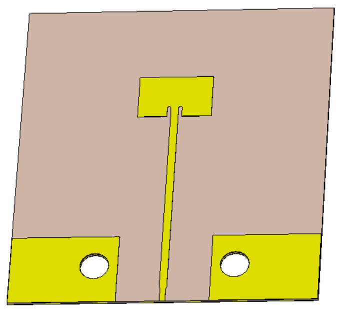

Figure 48: Patch antenna

The PCB fabrication milled 0.069 mm away from the Rogers substrate resulting in a substrate thickness of 0.185 mm around the antennas. The connector is attached under a microscope to make sure the connector pin does not bend when tightening the screws. Since the board is quite thin, too much force on the screws will bend the board on the edges and pushes the board closed to the pin which could potentially damage the connector. Therefore, the connector is not entirely tightened, which likely induces a very small gap between the pin and the stripline. To take this into account the CST simulation is done with shifting the connector slightly above the microstripline. With increments of 0.001 mm, the S11 dip rapidly increases in value. The results of the CST simulated S11 parameters and the measured one of the V1 and V2 board (these should be nearly identical) are shown in Figure 50. The measured data is close to the shifted pin simulation of 0.001 mm and its center frequency with values 23.96 GHz (230 MHz shift) and 24.11 GHz (80 MHz shift) for V1 and V2 respectively. Because the substrate thickness of the boards under the traces is still 0.254 mm, this might be the factor for the slight down shift.

Another uncertainty of the PCB milling is the large surfaces which are not milled out entirely even. With the naked eye one could see that the milling of the copper (and part of the substrate) is not even which means the substrate thickness varies around the antenna.

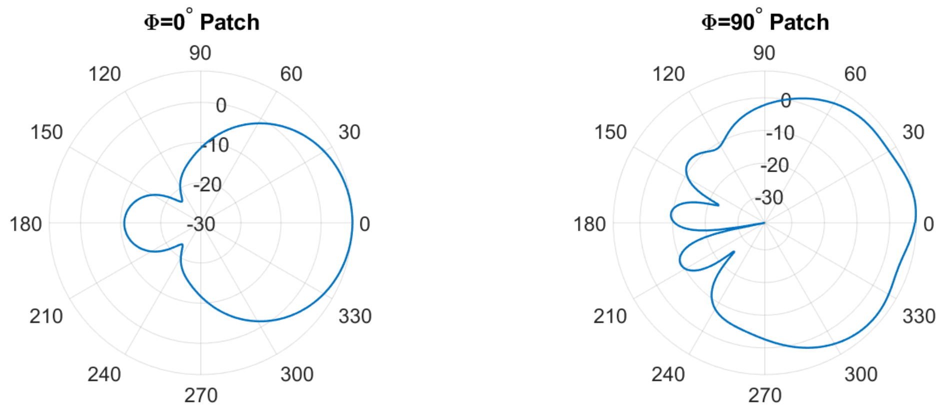

(a) $\Phi = 0$ **(b)** $\Phi = 0$

Figure 49: Farfield radiation patterns for Φ equal to 0 and 90 degrees

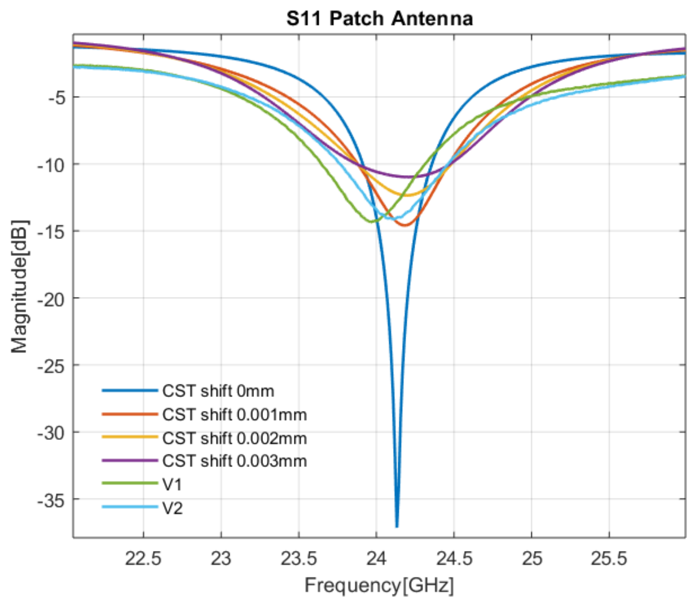

Figure 50: Measured S11 of patch antenna compared with shifted connector data

To make sure the patch antenna works as expected, another measurement is done after a week by calibrating the VNA again. Figure 51 shows the two patch antenna versions and slight difference in magnitude from one measurement to the other. As could be seen from the simulated results, the slight shift is probably caused by a slightly loose connector. The center frequencies of the antennas are very consistent and still cover the ISM band. Compared to the fabricated CDRA, the impedance matching of this patch antenna is much better and therefore the power losses for this antenna are expected to be lower than for the CDRA.

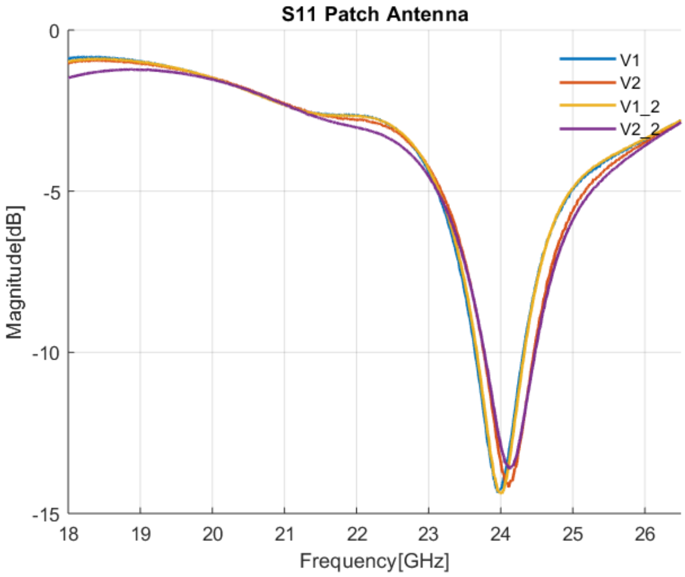

Figure 51: Measured S11 of patch antenna over 2 different days

4.8 Conclusion

An optically transparent cylindrical shaped polycarbonate resonator is used for the DRA. This material has the best conditions regarding the trade-offs between transparency, price and ease of manufacturing. The CDRA will be fed by a microstrip-slot combination and tapered using a grounded coplanar waveguide to the SMA connector pin.

The sensitivity analysis showed that the LEDs did have some influence on the impedance matching, depending on the placement. If the LED edge is more than 2 mm away from the slot edge, the S11 parameters are not significantly influenced. The parameters which suffers the most from manufacturing tolerances were the slot extension and length of the slot which shifted the S11 parameter away from the 24 GHz ISM band. Considering the housing of the antenna the cap had a significant impact on the radiation pattern of the DRA and introduced a second dip in S11. By adding the cap with the backplate to close the antenna entirely, the radiation pattern suffered of dips with magnitudes as small as -10 dB in the field of view. This results in blind spots in the radars field of view and might cause problems for presence detection. One could tweak the DRA again to possibly get rid of the dips in the field of view. The DRA should thus be fine-tuned in its final environment. A dielectric permittivity measurement resulted in slightly different values compared to measured values as documented in literature. For polycarbonate which is a low-cost material and not manufactured for microwave purposes, these small variations are likely to happen.

A final prototype is made to validate the simulation results. There was a big impedance mismatch at the 24 GHz ISM band which is likely caused by the slot resonating at a higher frequency than the SMA connector is specified for. The PCB samples also differs a lot which is likely to be influenced by the way of soldering the connector to the PCB. The S11 influence of the cap was also demonstrated with the prototype, causing 2 dips over the frequency band of interest. The measured radiation pattern of the DRA prototype were slightly varying from the simulated results, but were still within the gain margins in the field of view.

5 Development and Design of Proposed Radar System

This section describes the design choices and implementation of the proposed radar system based on linear frequency modulated continuous wave radar. Two considered radar transceivers were the BGT24LTR11N16 (LTR) [10, 73] and the BGT24MTR11 (MTR) [7, 74]. The former is designed for CW radar and the latter for FMCW automotive applications. Both transceivers have a possibility to control the VCO sweep frequency using hardware- or software-based controllers with a possibility to create custom waveforms. The LTR however has a relatively poor transmit-receive isolation compared to the MTR. The chip package of the LTR is small which makes the cross talk from internal circuitry to receiver significantly large. The quadrature phase imbalance can vary up to 24 degrees from this chip which will significantly increase the error for target detection when using a frequency modulated CW waveform. With the phase change defined by $\Delta\Phi = \frac{4\pi\Delta R_t}{\lambda}$ and assuming a static target, the error in position change of the target will be 0.86296 mm compared to the actual target distance with a phase imbalance of 24 degrees. More details and specifications of the LTR can be found in Appendix C. The MTR radar transceiver has smaller quadrature phase imbalance, less cross talk, better transmit-receive isolation and is thus considered in more detail for the radar application.

5.1 Radar Transceiver BGT24MTR11

The BGT24MTR11 radar transceiver IC of Infineon is made for FMCW purposes and its main function blocks are shown in Figure 52:

- Green: frequency divider with values of 2^4 and 2^{16};
- Blue: amplifiers for the transmitted or received signal;
- Yellow: sensors for temperature, transmit power and local oscillator power;
- Red: VCO for frequency generation, SPI and MUX for controlling the chip and a polyphase filter (PPF) with quadrature mixers resulting in 4 IF outputs.

This transceiver VCO can be swept from 21.5 to 26.5 GHz, covering the 24 GHz ISM band of interest. The VCO is therefore limited between 24 GHz and 24.25 GHz by adjusting the fine and coarse voltage (see Figure 52) to steer the VCO. As the name of the tuning voltage pins suggests, the coarse voltage tunes the VCO frequency with a higher sensitivity of 3 GHz/V while the fine voltage has a sensitivity of 1.5 GHz/V. Figure 53a [7] shows a example measurement of the MTR VCO frequency and tuning voltage dependence with the fine and coarse voltage pins connected, resulting in a summation of the individual tuning sensitivities to 4.5 GHz/V. Figure 53a clearly shows the nonlinearity of the VCO tuning slopes with the lower frequency band of 22 to 24 GHz having an even stronger non linearity. The nonlinearity varies depending on VCO frequency and also strongly over temperature as shown in Figure 53a. A higher temperature shifts the tuning curve to the right, resulting in a higher tuning voltage range to cover the 24 GHz ISM band.

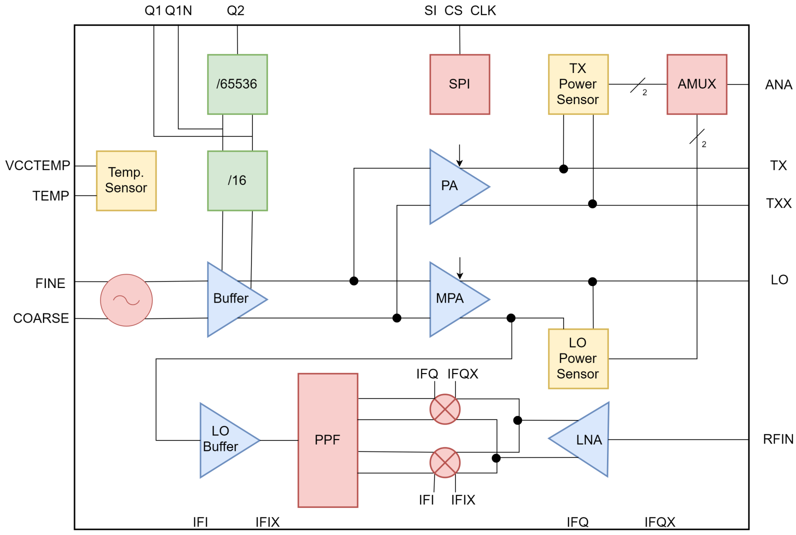

Figure 52: BGT24MTR11 internal circuitry, adapted from [7]

For FMCW radar the sweep linearity is of uttermost importance to get accurate range measurements. Linearization can be done for in software using look up tables or and a hardware-based phase locked loop can be used. The MTR chip also has multiple sensors integrated in its IC, including a local oscillator power sensor (LO Power Sensor), a transmit power sensor (TX Power Sensor) and a temperature sensor, which can be used in case of a software based linearizer to correct for temperature dependencies. Figure 52 also depicts the frequency dividers in green, resulting in divided down frequencies on Q1, Q1N with a factor 2^4 and Q2 divided down with a factor of 2^{16}. The Q1 and Q1N outputs can be used for a hardware-based linearizer and the Q2 pin is mainly used for the software linearizer. Both waveform control methods are described in the next subsections.

Table 9: Parameter specification of Infineon BGT24MTR11 Doppler radar

Parameter	Specifications	Note
Operating frequency range	21.5 - 26.5 GHz	-
Supply voltage	3.3 V	-
Ambient temperature range	-40 C to 105 C	-
Typical TX output power	6 dBm	-
Noise Figure SSB	12 dB	-
Conversion Gain	26 dB	-
IQ imbalance	$\pm$10 deg	-
VCO Phase Noise	-85 dBc/Hz	Typical @100 kHz
Tx,Rx Isolation	30-35 dB	With compensation structures

The transmit pins TX and TXX are a differential output signal with a possibility to be used as a single output signal. When only one antenna is used as transmitter, a balun can be used in case the typical stated transmit power is needed, otherwise one TX pin can be terminated by 50 Ω while the other can be connected by the antenna. The second method however will reduce the output power by 3 dB (factor $\frac{1}{2}$). The phase noise is defined at 100 kHz offset from the carrier as given in Table 9, however for the radar implementation the phase noise close in to the carrier frequency up to the highest beat frequency is of interest. To obtain this phase noise data measurements are performed on the free running MTR chip and on the total system. Other relevant data sheet specifications of the transceiver are given in Table 9.

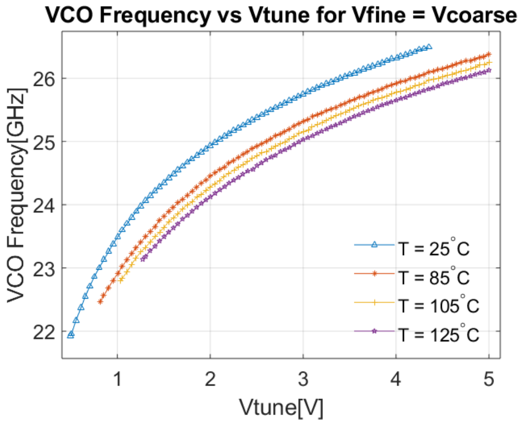

(a) LUT for Vtune = Vfine

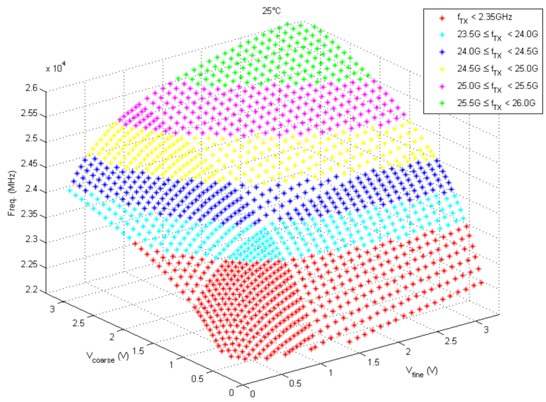

(b) 3D LUT at 25 degrees

Figure 53: BGT24MTR11 LUT for Vfine=Vcoarse in (a) and for different Vfine,Vcoarse on room temperature in (b), both obtained from [7]

5.1.1 VCO Control: Software Based Open Loop

A software controlled open loop can be used to control the MTR which is similar to the approach as shown for the LTR in Figure 79. With the inputs of a frequency divided signal Q2 and a temperature, the tuning voltage can be adjusted for the VCO. The frequency divided signal is read out and compared with a reference waveform to know what the second frequency point should be to get the desired waveform. Using a Look Up Table (LUT) based on the temperature and desired frequency, the needed tuning voltage can be read out and fed to the VCO via a Digital Analog Converter (DAC). However, the to be stored LUT is large and depends a lot on temperature as shown in Figure 53a and Figure 53b. Figure 53b shows the 3D look up table that has to be defined for each relevant temperature change if one would like to also change the fine and coarse tuning voltage separately. Considering the lighting implementation, a drastic change in temperature is likely to happen. With a bulb turned off the temperature inside the bulb (where the transceiver is placed) might be slightly above room temperature, while a bulb turned on can heat up to 100 degrees within milliseconds, requiring the VCO tuning properties to shift and change in sensitivity rapidly.

In addition, Figure 53a and Figure 53b also show the nonlinearity of the VCO frequency with the tuning voltage. For the software based open loop one could program the tuning sensitivity, such that it will correct the VCO frequency. However, since it is an open loop concept there is no feedback on the actual VCO frequency. The adjusted tuning voltage thus needs to be programmed in advance for every temperature range of the bulb and the temperature need to be obtained very frequently. As mentioned before this temperature range covers room temperatures up to more then 100 degrees which would require approximately 70 3D look up tables (if $1°C$ is desired) with each LUT consisting of few hundreds data points as presented in Figure 53b.

Another complication is the normal distributed spread between different fabricated IC samples, resulting in varying the LUT values between different samples. The typical values in the datasheet are obtained by measuring 10 samples which is not sufficient to show the normal distribution between samples. In addition, the defined values for the transmitter and receiver are measured under the most ideal circumstances (such as turning the transmitter off while measuring the receiver or vice versa), which is not achievable to mimic in a realistic product. The chips that are manufactured are thus expected to slightly differ from the data sheet values.

To conclude, making a fixed LUT based on one sample will require many measurements since there is a strong nonlinear dependency on temperature, tuning voltage and resulting output frequency and second it is likely to give significant range errors for different samples of the MTR transceiver. These errors are caused by nonlinearity of the ramp slopes which is likely to happen if a fixed LUT is used for different samples. To eliminate the significance of the transceiver sample, the closed loop linearization seems to be a more suitable alternative because of the feedback that is present.

5.1.2 VCO Control: Hardware Based Closed Loop

The hardware based closed loop concept is a very common method to linearize the frequency sweeps for a FMCW radar. Especially the PLL is frequently used for FMCW radars which corrects the frequency in its loop. The basic elements of the PLL are shown in Figure 19, where the VCO in this case is present in the MTR radar transceiver chip together with a divided-by-16 output. This divider is also part of the total 1/N as shown in Figure 19. The PLL can be used over a predefined frequency band by varying the N divider and keeping the PFD fixed. N as shown in Figure 19 is defined as the total feedback loop divider which equals N*16 in this case. For an integer-N PLL the frequency resolution becomes

$$\Delta f_{int} = \frac{f_{VCO}}{N} \quad [Hz] \tag{70}$$

which shows that a large N is preferred in order to get a small frequency resolution. When the system is in locked state, thus with $f_{VCO} = f_{ref}$, the VCO will have the same frequency accuracy as the Temperature Compensated Crystal Oscillator (TCXO) reference. However, increasing N results in a signal phase noise addition of $20log(N)$ dB. With a fractional-N PLL the relationship between the frequency resolution, N and the reference frequency can be altered. For fractional-N PLL the frequency resolution is defined by

$$\Delta f_{frac} = \frac{f_{VCO}}{N + K/F} \quad [Hz] \tag{71}$$

where f_{ref} represents the reference frequency at the input pins of the PFD and F is the fractional modulus of the circuit.

5.2 Waveform Control with a Phase Locked Loop

Two external waveform generators of Analog Devices based on a phase locked loop were considered, one with the chip ADF4158 and the other with the ADF4159 [8]. The ADF4159 [8] is designed for fast waveform generation. It can generate ramps ranging from hundreds of megahertz in tens of microseconds to tens of hertz in minutes which is better suitable for this application to obtain more design flexibility in waveform generation.

5.2.1 ADF4159 Phase Locked Loop

The functional block diagram for the ADF4159 is shown in Figure 54 where the $\sum - \Delta$ based fractional interpolator in shown in grey. The overall N divider of this fractional interpolator is defined as

$$N = INT + \frac{FRAC}{2^{25}} \tag{72}$$

where INT and FRAC are the integer and fractional parts of the divider. Figure 54 also depicts the 5-Bit R counter, which is part of the reference clock divider. There is also a possible doubler or divider present which can scale the reference input, however the reference input (REFin) lower than 110 MHz due to the limitation in speed of the $\sum - \Delta$ circuit.

Considering the PFD bandwidth (loop bandwidth) there is a trade-off between the noise levels, spurs and lock times. Lower loop bandwidth values will lead to reduced phase noise levels and reference spurs, however at the expense of longer lock times and lower phase margin.

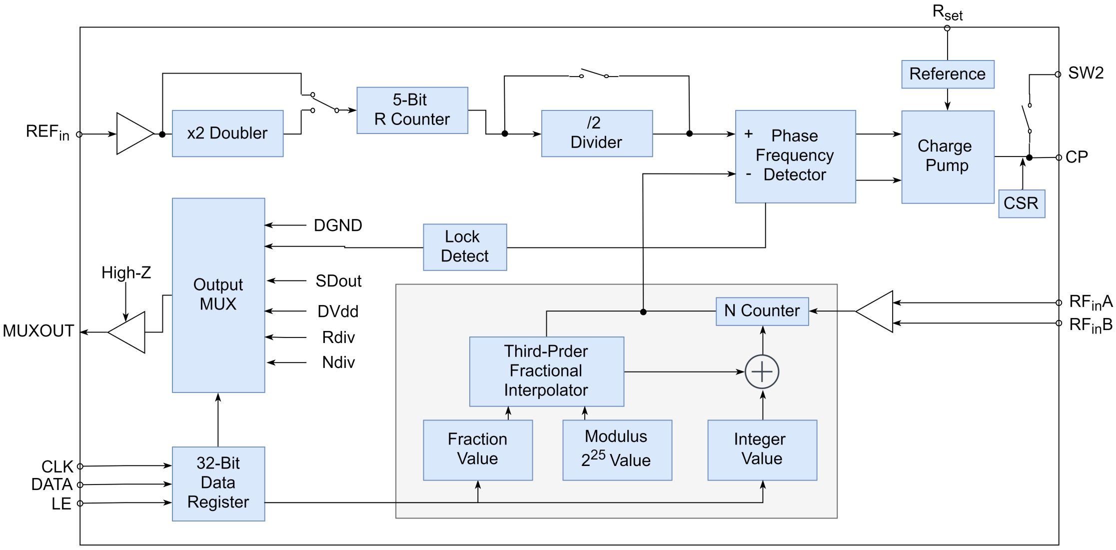

Figure 54: ADF4159 functional block diagram, adapted from [8]

Evaluation boards based on this IC named EVAL-ADF4159xEBxZ are used for test purposes of the radar system. These boards are also called UG-123 and UG-383, depending on the x being a 1 or a 3 respectively. For the 1Z the evaluation board has an on-board VCO for the UG-123 and no VCO for the UG-383. For this application with the MTR11 transceiver the VCO is already present and therefore the 3Z series is selected for this application. More details on the evaluation board can be found in Appendix F.

By connecting the Vtune SMA connection to the Vfine and/or Vcoarse of the MTR evaluation board, the VCO can be controlled. To close the loop, a frequency divided signal (fixed division rate of 16 [7]) is obtained from the MTR11 at pins Q1 or Q1N and fed back to the ADF4159 via the VCO/2 SMA connector, as shown in Figure 55. Since there is only one input SMA connector available for the feedback loop (VCO/2 connector) the other Q1x should be Direct Current (DC) blocked and terminated with a 50Ω load. Radio Frequency (RF) sythesizer waveform parameter settings for the ADF4159 chipset are computed in Appendix F resulting in a TCXO reference frequency of 50 MHz.

5.2.2 Loop Filter

The PLL evaluation board does not have a loop filter implemented because this should be matched to the VCO. The loop filter has a significant impact on the PLL performance and influences the following PLL design parameters:

- filter comparison frequency: remove unwanted components of the phase detection/ comparison frequencies;
- loop stability: filter should be defined to give a required fall in loop gain at the unity gain point for the loop;
- transient response: loop filter can slow down or speed up the loop response with a smaller and wider bandwidth, respectively.

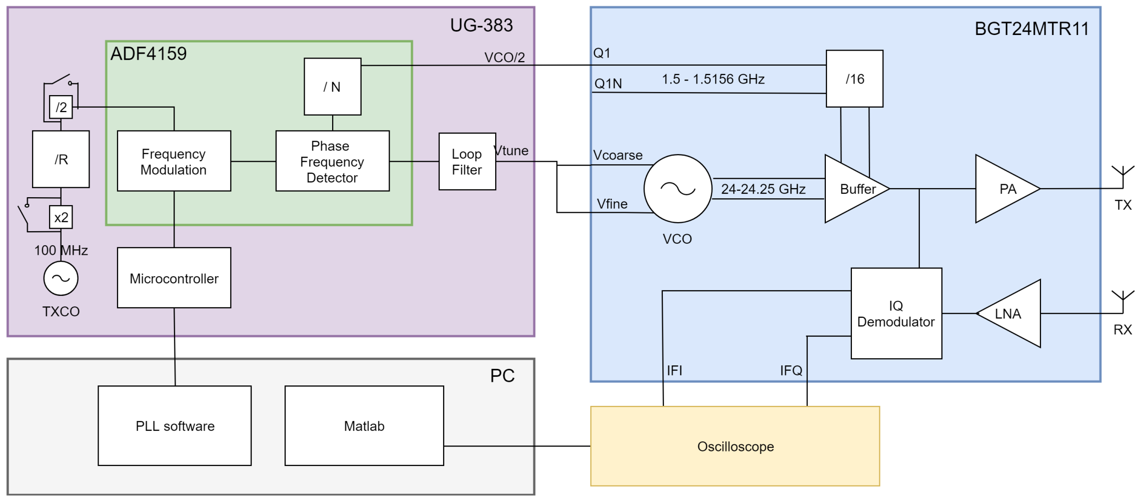

Figure 55: FMCW system block diagram with evaluation boards included.

The software ADIsimPLL corresponding to the ADF4159 is used to design a loop filter for the specific chip with the external phase noise of the VCO taken into account.

The PLL output jitter is mainly dominated by the reference noise source and the internal VCO noise. The reference noise includes jitter generated by PCB noise coupling, power supply noise and reference timing source. The VCO noise includes the VCO amplifier components and power supply noise. If the reference signal has a significant amount of jitter present, using a low PLL bandwidth will decrease phase noise contribution of it in the output signal. However, using a small PLL bandwidth will increase the VCO phase noise in the output signal. Therefore, a trade-off decision must be made between the VCO and reference signal jitter.

The PLL loop bandwidth is affected by the loop filter bandwidth and has a tradeoff between lock time and PLL controllability. With a higher PLL loop bandwidth the lock time will be reduced but making the PLL harder to control. The loop filter bandwidth and lock dependence is depicted in Figure 56b. The phase error also depends on the loop bandwidth as shown in Figure 56a. A higher loop bandwidth results in a lower phase error. However, making the loop bandwidth too high will increase the frequency error. A trade-off should be made between the phase and frequency error.

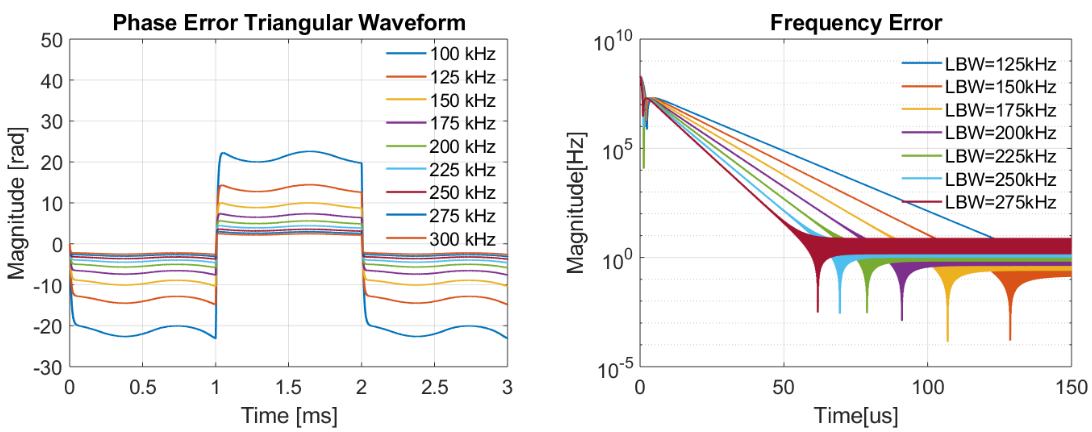

(a) Phase error **(b)** Absolute frequency error

Figure 56: Phase and frequency error for a triangular waveform and frequency change, respectively

Since the reference is not part of the correcting loop as shown in Figure 19, Phase Noise (PN) present in the reference oscillator will be amplified through the loop gain. In general, a higher loop bandwidth is preferred when the input reference is clean. A clean input reference is a crystal oscillator for example with a PN around -100 dBc/Hz in the kHz range. If a FPGA reference is used for example, the reference is likely to be noisier which requires jitter cleaning. For these noisy references with a PN around -80 dBc/Hz in the kHz range, the loop bandwidth should be low to achieve the jitter cleaning. However, setting the loop bandwidth to a lower value results in a PLL output which is more dependent on the VCO close to the carrier frequency, as depicted in Figure 58. With higher levels of PN close to the carrier frequency, small detected targets are likely to be masked in the PN of the transmitted signal. In addition, the phase noise will increase for increased loop bandwidth causing the phase frequency detector to have more troubles with locking to the right frequency. Ideally, the loop bandwidth should have a value which let the PLL output benefit from the low PN of the reference oscillator close to the carrier frequency and at far offset frequencies from the low VCO noise floor.

Active Loop Filter

The schematic of the total system is shown in Figure 57 with the prescaler of factor 16 implemented in the MTR chipset VCO output. The loop filter configuration implemented by default on the evaluation board is an integrator with a pre- and post low pass filter added to increase the frequency roll-off. The zero of the loop filter is formed by R2C2 and the three poles are represented by components R1C1, R2C3 and R3C4.

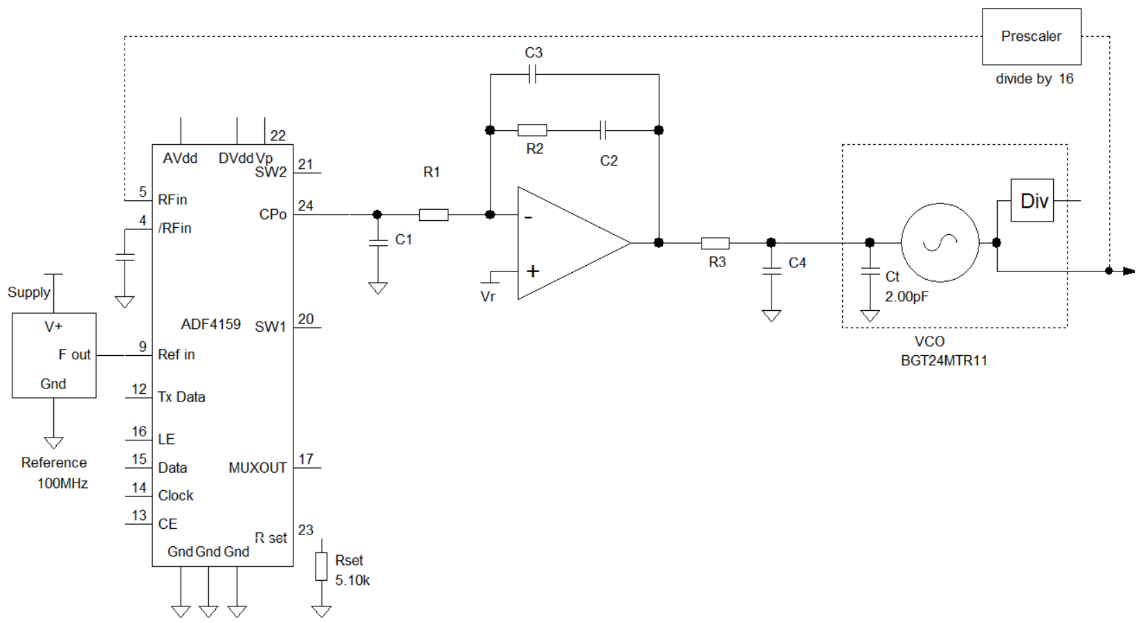

Figure 57: Schematic of simulated PLL, obtained from ADIsimPLL

The component values of the loop filter are calculated based on a defined loop filter bandwidth and phase margin. The loop filter bandwidth is selected such that the frequency error and phase error are acceptable and the total phase noise is relatively low. To observe the influence of the loop bandwidth on the total PLL phase noise different PLL phase noise has been plotted for different loop bandwidths in Figure 58. From this figure it can be seen that there is a clear trade-off between the faster lock time (larger filter bandwidth) over higher levels of phase noise at frequencies above 200 kHz. Regarding the lock time for the chosen bandwidth from Figure 56b, one could see that for 100 Hz error the loop filter bandwidth of 125 kHz results in a 102.2 μs while the 300 kHz bandwidth only needs 46.35 μs to get to the same frequency error. For a slow ramp or triangular waveform with a ramp duration in ms, the 100 kHz loop bandwidth will be fast enough to lock the frequency for the linear waveform generation.

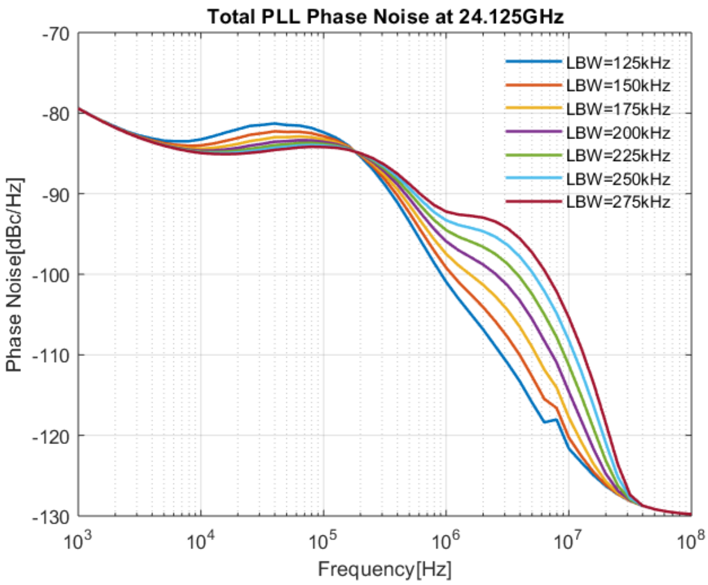

Figure 58: Total PLL phase noise

The phase margin influences the overshoot for frequency lock which is chosen to stay within the ISM band from 24 GHz to 24.25 GHz. The sweep bandwidth was chosen to be 200 MHz, leaving 25 MHz for under and overshoot.

ADIsimpLL is used to simulate the overshoot for different phase margins as shown in Figure 59. The minimum phase margin needed to stay within a overshoot of 25 MHz equals 69 degree. The component values determine the phase margin and therefore small variation in the component values will change the phase margin by a few degrees which can be enough to exceed the 24 GHz ISM band. To avoid this, the phase margin is increased to 70.2 degrees by taking the 1% component tolerances into account. The resulting overshoot with the chosen phase margin is shown in Figure 59b where the overshoot and the frequency error relative to the defined frequency is shown. The peak value of the overshoot in Figure 59b equals 24.2406 GHz which is within the ISM band. For the undershoot in Figure 59a the lowest frequency equals 24.009 GHz which is still in the ISM band with 8.778 MHz space for component tolerances which might be higher than the computed 1%. Regarding the frequency error around 90 μs the frequency error is already smaller than 10kHz.

A analysis based on the triangular and sawtooth modulation for a phase margin of 66° and a modulation period of 1 ms (worst case scenario), is shown in Table 10. The bandwidth is varied with resulting phase and frequency errors which are of interest. One could observe that the phase error decreases for increasing loop bandwidth while the frequency error increases. Since the PFD takes both the phase and frequency errors into account, the loop bandwidth that is most suitable ranges from 200 to 250 kHz. The phase and frequency error are slightly larger for the sawtooth waveform compared to the triangular one which can be explained by the overshoot between the end of a sawtooth ramp and the start of a new one.

Table 10: ADIsimPLL Triangular and Sawtooth Chirp Analysis for PM=66°, $T_m = 1\text{ms}$

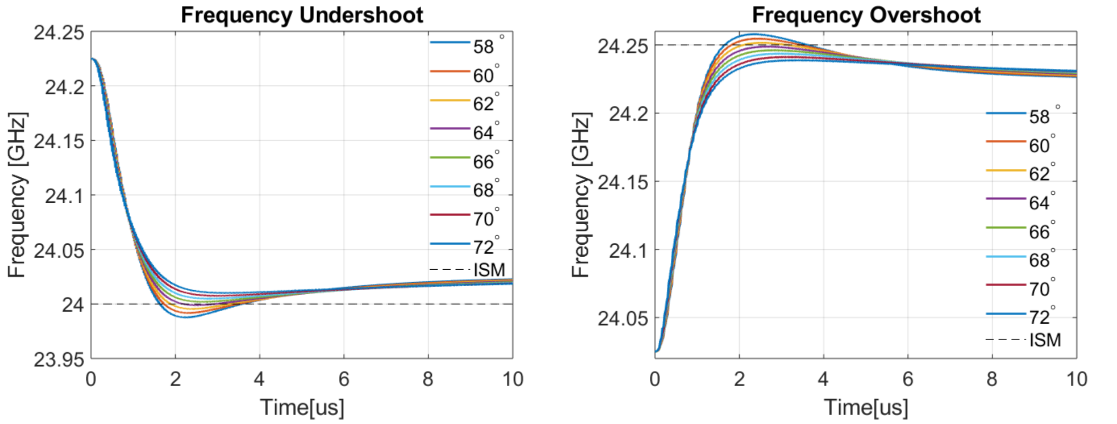

(a) Frequency undershoot

(b) Frequency overshoot

Figure 59: Frequency under and overshoot for varying phase margin at a loop bandwith of 218 kHz

Parameter | BW [kHz]	125	150	175	200	225	250	275
Chirp Rate [kHz/us]	-200.3	-200.29	-200.28	-200.28	-200.28	-200.28	-200.28
Chirp Rate Error [Hz/us]	-25.9	-17.5	-12.5	-9.23	-7.05	-5.5	-4.38
Freq. Dev. RMS [kHz]	34.4	26	20.7	17.6	15.9	15.3	15.6
Freq. Dev. Peak [kHz]	457	384	338	301	270	244	222
Phase Error[deg]	791	547	400	304	238	192	157
Freq. Error[kHz]	1.07	1.24	2.14	3.66	5.71	8.16	10.95
Chirp Rate[kHz/us]	201.54	201.34	201.18	201.04	200.93	200.84	200.76
Chirp Rate Error[kHz/us]	1.27	1.07	0.907	0.771	0.66	0.568	0.492
Freq. Dev. RMS[MHz]	1.63	1.49	1.38	1.27	1.17	1.07	0.974
Freq. Dev. Peak[MHz]	21.5	21.7	21.8	21.9	22.1	22.2	22.1
Phase Error[deg]	-802	-555	-406	-310	-243	-196	-161
Freq. Error[kHz]	1.08	0.226	-1.04	-2.82	-5.04	-7.62	-10.5

Table 11: Loop filter components of the active loop filter

Component	Value	Unit
R1	220	Ω
R2	180	Ω
R3	330	Ω
C1	120	pF
C2	27	nF
C3	390	pF
C4	270	pF

The loop filter components as selected for the active loop filter are given in Table 11 with resulting open and closed loop gain at 24.125 GHz in Figure 60. The frequency where the open loop gain is 0 dB equals the loop bandwidth of the loop filter which equals 218 kHz. The phase margin can also be found from the open loop gain plot at the loop bandwidth frequency of the loop filter which equals (180 - 113) 67°.

The VCO gain K_v is computed using the single sideband phase noise (Figure 61b) which is obtained by the phase noise measurement on the MTR board. From Figure 61a it can be seen that the sensitivity of the MTR reaches up to 4.6 GHz/V which is relatively high since typical VCO sensitivities are in terms of MHz. Small errors in the tuning voltage will result in large frequency shifts. However, for the ISM band only part of the tuning voltage range is used. Depending on the chip operating temperature the tuning voltage in ISM band varies around 1.2 to 2.2 V, resulting

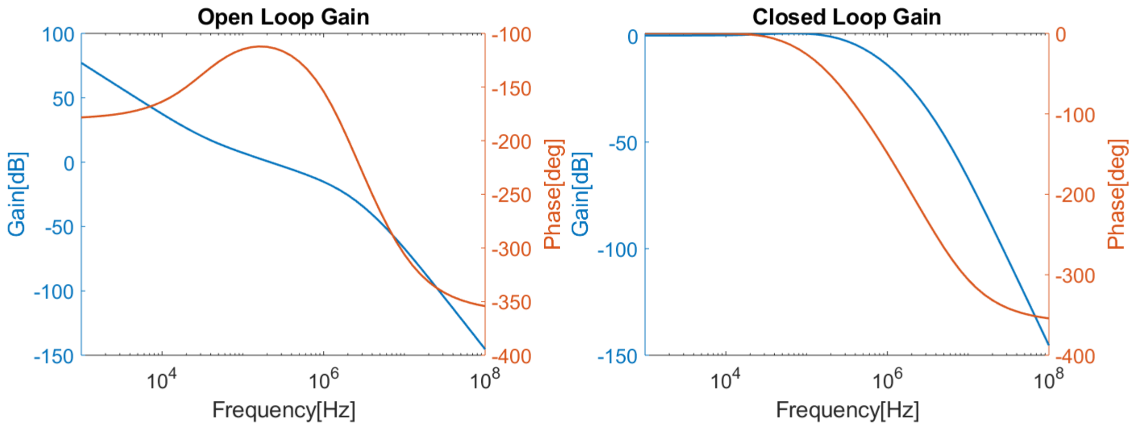

(a) Open loop gain

(b) Closed loop gain

Figure 60: Simulated open and closed PLL loop gains

in a sensitivity range of 0.8 to 2 GHz/V.

The resulting PLL phase noise is shown in Figure 62 where the crystal reference oscillator and prescaler dominates at lower frequencies and the $\sigma\Delta$ modulator and VCO are dominating at higher frequencies. This was expected, because the reference and prescaler are not part of the loop which filters the phase noise. It is of uttermost importance that the prescaler and reference are low noise sources. Comparing the VCO phase noise in Figure 61b with the one in Figure 62, one could see that the VCO phase noise is lowered with 75 dBc at lower frequencies which confirms the functioning PLL.

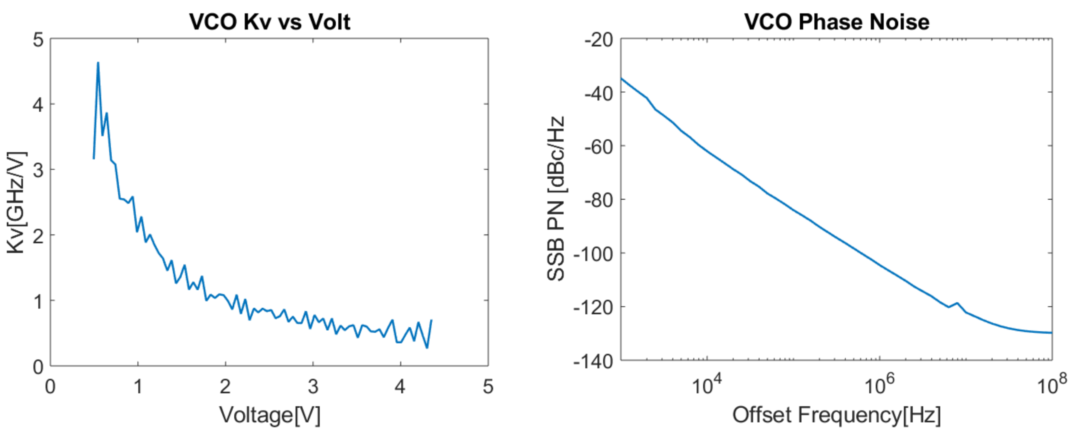

(a) Kv as function of tuning voltage

(b) VCO phase noise

Figure 61: Simulated VCO phase noise and Kv dependence on tuning voltage at room temperature

Passive Loop Filters

Besides the active loop filter also a passive loop filter has been considered for the design. With the charge pump output on the evaluation board an external loop filter can be used.

Three loop filters are selected as shown in Figures 63 and 64 which are relatively simple and can be simulated in ADIsimPLL. Different bandwidths and phase margins were used for these

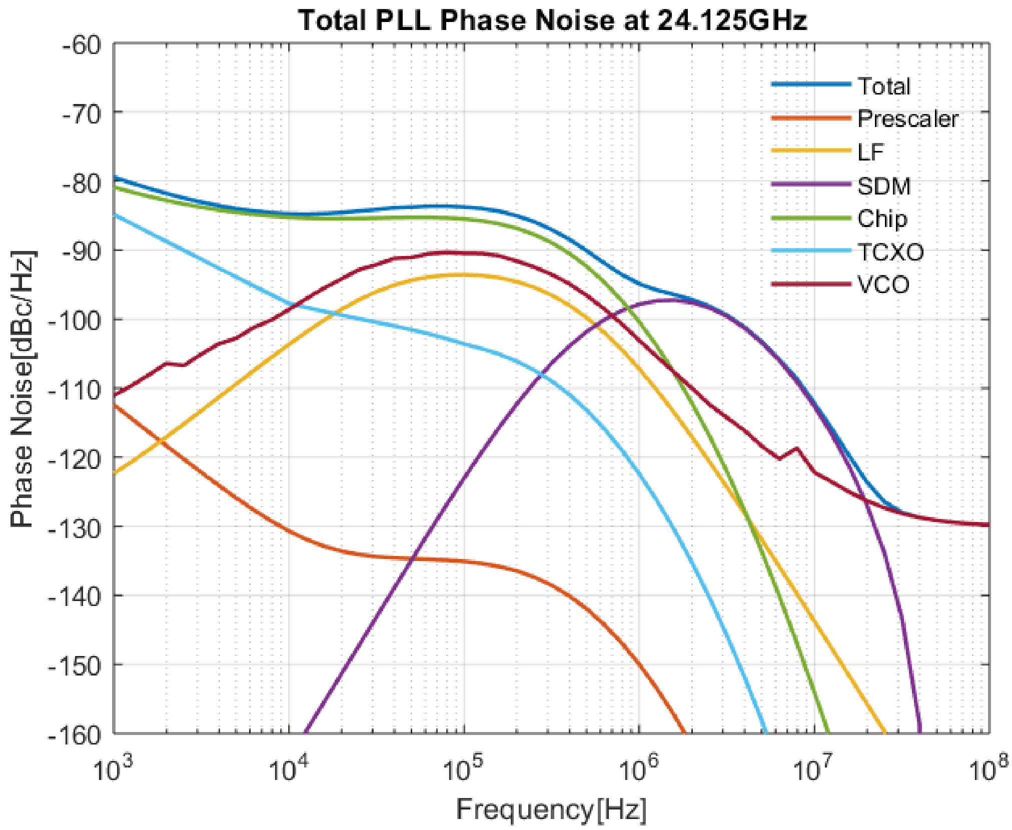

Figure 62: Simulated PLL phase noise of all loop components and the total

filters for testing purposes of the radar system. The values selected for the loop filter are given in Table 12,Table 13 and Table 14 for filter 2C, 3C and 4C, respectively.

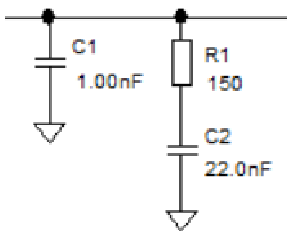

Figure 63: 2C passive loop filter with 2 capacitors

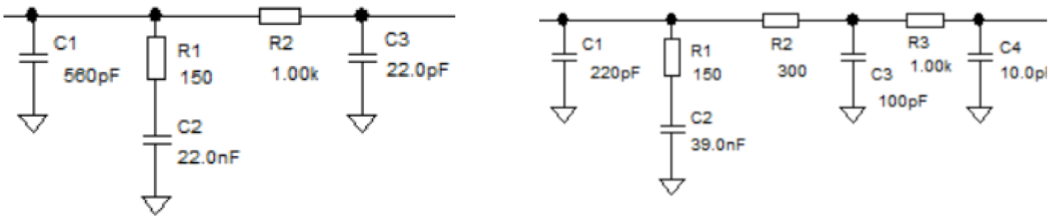

(a) 3C passive loop filter with 3 capacitors

(b) 4C passive loop filter with 4 capacitors

Figure 64: Passive loop filters considered for the radar system

Table 12: Loop filter components of the 2C passive loop filter resuling in a loop bandwidth of 252 kHz and phase margin of 66.4°

Component	Value	Unit
R1	150	Ω
C1	1	nF
C2	22	nF

Table 13: Loop filter components of the 3C passive loop filter resuling in a loop bandwidth of 229 kHz and phase margin of 69.3°

Component	Value	Unit
R1	150	Ω
R2	1	$k\Omega$
C1	560	pF
C2	22	nF
C3	22	pF

Table 14: Loop filter components of the 4C passive loop filter resuling in a loop bandwidth of 231 kHz and phase margin of 75.7°

Component	Value	Unit
R1	150	Ω
R2	300	Ω
R3	1	$k\Omega$
C1	220	pF
C2	39	nF
C3	100	pF
C4	10	pF

The resulting total phase noise of the system is given in Figure 65. One could see that the slight variation in bandwidth and phase noise influences the total PLL phase noise slightly. All passive filters close in phase noise is -80 dBc/Hz or less, which was the maximum phase noise level to detect humans with the given transmit powers. A chirp analysis is shown in Table 15 for the passive filters with a modulation time of 1 ms. Compared to the chirp analyses on the active loop filter, the chirp rate error, frequency deviation peak and phase error have been drastically increased for the passive loop filters.

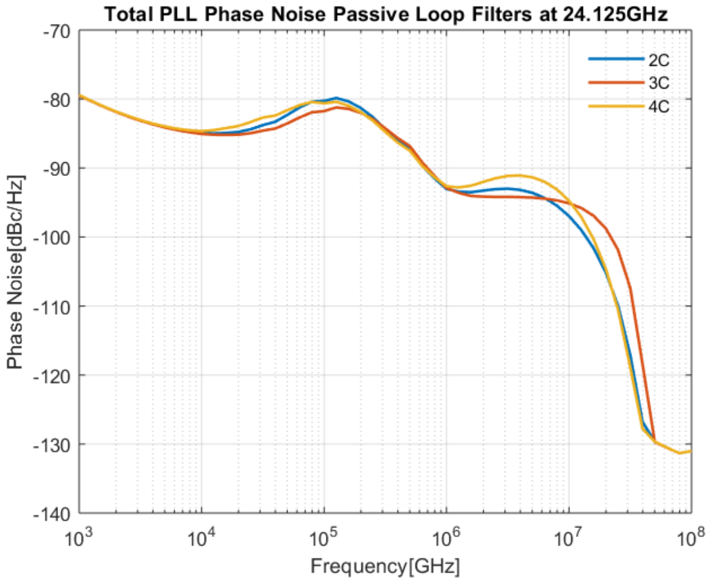

Figure 65: Total PLL phase noise for passive filters

Table 15: ADIsimPLL Triangular and Sawtooth Chirp Analysis for passive filters for $T_m = 1\text{ms}$

Parameter	2C	3C	4C
Chirp Rate [kHz/us]	-200	-200.27	-200.27
Chirp Rate Error [Hz/us]	-2.92	-4.52	-9.04
Freq. Dev. RMS [kHz]	15.4	14.5	18.2
Freq. Dev. Peak [kHz]	271	259	269
Phase Error[deg]	142.14	160.14	16.47
Freq. Error[kHz]	-34.71	15.40	283.86
Chirp Rate [kHz/us]	200.97	200.27	200.27
Chirp Rate Error [Hz/us]	695	637	693
Freq. Dev. RMS [MHz]	1.56	1.4	1.09
Freq. Dev. Peak [MHz]	36.6	29.3	17.5
Phase Error[deg]	-141.73	-159.67	-282.86
Freq. Error[kHz]	-53.30	-15.71	-16.8-

5.3 Conclusion

The BGT24MTR11 radar transceiver IC is chosen due to its design especially for FMCW radar which results in better performance compared to the LTR transceiver. The transceiver tuning voltage characteristic vs VCO frequency is strongly dependent on temperature. Because lighting applications have drastic temperature changes, a hardware based closed loop is used to compensate for this temperature dependence and to avoid the chip sample variation.

A phase locked loop based waveform generator is used to tune the voltage of the VCO and a feedback loop is created with the divided down VCO frequency. To match the PLL with the VCO on the MTR, different loop filters were designed. The active loop filter is by default used on the evaluation board. Because this filter cannot be checked externally, some passive loop filters were simulated with slightly different loop bandwidths and phase margins which functions as test loop filters for the system.

6 Evaluation of Proposed Radar System

The proposed radar system as described in the previous section is evaluated by measurements. The MTR board and ADF board are first tested separately and afterwards connected together as a system.

The connectors and pins on the MTR and ADF board are shown in Table 16 with their frequency of operation and function included.

Table 16: Connectors of MTR & ADF evaluation board

Name	Type	DC	Frequency	Function
TX	SMA	n	24 - 24.25 GHz	differential TX input
TXX	SMA	n	24 - 24.25 GHz	differential TX input
LO	SMA	n	24 - 24.25 GHz	local oscillator output
RFIN	SMA	n	24 - 24.25 GHz	RX input
IFI	SMA	y	0 - 10 MHz	differential IF I output
IFIX	SMA	y	0 - 10 MHz	differential IF I output
IFQ	SMA	y	0 - 10 MHz	differential IF Q output
IFQX	SMA	y	0 - 10 MHz	differential IF Q output
FINE	pin	n	-	fine tuning voltage
COARSE	pin	n	-	coarse tuning voltage
Q1	SMA	y	1.5-1.5126 GHz	differential 2^4 frequency divider output
Q1N	SMA	y	1.5-1.5126 GHz	differential 2^4 frequency divider output
Q2	pin	y	22.89-23.13 kHz	2^{20} frequency divider output
SPI	pin	n	-	SPI parameters input
ANA	pin	n	-	analog output
REFIN	SMA	n	f_{ref}	external reference input
TXDATA	SMA	n	-	transmit data output
CPOUT	SMA	n	-	charge pump output
VCO/2	SMA	n	1.5-1.5126 GHz	VCO loop input
VVCO	SMA	n	$f_{VCO,ob}$	on-board VCO voltage output
EXT_VCOOUT	SMA	n	$f_{VCO,ob}$	on-board VCO output
VTUNE	SMA	n	-	tuning voltage output
USB	-	n	-	connects to a computer

6.1 MTR Board Evaluation

This section covers the functional tests carried out on the MTR board. The detailed steps for connecting the MTR board to the test equipment is described in Appendix H.1. The frequency-tuning voltage dependence of the VCO is first tested, followed by phase noise measurements on different outputs of the MTR.

6.1.1 Frequeny - Tuning Voltage Dependence

First, a functional test is done on the MTR board by connecting it with the TX connector to a scope and using a function generator to feed the tuning voltage pin(s) with voltages which should result in ISM band frequencies, as shown in Figure 53a. The unused connectors are terminated by 50 Ω loads and the Q1 and Q1N are DC blocked. To control the MTR board, an SPI needs to be configured by a 16-bit sequence. An arduino micro is used with SPI connection to serve as a master device for the MTR board which is an input-only device.

From the PLL board only one tuning voltage is available through VTUNE, which limits the possibility of tuning Vfine and Vcoarse with different voltages simultaneously. If any of the tuning voltage pins is left open it will be internally connected to Vcc with a pull-up resistor. Therefore leaving both of them open will result in a Vcc voltage on both pins around 3.3 V, which equals to a frequency output around 26 GHz at room temperature as shown in Figure 53b. In addition, the tuning voltages should be higher than 0.5 V at any time to have the VCO operate correctly as defined in the MTR userguide [7].

The result of the tuning voltage output is given in Figure 66a where first the Vcoarse pin is swept from 0.5 to 4.5 V with steps of 0.1 V, then the Vfine is swept with the same tuning voltage range and the last measurement is with Vfine connected to Vcoarse. The horizontal lines in Figure 66a show the 24 GHz band limits. Tuning the Vfine while leaving Vcoarse open does not cover the ISM band and is therefore not suitable for this 24 GHz radar application. As mentioned before, the tuning voltage pins should always be above 0.5 V and the chip should also work at lower temperatures (shifting the graph upwards) and therefore the Vfine=Vcoarse setup is selected for the tuning.

To validate the measurements of the VCO frequency compared to the tuning voltage output, the datasheet [7] values are used as a reference. A comparison was done by plotting the measured Vfine=Vcoarse data with the reference measurements as shown in Figure 66b. The shape of the measured graph is comparable to the reference graph measured at room temperature ($T = 25°$). The graphs were overlapped by shifting the measured graph down with 660 MHz, resulting in an almost perfectly overlap. Some small errors might have been neglected during the measurement such as the exact tuning voltage input at the pins compared to the one defined on the voltage supply. This did vary with a 2 mV in some cases, which would result in a frequency error of 9 MHz at most (assuming 4.5 GHz/V sensitivity) which is relatively small. This could thus not have caused the 660 MHz shift. The constant upward shift of 660 MHz is around 2.75% error which is however quite reasonable for a sample spread.

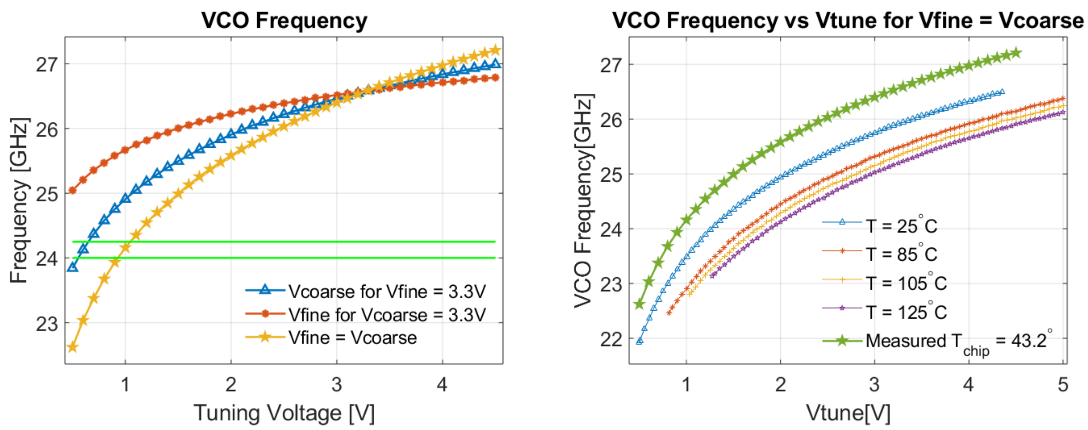

(a) Measured varying tuning voltages

(b) Comparison of Vfine=Vcoarse with datasheet

Figure 66: Tuning voltage measurements for Vfine with Vcoarse left open, visa versa and Vfine connected to Vcoarse

The slight nonlinearity of the VCO tuning voltage characteristics is shown in Figure 67b for the 24 GHz ISM band. Errors up to 20 MHz are present compared to a linear fitted line which is a 10 % error in terms of the sweep bandwidth.

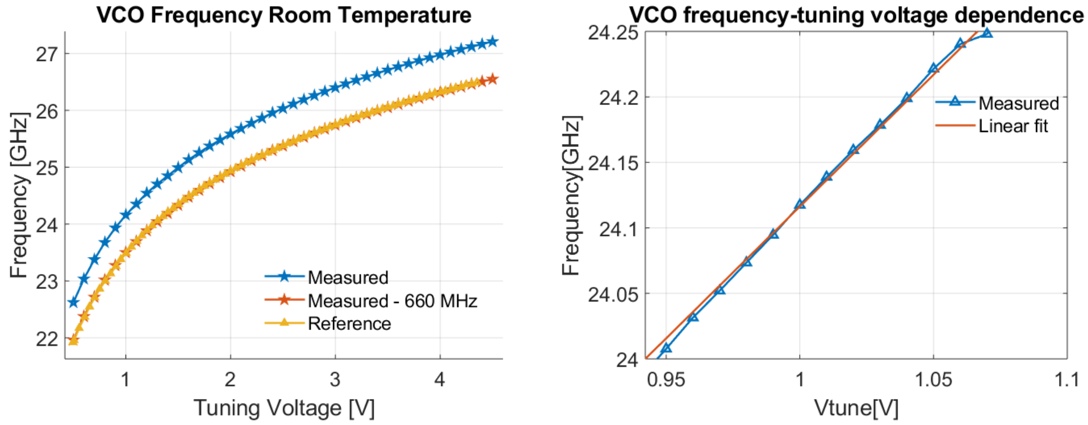

(a) Comparison tuning voltage at $T = 25^\circ$ **(b)** Tuning voltage in ISM band

Figure 67: Tuning voltage measurements for Vfine connected to Vcoarse

6.1.2 VCO Phase Noise

The phase noise can be directly measured by a spectrum analyzer (Figure 68) as long as the analyzer noise floor does not exceed the VCO phase noise. With the built-in phase noise measurement function on the spectrum analyzer, the analyzer noise bandwidth and circuitry are corrected for the phase noise measurement. The direct measurement method is not able to differentiate between amplitude and phase noise. However, with measured data from another sample of the LTR transceiver where the AM noise was measured to be below -130 dBc/Hz for different temperatures (from -40 to 25 degrees) and Vcc voltages, which is low enough to not influence the phase noise (FM) significantly. For the similar and more high-end MTR radar transceiver this AM noise is assumed to be equal or lower compared to the measured LTR noise.

The transmit output TX and TXX is a differential output which can be changed to a single output by terminating one of the TX outputs with 50Ω. This will however decrease the output power by 3 dB. If the full output power is desired, a balun can be placed in between the differential output and antenna. However, external baluns operating at 24 GHz are not sold but have to be custom designed. Using a microstrip analysis for Rogers 4350B 0.254mm thickness substrate at a frequency of 24.125 GHz, the length of the stripline for a balun equals 1.85 mm (for an electric length of 90 degrees). The total balun length should then be twice the stripline length which results in a board smaller then 4 mm in length. Since a transition needs to be made or an substrate inserted microstripline is needed with small via holes and very small trace spacings, the price for an external balun would increase rapidly and is therefore not further considered for this thesis.

Since the phase noise measurement is expected to be very sensitive, different measurements are done on the board by using a different type of cables and power supplies. The reference used if the VCO phase noise as defined in the datasheet which should be within -85 dBc/Hz to -75 dBc/Hz at 100 kHz offset. From Figure 69 one could see that the measured phase noise at 24 GHz is within the data sheet reference limits as shown by the dots. For these phase noise measurements the external battery was used with twisted cables and the display turned off.

6.1.3 Divider VCO Phase Noise

The divided down phase noise is measured through the output Q1 and is shown in Figure 70 with a tuning voltage varying from 0.9 to 1.1 V to covers the 24 GHz ISM band. The center frequency did vary around by tens to hundreds of kHz at a same tuning voltage and needed some start up

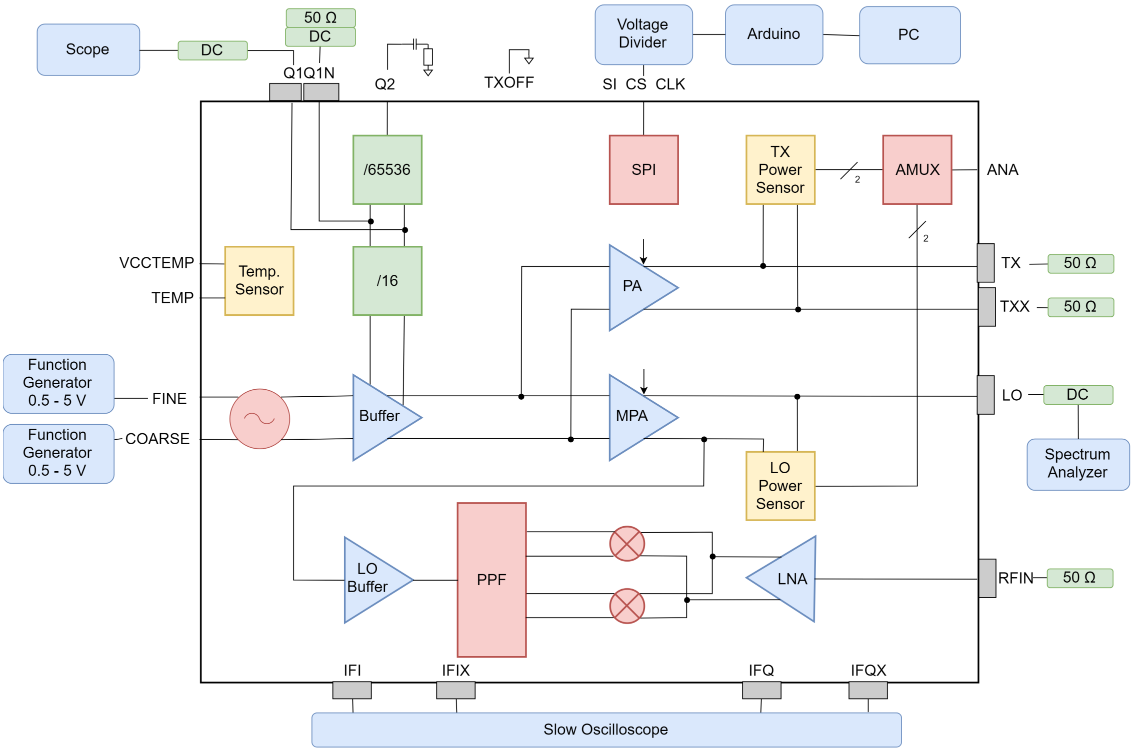

Figure 68: Measurement setup for VCO phase noise, board scheme adapted from [7]

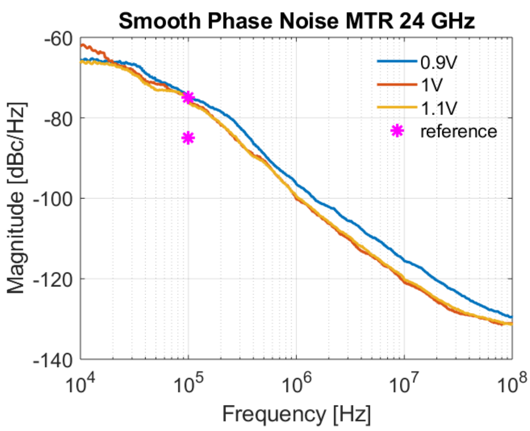

Figure 69: Phase noise MTR

time. When powered up, the frequency started with hundreds of kHz higher and shifted slowly to the more stable center frequency.

Another phase noise measurement was done with just the Vcoarse connected and by varying the voltage between 0.55 and 0.65 V. By adding one or two absorbers and setting the search span of the center frequency peak, different slightly different phase noise was measured as shown in Figure 71b. Different measurement methods were used for the phase noise measurement to compare the impact of external electronics and connections. Figure 71a clearly shows a difference in using a battery feed for the MTR board while measuring the phase noise. Especially below 10 kHz from the center frequency resulted in a better phase noise measurement by using a battery for circuitry power. By turning the battery display off, the phase noise measurement close in became even more accurate,

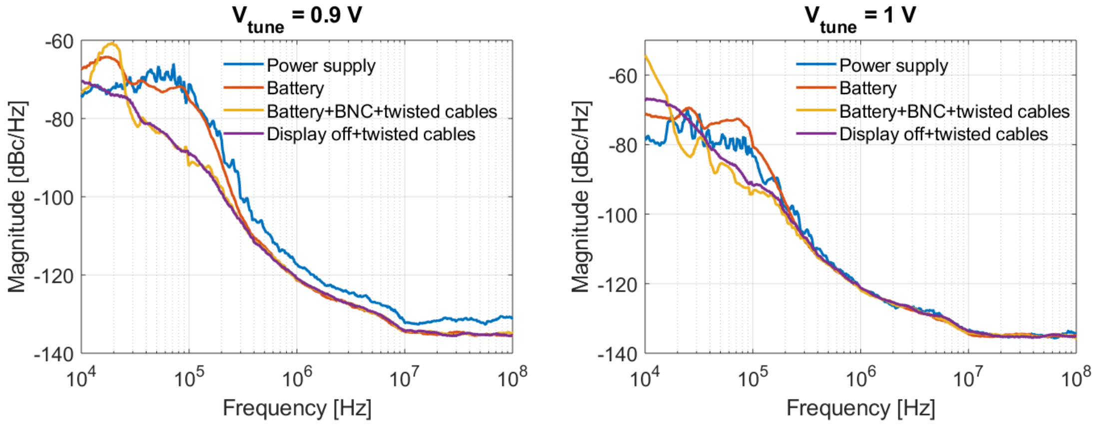

(a) Divided down phase noise at Vtune = 0.9 V **(b)** Divided down phase noise at Vtune = 1 V

Figure 70: Divided down VCO phase noise for Vfine=Vcoarse at different tuning voltages and with different measurement setups

resulting in a decaying phase noise graph as expected from a typical VCO response.

Comparing the phase noise plots for different tuning voltages in Figures 70 and 70a showed some differences between the measurements under the same conditions. It can therefore be concluded that the phase noise changes slightly for different center frequencies.

In an ideal case the divided down phase noise should be 20logN (=24 dB for N=16) dB lower compared to the phase noise measured at 24 GHz. If the smoothed phase noise is shifted upwards by 24 dB, the phase noise exceeds the 24 GHz specified datasheet values, which are given by two stars in Figure 71b. This is expected since the frequency dividers and measurement equipment also have some phase noise.

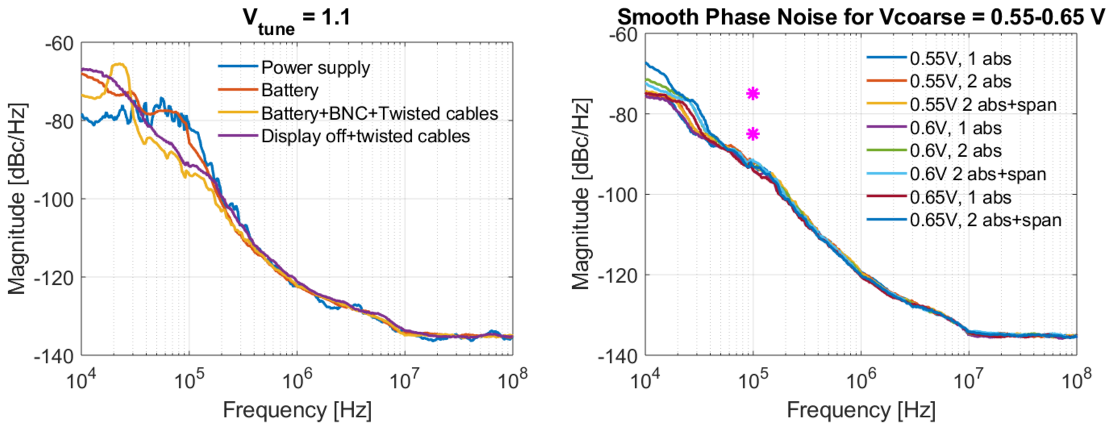

(a) Divided down phase noise at Vtune = 1.1 V **(b)** Divided down phase noise for Vcoarse

Figure 71: Measured phase noise for Vcoarse=Vfine connected and for Vcoarse only with a tuning voltage from 0.55-0.65 V to cover the ISM band

Transmit Power Tests

The transmit power of the MTR chip was measured through to check if these align with the data sheet values. The output power of the TX, TXX and LO are measured directly with DC block and cable connected to the spectrum analyzer. The transmit powers obtained with the antennas are measured by using two identical designed antennas. One antenna is connected to the TX port of the MTR board, while the TXX is terminated with 50Ω, and the other antenna is directly connected with a DC block to the spectrum analyzer.

The measured powers are shown in Table 17 which is 6-7 dB lower for maximum values of TX, TXX and LO compared to the datasheet values of 6 dBm and 0 dBm for the TX,TXX and LO, respectively. These losses are likely because the transmit-receive isolation which is worse when both the transmit and receive antennas are turned on, in contrast to the ideal measured situation for the datasheet values where one of the transmit or receive connection is turned off. The transmit power however is much lower than assumed before, resulting in a smaller detection range.

Table 17: Peak power measured

Output	Power	Datasheet	Units	Comment
TX	1.33	6	dBm	maximum TX power, terminated TXX
TXX	0.17	6	dBm	maximum TX power , terminated TX
LO	-10	-3	dBm	low power LO
LO	-6	0	dBm	high power LO
CDRA	-8.201	-	dBm	prototype
patch	-5.614	-	dBm	reference antenna

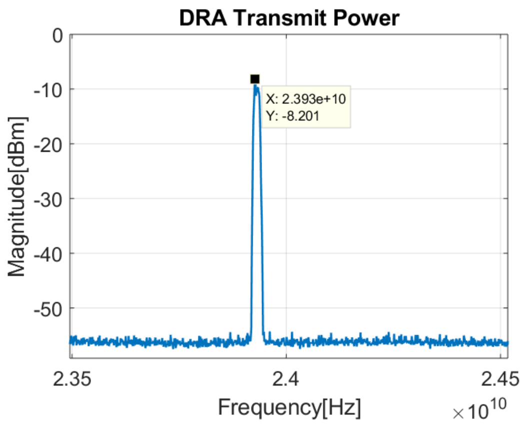

(a) DRA measured power

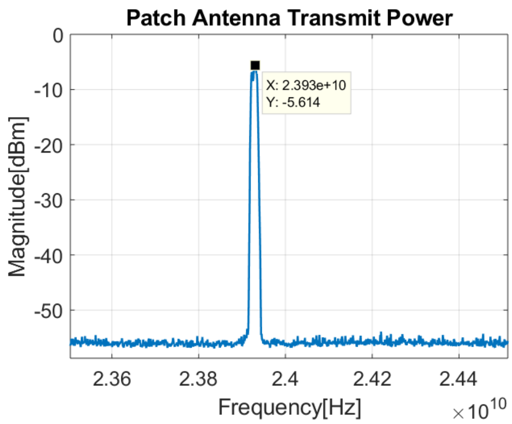

(b) Patch antenna measured power

Figure 72: Measured power for DRA and patch antennas

6.2 Evaluation of the Radar System

The radar system consist of the radar transceiver board as shown in Figure 73 and the external phase locked loop as shown in Figure 74. A voltage limiter consisting of a simple resistor and Zener diode is used to limit the tuning voltage to 5 V max to avoid damaging the MTR via its tuning pins. Between the arduino and SPI pins on the MTR a resistive voltage divider is added to convert the 0-5 V output range of the arduino to the 0-3.3V range of the MTR board. The system phase noise is measured and the PLL locking characteristics are determined.

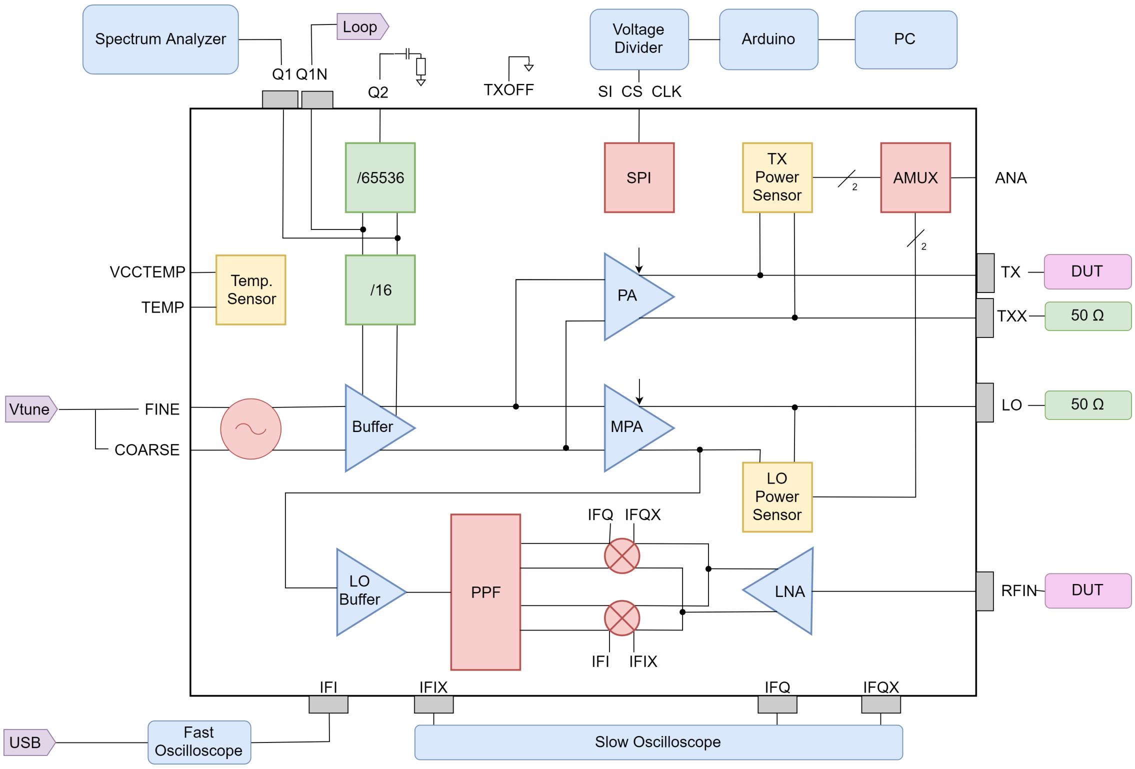

Figure 73: Measurement setup MTR part for FMCW validation, board scheme adapted from [7]

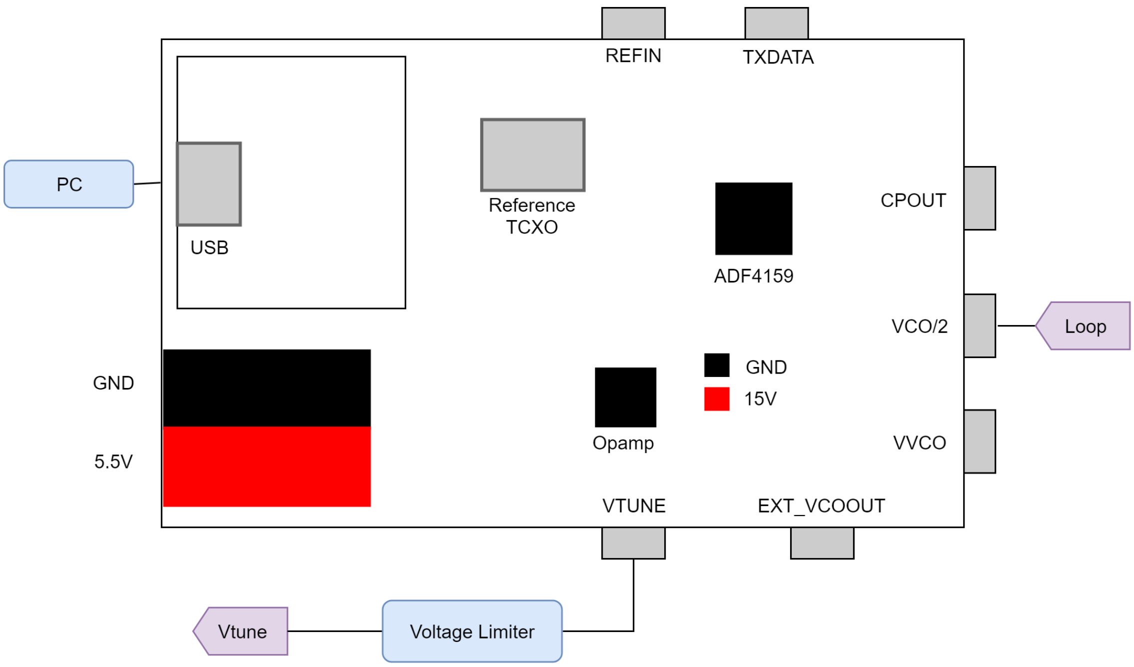

Figure 74: Measurement setup PLL part for FMCW validation, adapted from [9]

6.2.1 System Phase Noise

The total system phase noise can be obtained by measuring at the divided down Q1 or at LO with the PLL connected. According to the previous section, using a battery with display turned off decreases the added noise to the phase noise measurement. However, the battery can only be powered up to 5.4 V at max, which means the 15 volts needed for the opamp cannot be provided by the battery and should be connected to a voltage power supply which is more noisy. In addition, a Zener diode was used for the voltage limiter at the VTUNE output which typically has a high noise. Since this Zener diode is part of the PLL loop, the phase noise is expected to be suppressed by the loop filter.

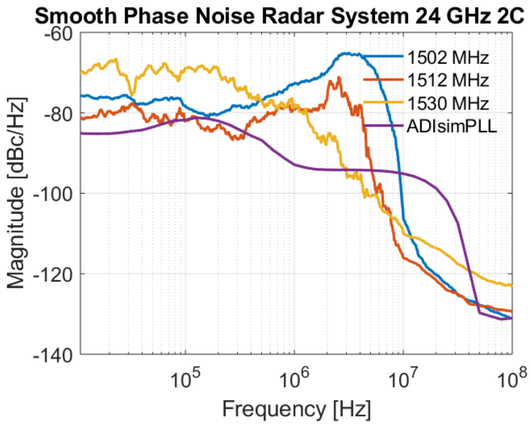

Figure 75: Phase noise total system at 24 GHz with 2C loop filter for different lock frequencies

The phase noise measurements were done for the passive loop filters, because the default active loop filter on the evaluation board failed to lock in and around the 24 GHz band. Because this filter was already implemented on the evaluation board, there was no possibility to check the transfer function of this filter. This active filter is therefore not further considered for the system and the passive filters were used. The phase noise measurements using different passive filters as shown in Figures 75 and 76 varied a lot during the measurements for the same measurement setup and PLL settings. The results are shown in Figures 75 and 76 together with the reference as computed by ADIsimPLL. Compared to the reference obtained in ADIsimPLL none of the measured phase noise has a similar shape and the overall phase noise level was measured do differ with maximum 10 dB from the simulated values. However, when compared to the phase noise which was measured with the MTR only, one could see that the system phase noise has dropped close in with at least 10 dB which confirms the PLL filtering the phase noise.

From the measured phase noise for different loop filters, the 4C loop filter resulted in a lowest overall phase noise. Therefore the 4C loop filter was further used for testing purposes of the system.

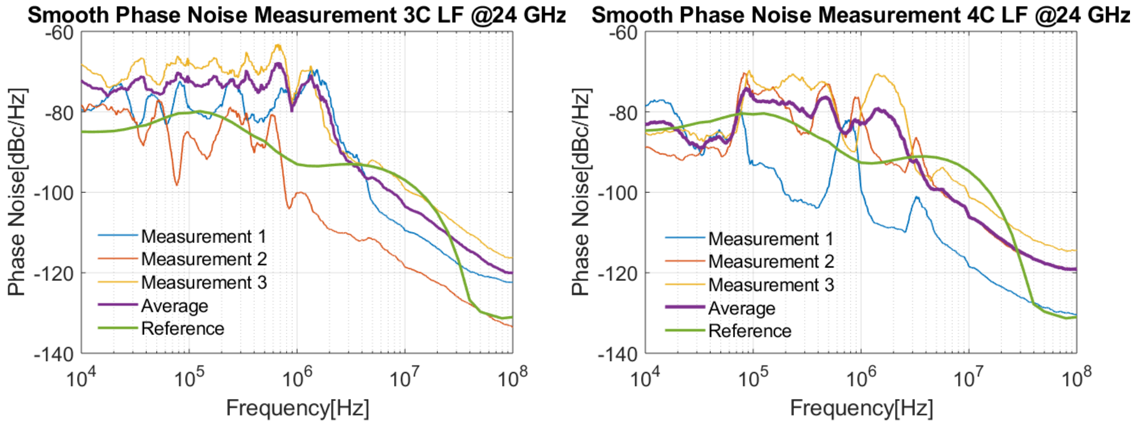

(a) Phase noise system with 3C loop filter **(b)** Phase noise system with 4C loop filter

Figure 76: Phase noise measured of the MTR and total system at 24 GHz with 3C and 4C loop filter with VCO frequency setting on 1550 MHz and 1525 MHz, respectively

6.2.2 PLL Test Methodology

The nodes of the loop filter for CP-PLLs in general, are considered to be a critical controlling node of the PLL. A correct operating loop filter is essential for the PLL to operate correctly over the specified frequency range. Therefore the PLL must be tested extensively. The important functional characteristics which are often tested for PLLs are: the lock time, system startup lock time, capture/lock range, phase/frequency step response time, overshoot, loop bandwidth and output jitter. The afore-mentioned characteristics are however all connected to a certain extend. To test the operation of the PLL the lock and capture range are considered and the linearity of frequency sweeps.

Lock and Capture Range

The first test of the PLL was performed by connecting the Vfine and Vcoarse together for Vtune, which is conrolled by the PLL board. The polarity of the phase frequency detector is set on positive, which was also set in the ADIsimPLL simulation program. By changing the VCO output frequency in the PLL Software (delivered with the PLL evaluation board), the lock frequency can be changed. The passive loop filters were all tested on lock and capture range and they all covered the 24 GHz ISM band.

To test the capture range as specified in the PLL program a triangular sweep was carried out while the network analyzer was set on max peak hold. The results for each loop filter was quite similar and therefore only the capture range of the 4C loop filter is included as shown in Figure 77a. The triangular sweep started at 24 GHz and moved up to 200 MHz within 100 ms per sweep. With this long sweep duration the shape of the locked VCO could be carefully checked. During these sweeps some slight deformation of the VCO peak was observed at some times, which is caused by loss of lock of the PLL. Figure 77a shows some slight under and overshoot on the defined 200 MHz sweep bandwidth which is caused by the broad peak of the VCO.

When the sweep time was decreased to 10 ms the capture range did not change as shown in Figure 77b. However, further decreasing the sweep time to 5 and 1 ms, the capture range became smaller. This is likely the PLL which cannot keep up with the fast sweep time. Therefore the minimum sweep time of the system was limited to 10 ms.

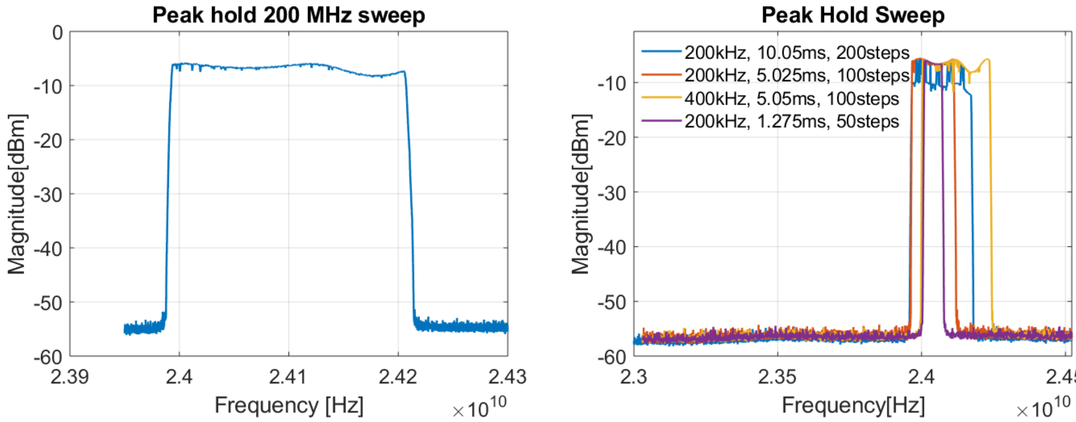

(a) Sweep time 100 ms **(b)** Different sweep time and frequency bandwidth

Figure 77: Frequency peak holds for triangular sweeps

Frequency Sweep Linearity

The frequency sweep linearity is obtained by using an oscilloscope to capture the divided down time domain signal at pin Q2. The waveforms were than imported into matlab for signal processing, resulting in a frequency-time plot as shown in Figure 78. The waveforms had a sweep period of 100 ms and should sweep from 22.89 - 23.08 kHz. Figure 78a shows the sawtooth waveform which ranged from 22.92 - 23.08 kHz which is close to the expected sweep range. Some overshoots can be seen for the sawtooth waveform when the frequency is changed from high to low. The overshoot to higher frequencies reaches 23.2 kHz, resulting in a VCO overshoot of 24.33 GHz which is outside the ISM band.

The triangular sweep is shown in Figure 78b which has less overshoots compared to the sawtooth waveform. Because the triangular sweep does not have to make instant frequency changes, the overshoot is indeed expected to be lower compared to the sawtooth one. About the frequency linearity one could see that the sweeps look quite linear. Because of the trade off between frequency resolution and time resolution for these plots, the frequency steps could not be much smaller than 100 Hz without making the time resolution worse. Therefore there are only a limited number of points available to check the frequency linearity.

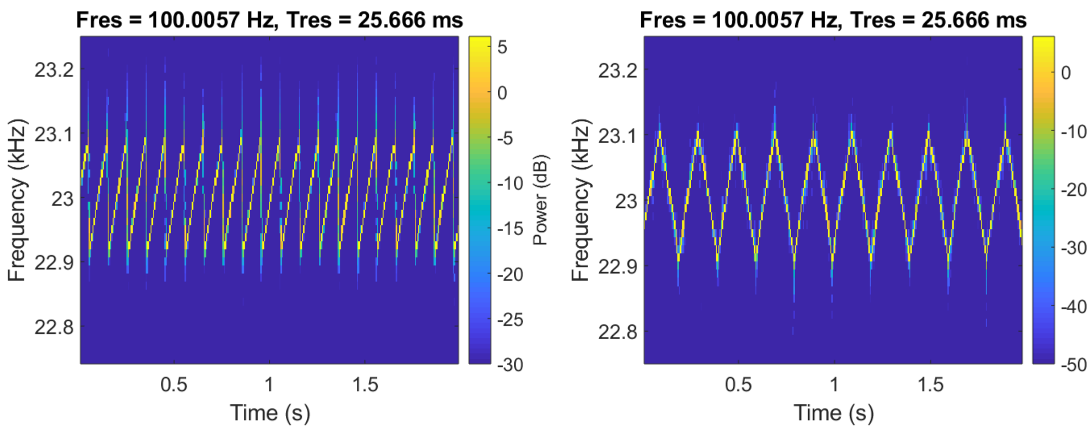

(a) Sawtooth **(b)** Triangular

Figure 78: Sawtooth and triangular frequency over time for a sweep period of 100 ms

The sweep bandwidth in Figure 78 are both slight off from the expected value. The minimum and maximum frequencies are at 22.91 kHz and 23.11 kHz resulting in a 24.023 GHz and 24.233 GHz VCO frequency, respectively. The maximum frequency therefore just exceeds the ISM band. To correct this the sweep bandwidth can be lowered in the software.

System Validation

With the MTR and PLL evaluation boards tested, a final system validation was considered. Because of the lower transmit power than expected from the MTR combined with a higher system phase noise and limited sweep time, a large corner reflector of 250 m^2 theoretical RCS was used for target detection. Considering the transmit power to be 1 dBm and a transmit and receive antenna gain of 7.5 dBi each, results in a received power of -60 dB. The MTR transceiver has a voltage conversion gain of 26 dB, resulting in a measured received voltage of 0.1557 V before it get mixed with the transmit signal. The beat frequency is expected to be at 26.67 Hz, assuming a sweep time of 10 ms and a target range of 20 cm.

An oscilloscope was used to read out the IQ signals and convert the time domain signal to the frequency spectrum. The resulting mixed signal however was of very small magnitude and the frequency spectrum did not show a peak at the expected beat frequency. Some possible explanations for this were:

- The close in phase noise of the carrier frequency is too high during frequency sweeps;
- The received power is lower than computed because of more losses which were not taken into account;
- The frequency sweep lost its linearity at a sweep time of 10 ms;
- The amplifier after the receiver in the MTR chip is not working properly;
- The transmit-receive leakage was too high.

By creating larger frequency sweeps and using longer cables for the transmit and receive antenna to reduce the leakage, the system could still not detect the target. Also by reducing the time sweep to shift the beat frequency to a higher value or placing the target further away did not result in any detection. The waveform sweep linearity could not be checked by using matlab processing because of the small frequency resolution of 100 Hz required and the small time resolution of at least 1 ms.

6.3 Conclusion

By measuring the MTR board, temperature changes around 10 degrees were observed by just turning the device on. Therefore the MTR always overshoots its center frequency and moves slowly back within the next few seconds. Slightly changing the chip temperature caused the frequency to shift up with tens of MH for the free running VCO.

The simulation of the PLL loop filter showed that the designed filters would work with the PLL, however by using the default (active) loop filter on the evaluation board no lock could be obtained. The passive filters however did obtain a frequency and phase lock. With the PLL waveform generator added and the protection circuitries, the phase noise varied a lot over different measurements. The most reasonable ones were shown during this report, however these do not align with the simulated phase noise. The simulated phase noise however does not take the additional circuitries into account which also add noise to the system phase noise. The PLL however did decrease the phase noise close in compared to the separate measured phase noise of the VCO.

The system clearly demonstrated to be sensitive to its loop filter, requiring a high phase margin ($> 70°$) for frequency lock. The loop bandwidth for both the passive and active filters were chosen to be above 200 kHz. However, the minimum sweep time in which the PLL could still keep its lock was at 10 ms which is higher than the sweep time that was used in the ADIsimPLL software.

The total radar system manage to generate sweeps after changing the default loop filter, but did not manage to show a beat frequency from the mixed signal outputs. Some possible causes were given, however due to limit time and equipment not all of these factors could be checked. The radiated power as stated in the datasheet were 6 dB higher than the actual measured values, resulting in lower receive power. Having a lower received power and more phase noise around the center frequency will likely cover static human targets at maximum distance in noise.

7 Conclusions and Discussion

Integrating a radar system in an enclosed light bulb is a challenging task. In this thesis, different types of optical transparent antennas were studied and combined with a physical radar system to access the feasibility for human presence detection.

To summarize, the following accomplishments and contributions to knowledge were found:

- The DRA is sensitive to its environment and is significantly influenced by the light bulb cap and backplate, causing blind spots for the radar in its field of view. Using polycarbonate as a microwave material might be low-cost and easy to fabricate, however its electric parameters are not well documented resulting in a slight impedance mismatch in the antennas.
- The radar model developed was too idealistic compared to the measurement environment and did not take the losses and noise of measurement equipment and electronics into account and could therefore not be compared to the final radar system which contained (noisy) circuitries.
- The use of phase locked loop implementation for FMCW radar system removes the temperature and sample dependence of the radar transceiver, but suffers when sweeps faster than 10 ms are required. The sweep time limits the beat frequency output and is likely to cover human targets in noise for the presence detection application. For an already relatively linear free running VCO in the frequency band of interest, a PLL does not add much value. For fast sweeps within the ISM band, the used VCO is likely to benefit more from a faster software controlled solution.

7.1 Recommendations

For further research on an optically transparent DRA in a bulb housing it should be taken into account that the DRA design should be fine-tuned in its final environment. During this thesis the influence of the housing was obtained by doing simulations. These large structures and round surfaces however require fine meshing, resulting in very long simulation times. It is thus recommended to do measurements on the radiation pattern with the antenna placed in the light bulb housing. By comparing this radiation pattern with the radiation pattern of a bare antenna, the radiation properties of the light bulb housing can be obtained. With such measurements the transmission properties of the cap could be obtained.

References

[1] J. Hautcoeur, L. Talbi, and K. Hettak, "Feasibility study of optically transparent cpw-fed monopole antenna at 60-ghz ism bands," *IEEE Transactions on Antennas and Propagation*, vol. 61, no. 4, pp. 1651–1657, April 2013.

[2] J. Hautcoeur, F. Colombel, X. Castel, M. Himdi, and E. M. Cruz, "Optically transparent monopole antenna with high radiation efficiency manufactured with silver grid layer (aggl)," *Electronics Letters*, vol. 45, no. 20, pp. 1014–1016, September 2009.

[3] S. Long, M. McAllister, and L. Shen, "The resonant cylindrical dielectric cavity antenna," *IEEE Transactions on Antennas and Propagation*, vol. 31, no. 3, pp. 406–412, May 1983.

[4] J. Fortuny-Guasch and J.-M. Chareau, "Radar cross section measurements of pedestrian dummies and humans in the 24/77 ghz frequency bands," European Commission, Publications Office of the European Union, Tech. Rep. 25762 EN, 2013.

[5] P. V. Brennan, Y. Huang, M. Ash, and K. Chetty, "Determination of sweep linearity requirements in fmcw radar systems based on simple voltage-controlled oscillator sources," *IEEE Transactions on Aerospace and Electronic Systems*, vol. 47, no. 3, pp. 1594–1604, July 2011.

[6] Y. Kobayashi and M. Katoh, "Microwave measurement of dielectric properties of low-loss materials by dielectric rod resonator method," *IEEE Transactions on Microwave Theory and Techniques*, vol. 33, no. 7, pp. 586–592, July 1985.

[7] Infineon, "User's guide to bgt24ltr11n16," Infineon Technologies AG, Tech. Rep., 2017, application Note AN472.

[8] A. Devices, "Direct modulation/fast waveform generating, 13 ghz, fractional-n frequency synthesizer," Analog Devices, Tech. Rep., 2013 - 2014, datasheet.

[9] ——, "Ev-adf4159eb1z/ev - adf4159eb3z user guide," Analog Devices, Tech. Rep., 2013 - 2014, datasheet.

[10] Infineon, "User's guide to bgt24mtr11," Infineon Technologies AG, Tech. Rep., 2012, application Note AN305.

[11] Y. Kobayashi and S. Tanaka, "Resonant modes of a dielectric rod resonator short-circuited at both ends by parallel conducting plates," *IEEE Transactions on Microwave Theory and Techniques*, vol. 28, no. 10, pp. 1077–1085, October 1980.

[12] R. K. Mongia and P. Bhartia, "Dielectric resonator antennas - a review and general design relations for resonant frequency and bandwidth," *International Journal of Microwave and Millimeter-Wave Computer-Aided Engineering*, vol. 4, no. 3, pp. 230–247, 1994.

[13] E. C. Committee, "The european table of frequency allocations and utilisations in the frequency range 9 khz to 3000 ghz," European Conference of Postal and Telecommunications Administrations, Tech. Rep., 2018.

[14] C. Barrett, "Fractional/integer-n pll basics," Texas Instruments, Tech. Rep., August 1999, technical Brief SWRA029.

[15] D. Fischette. (2009) First time, every time - practical tips for phase-locked loop design. [Online]. Available: http://www.delroy.com/PLL_dir/pll.htm

[16] V. Winkler, "Range doppler detection for automotive fmcw radars," in *2007 European Microwave Conference*, Oct 2007, pp. 1445–1448.

[17] Altair. (2018) Radar applications in everyday life. [Online]. Available: http://www.radartutorial.eu/01.basics/Minimal%20Measuring%20Range.en.html

[18] S. Pisa, E. Pittella, and E. Piuzzi, "A survey of radar systems for medical applications," *IEEE Aerospace and Electronic Systems Magazine*, vol. 31, no. 11, pp. 64–81, November 2016.

[19] J. R. Saberin and C. Furse, "Challenges with optically transparent patch antennas," *IEEE Antennas and Propagation Magazine*, vol. 54, no. 3, pp. 10–16, June 2012.

[20] K. W. Leung, Y. M. Pan, M. Yong, X. S. Fang, E. H. Lim, K. M. Lu, and H. P. Chan, "Dual-function radiating glass for antennas and light covers - part i: Omnidirectional glass dielectric resonator antennas," *IEEE Transactions on Antennas and Propagation*, vol. 61, no. 2, pp. 578–586, 2013.

[21] K. W. Leung, X. S. Fang, Y. M. Pan, E. H. Lim, K. M. Luk, and H. P. Chan, "Dual-function radiating glass for antennas and light covers - part ii: Dual-band glass dielectric resonator antennas," *IEEE Transactions on Antennas and Propagation*, vol. 61, no. 2, pp. 587–597, 2013.

[22] M. Simeoni, R. Cicchetti, A. Yarovoy, and D. Caratelli, "Plastic-based supershaped dielectric resonator antennas for wide-band applications," *IEEE Transactions on Antennas and Propagation*, vol. 59, no. 12, pp. 4820–4825, Dec 2011.

[23] M. Simeoni, R.Cicchetti, A. Yarovoy, and D. Caratelli, "Supershaped dielectric resonator antennas," *IEEE Antennas and Propagation Society International Symposium*, pp. 1–4, June 2009.

[24] E. Lim and K. Leung, "Transparent dielectric resonator antennas for optical applications," *IEEE transactions on antennas and propagation*, vol. 58, no. 4, pp. 1054–1059, 2010.

[25] L. Huitema and T. Monediere, *Dielectric Materials for Compact Dielectric Resonator Antenna Applications.* InTech, 2012.

[26] P. Lighting. (2018) Philips hue starterspakket e27 white ambiance. [Online]. Available: https://www.meerdanlicht.nl/philips-hue-starterspakket-e27-white-ambiance.html

[27] S. O. Piper, "Radar principles," Georgia Tech Research Institute, Tech. Rep., 2007, course notes: Principles of CW RADAR.

[28] G. W. Records. (2018) Tallest man - living. [Online]. Available: http://www.guinnessworldrecords.com/world-records/tallest-man-living

[29] F. Colombel, X. Castel, M. Himdi, G. Legeay, S. Vigneron, and E. M. Cruz, "Ultrathin metal layer, ito film and ito/cu/ito multilayer towards transparent antenna," *IET Science, Measurement Technology*, vol. 3, no. 3, pp. 229–234, May 2009.

[30] S. Long, M. McAllister, and L. Shen, "The resonant cylindrical dielectric cavity antenna," *IEEE Transactions on Antennas and Propagation*, vol. 31, no. 3, pp. 406–412, May 1983.

[31] K. Luk and K. Leung, *Dielectric Resonator Antennas.* Baldock, Hertfordshire, England: Research Studies Press Ltd., 2003.

[32] K. W. Leung, E. H. Lim, and X. S. Fang, "Dielectric resonator antennas: From the basic to the aesthetic," *Proceedings of the IEEE*, vol. 100, no. 7, pp. 2181–2193, July 2012.

[33] D. Kajfez, A. W. Glisson, and J. James, "Computed modal field distributions for isolated dielectric resonators," *IEEE Transactions on Microwave Theory and Techniques*, vol. 32, no. 12, pp. 1609–1616, Dec 1984.

[34] S. M. Shum and K. M. Luk, "Analysis of aperture coupled rectangular dielectric resonator antenna," *Electronics Letters*, vol. 30, no. 21, pp. 1726–1727, Oct 1994.

[35] E. A. Marcatili, "Dielectric rectangular waveguide and directional coupler for integrated optics," *Bell Labs Technical Journal*, vol. 48, no. 7, pp. 2071–2102, 1969.

[36] S. Keyrouz and D. Caratelli, “Dielectric resonator antennas: Basic concepts, design guidelines, and recent developments at millimeter-wave frequencies,” *International Journal of Antennas and Propagation*, vol. 2016, pp. 1–20, Sep 2016.

[37] X. S. Fang and K. W. Leung, “Designs of single-, dual-, wide-band rectangular dielectric resonator antennas,” *IEEE Transactions on Antennas and Propagation*, vol. 59, no. 6, pp. 2409–2414, June 2011.

[38] M. W. McAllister and S. A. Long, “Resonant hemispherical dielectric antenna,” *Electronics Letters*, vol. 20, no. 16, pp. 657–659, August 1984.

[39] Y. Song and A. Sebak, “Radiation pattern of aperture coupled prolate hemispheroidal dielectric resonator antenna,” *Progress In Electromagnetics Research*, vol. 58, no. 1, pp. 115–133, 2006.

[40] K. L. Wong, N. C. Chen, and H. T. Chen, “Analysis of a hemispherical dielectric resonator antenna with an airgap,” *IEEE Microwave and Guided Wave Letters*, vol. 3, no. 10, pp. 355–357, Oct 1993.

[41] M. I. Skolnik, *Introduction to Radar Systems*. McGraw-Hill Book Company, 1962.

[42] S. O. Piper, “Sensitivity in linear fmcw radar,” Georgia Tech Research Institute, Tech. Rep., 2007, course notes: Principles of CW RADAR.

[43] C. Wolff. (2018) Minimal measuring range. [Online]. Available: http://www.guinnessworldrecords.com/world-records/tallest-man-living

[44] *A continuous-wave (CW) radar for gait analysis*, Nov 2001.

[45] M.Otero, *Application of a continuous wave radar for human gait recognition*. SPIE, 2005.

[46] A. G. Stove, “Linear fmcw radar theory,” Philips Research Laboratories, Tech. Rep. 2500, August 1987.

[47] D. G. C. Luck, *Frequency modulated radar*. McGraw-Hill, 1949.

[48] M. A. W. Ismail, “A study of the double modulated fm radar,” Ph.D. dissertation, ETH Zurich, 1955.

[49] B. Horton, “Noise-modulated distance measuring systems,” *Proceedings of the IRE*, vol. 47, no. 5, pp. 821–828, 1959.

[50] W. Saunders, “Post-war developments in continuous-wave and frequency-modulated radar,” *IRE Transactions on Aerospace and Navigational Electronics*, vol. 8, no. 1, pp. 7–19, 1961.

[51] W. R. Fried, “An fm-cw radar for simultaneous three-dimensional velocity and altitude measurement,” *IEEE Transactions on Aerospace and Navigational Electronics*, vol. 11, no. 1, pp. 45–57, 1964.

[52] B. R. Mahafza and A. Elsherbeni, *MATLAB simulations for radar systems design*. CRC press, 2003.

[53] D. E. Barrick, “Fm/cw radar signals and digital processing,” National Oceanic and Atmospheric Administration, Tech. Rep. 26, July 1973.

[54] A. G. Stove, “94ghz fmcw radar,” Philips Research Laboratories, Tech. Rep. 3304, December 1987.

[55] ——, “a 3ghz fmcw radar with mti,” Philips Research Laboratories, Tech. Rep. 3284, March 1985.

[56] S. Rao, “Introduction to mmwave sensing: Fmcw radars module 1 : Range estimation,” Texas Instruments, Tech. Rep., 2017, tI training notes.

[57] S. O. Piper, “Fmcw radar receivers,” Georgia Tech Research Institute, Tech. Rep., 2007, course notes: Principles of CW RADAR.

[58] ——, “Frequency sweep linearity,” Georgia Tech Research Institute, Tech. Rep., 2007, course notes: Principles of CW RADAR.

[59] A. Devices, “Fundamentals of phase locked loops(plls),” Analog Devices, Tech. Rep., 2008, tutorial.

[60] H. Curtin and P. O’Brian, “Phase-locked loops for high-frequency receivers and transmitters - part 1,” *Analog Dialogue*, vol. 33, no. 3, pp. 1–4, 1999.

[61] ——, “Phase-locked loops for high-frequency receivers and transmitters - part 2,” *Analog Dialogue*, vol. 33, no. 5, pp. 1–5, 1999.

[62] ——, “Phase-locked loops for high-frequency receivers and transmitters - part 3,” *Analog Dialogue*, vol. 33, no. 7, pp. 1–5, 1999.

[63] B. Riddle, J. Baker-Jarvis, and J. Krupka, “Complex permittivity measurements of common plastics over variable temperatures,” *IEEE Transactions on Microwave Theory and Techniques*, vol. 51, no. 3, pp. 727–733, 2003.

[64] A. Kilian, J. Weinzierl, and L. P. Schmidt, “Permittivity measurement techniques at 24 ghz for automotive polymer composites including thin films and paint foils,” Institute for Microwave Technology, Tech. Rep., 2008, paper.

[65] Thorlabs. (2018) Dichroic atomic vapor spectroscopy kit. [Online]. Available: https://www.thorlabs.com/newgrouppage9.cfm?objectgroup_id=5393

[66] Prospector. (2018) Acrylic typical properties generic acrylic (pmma). [Online]. Available: https://plastics.ulprospector.com/generics/3/c/t/acrylic-properties-processing

[67] C.-L. Plastics. (2018) Rexolite specifications. [Online]. Available: http://www.rexolite.com/specifications/

[68] J. Wallace. (2014) Corning introduces gorilla glass 4, next generation of chemically strengthened glass for displays, devices. [Online]. Available: https://www.laserfocusworld.com/articles/2014/11/corning-introduces-gorilla-glass-4-next-generation-of-chemically-strengthened-glass-for-displays-devices.html

[69] C. Plastics. (2018) Acrylic vs polycarbonate. [Online]. Available: http://cambrianplastics.co.nz/product/acrylic-vs-polycarbonate/

[70] S. Microwave, “Optimizing test boards for 50 ghz end launch connectors: Grounded coplanar launches and through lines on 30 mil rogers 4350 with comparison to microstrip,” Southwest Microwave, Inc, Tech. Rep., 2007, techreport.

[71] D. Kajfez and P. Guillon, *Dielectric resonators*, February 1998.

[72] E. Ito and Y. Kobayashi, “Changes in physical properties of polycarbonate by absorbed water,” *Journal of Applied Polymer Science*, vol. 22, no. 4, pp. 1143–1149.

[73] Infineon, “Bgt24ltr11n16 silicon germanium 24ghz radar transceiver mmic,” Infineon Technologies AG, Tech. Rep., 2017, datasheet.

[74] ——, “Bbgt24mtr11 silicon germanium 24 ghz transceiver mmic,” Infineon Technologies AG, Tech. Rep., 2014, datasheet.

[75] K. Ramasubramanian, K. Ramaiah, and A. Aginskiy, “Moving from legacy 24 ghz to state-of-the-art 77 ghz radar,” Texas Instruments, Tech. Rep., October 2017.

[76] F. J. Harris, "On the use of windows for harmonic analysis with the discrete fourier transform," *Proceedings of the IEEE*, vol. 66, no. 1, pp. 51–83, 1978.

[77] M. Lohne, "The computational complexity of the fast fourier transform," University of Oslo, Tech. Rep. 1, March 2017.

[78] R. L. R., S. R. W., and R. C. M., "The chirp z-transform algorithm and its application," *Bell System Technical Journal*, vol. 48, no. 5, pp. 1249–1292, 1968.

[79] B. Wadell, *Transmission Line Design Handbook*, ser. Artec House Antennas and Propagation Library. Artech House, 1991.

[80] M. Truong, "Antenna topology comparison and design for motion sensor integration in hue white and color," Philips Lighting and Delft University of Technology, High Tech Campus 7, Eindhoven, Tech. Rep. 1, December 2017.

A Frequency Bands

Regarding available frequency bands one could consider the licensed and unlicensed bands. The licensed frequency bands overall are costly and can vary per country and region.

Considering the ISM radio bands there are common frequency bands [13] which are used for radiowave sensing systems. The ISM bands are globally available and of free usage when the designed radar system does not exceed the limit for protection of radars in adjacent band as stated by the Electronic Communications Committee (ECC) [13]. The frequency bands that are relevant to radars (as short range devices) are considered and are given in Table 18.

Table 18: Typical frequency bands for radio-wave sensing systems as stated by the Electronic Communications Committee (ECC) [13]

Band	Center Frequency [GHz]	Bandwidth [MHz]	λ[cm]	type
C	5.8	100	5.2	ISM
K	24.125	250	1.2	ISM
V	61.25	500	0.49	ISM
W	76.5	1000	0.39	Automotive
W	80	2000	0.38	Automotive
G/mm	122.5	1000	0.24	ISM
G/mm	245	2000	0.12	SRD

Automotive first made products on the 24.125 GHz band, however the need for smaller components shifted the interest to 76-77 GHz [75]. The 76 - 77 GHz frequency band is reserved for automotive due to the benefit of high allowed equivalent isotropic radiated power which is needed for long-range radar applications [75] and is often used in Adaptive Cruise Control (ACC). The other automotive radar frequency band ranges from 79-81 GHz which is mainly used for short range radar systems. Both frequency bands mentioned above are limited to automotive only and therefore it is not an option for the radar implementation in the light bulb.

The higher ISM frequency band of 122.5 GHz or the short range device (SRD) band at 245 GHz could be used if smaller components and more accuracy (due to shorter wavelengths) are desired. However, a higher frequency requires a relatively high power consumption compared to lower frequency radars. Also the radar transceiver should be able to cope with the high frequency since factors such as weather influence will be more significant on higher frequencies. In addition the materials used for the chip design should be low in losses since these are likely to be very significant on higher frequencies compared to the same material on lower frequencies. Moreover, small fabrication errors in the applied antennas will result in a faulty radar. The overall system sensitivity need increases the cost of such radar systems which make it not yet applicable in commercial products.

With the two outer bands unsuitable for this application only the 5.8 GHz, 24.125 and 61.25 GHz bands are left with a quarter wavelength of 1.3 cm, 0.3 cm and 0.1225 cm, respectively. Due to the aluminium housing of the bulb which blocks all radiation outwards, the antenna is likely to be present in the cap which has a height around 3 cm. Assuming an antenna with lengths of multiple $\frac{\lambda}{4}$ the 24.125 GHz and 61.25 GHz bands are more likely to be small enough not to block visible light. As mentioned before a higher frequency also brings a higher power consumption and therefore the 24.125 GHz ISM frequency band seem to be most suitable for the application for indoor lighting.

B Digital Signal Processing

The Fourier transform is a widely used in radar for obtaining the target information from the received data in a radar system. For embedded radar systems as mentioned before, the computing power and memory is limited, therefore two different methods of computing the Fourier transform are considered in this section. First the most used method of doing the Fourier transform is briefly explained and afterwards a less computationally intensive method is introduced.

B.1 Discrete Fourier Transform

The DFT is widely used due to its simplicity and can be used for analyzing a signal or for computation of fast convolution in a digital filter for example. The equation which represents the DFT is shown in Equation (73) [76] where F[n] is the DFT of the sequence of f[k] and N the number of sample points. The exponent in Equation (73) is also called the twiddle factor that divides an unit circle into N equal samples and is defined as W_N^{nk}.

$$F[n] = \sum_{k=0}^{N-1} f[k] e^{-j\frac{2\pi}{N}nk} \quad for \quad n = 0 : N-1 \tag{73}$$

The number of operations needed (complexity $\mathcal{O}$) for a DFT are $\mathcal{O}(N^2)$ [77] becomes huge for a large number of samples. Many different algorithms which share a common name of FFT have been proposed to use the DFT efficiently. The FFT computation is based on decomposing the DFT and form a butterfly network which makes it possible to compute the FFT in parallel. The complexity for the FFT is $\mathcal{O}(Nlog_2(N))$ [77] which can be large for thousands of data samples which is not very unlikely for received radar data. Therefore, DFT might be quick and straightforward to apply, however when applied in a microprocessor memory and computation power limitations are likely to occur.

B.2 Chirp *z*-Transform

To cope with the microprocessor limitations a more efficient way to compute the Fourier transform is named the Chirp *z*-Transform (CZT) [78] and can be considered as a generalized DFT. The CZT uses the z-transform and is not limited to samples equally spaced and on the unit circle in the z-plane like the DFT. For the CZT the angular spacing of the points in z-plane is constant, however the radii can vary over a circular or spiral contour. The z-transform can be obtained using Equation (74) where N is the number of samples.

$$X(z_k) = \sum_{n=0}^{N-1} x_n z_k^{-n} \tag{74}$$

With z_k consisting of a set of points equally spaced around the unit circle, Equation (74) transforms to the DFT. For a more general contour, one could define the z_k as

$$z_k = AW^{-}k \quad k = 0, 1, \cdots, M-1 \tag{75}$$

where A and W are complex numbers as defined in Equation (76) and Equation (77), respectively, and M is an integer.

$$A = A_0 e^{j2\pi\theta_0} \tag{76}$$

$$W = W_0 e^{j2\pi\phi_0} \tag{77}$$

For A=1, M=N and $W = e^{\frac{-j2\pi}{N}}$ the above equations correspond to a DFT. For the CZT the z-plane contour starts at an arbitrary value z=A and depending on the value of W it will spiral in or out the origin. Setting W_0 equal to 1 results in Equation (77) being just a complex sinusoid with linear increasing frequency, which is comparable to the waveform chirps. The complexity of the CZT is roughly proportional to $\mathcal{O}(N+M)log_2(N+M)$ which seems to be larger than the FFT complexity, however, since the CZT does not have to be equally spaced the number of samples overall needed for a similar Fourier transform resolution is smaller. Additional advantages of the CZT include:

1. the number of time samples do not have to match the number of samples for the CZT;
2. the angular spacing for z_k is arbitrary;
3. the flexibility in design is larger compared to the FFT since z_k does not have to follow a unit circle.

The disadvantage of CZT is the computation time, which is proportional to $L \cdot log_2(L)$ [78] where L is greater than N or M.

C Radar Transceiver BGT24LTR11N16

The radar transceiver considered for this thesis which is made by Infineon is designed for CW radar, however Phase Shift Keying (PSK) is also possible and even FMCW might be even possible when an external circuitry is used. One drawback of this radar transceiver is the Tx,Rx antenna connection isolation which equals 30 dB. For FMCW a Tx,Rx isolation around 50 dB would be more preferable. Infineon made the board such that for CW no external PLL is needed since the chip itself can keep the frequency within the 24 GHz ISM band.

Table 19: Specification of Infineon K-band BGT24LTR11N16 Doppler radar

Parameter	Specifications	Note
Operating frequency range	24-24.25 GHz	-
Center frequency	24.125 GHz	-
Supply voltage	3.3 V	-
Ambient temperature range	-40 C to 85 C	-
Typical TX load impedance	50 Ω	single ended
Typical TX output power	6 dBm	-
Noise Figure SSB	12 dB	-
Tx,Rx isolation	30 dB	measured on evaluation board

In order to have other waveforms in this transceiver the VCO voltage can be controlled by using an external Phased Locked Loop (PLL) or a software based open loop. To get a FMCW signal with a typical sweep time of 0.1 ms, the option of a phased locked loop is likely to be too slow since it needs some recovery time to stabilize on a certain frequency. Therefore a software-based open-loop concept could be considered to make the transceiver operating as FMCW radar. The suggested model as obtained from the user's guide [10] is shown in Figure 79 where a MCU is used for the frequency control of the VCO. Withing the MCU a Look Up Table can be used which depends on temperature and the tuning voltage which can than be used to generate the desired frequency.

However this setup seems to very promising for the FMCW radar implementation and with a Tx,Rx isolation is around 25 - 30 dB, the chip itself is not very well suitable for FMCW waveforms. First of all, the chip housing is quite small which suffers from 'cross talk' between those connections and the receiver circuitry. This cross talk is not included in the isolation from transmit to receive and will degrade the isolation between the chip to the received signal. Also the IQ signal phase imbalance is relatively large with a maximum value of 24 degree as given in the data sheet [73]. Since methods like fast chirp waveforms FMCW rely on the phase difference between different chirps for the precise velocity and range information phase errors of 24 degrees will have a significant impact on the detection accuracy. Therefore this radar transceiver is not very suitable for the FMCW application and another chipset from Infineon is considered for the proposed radar model setup.

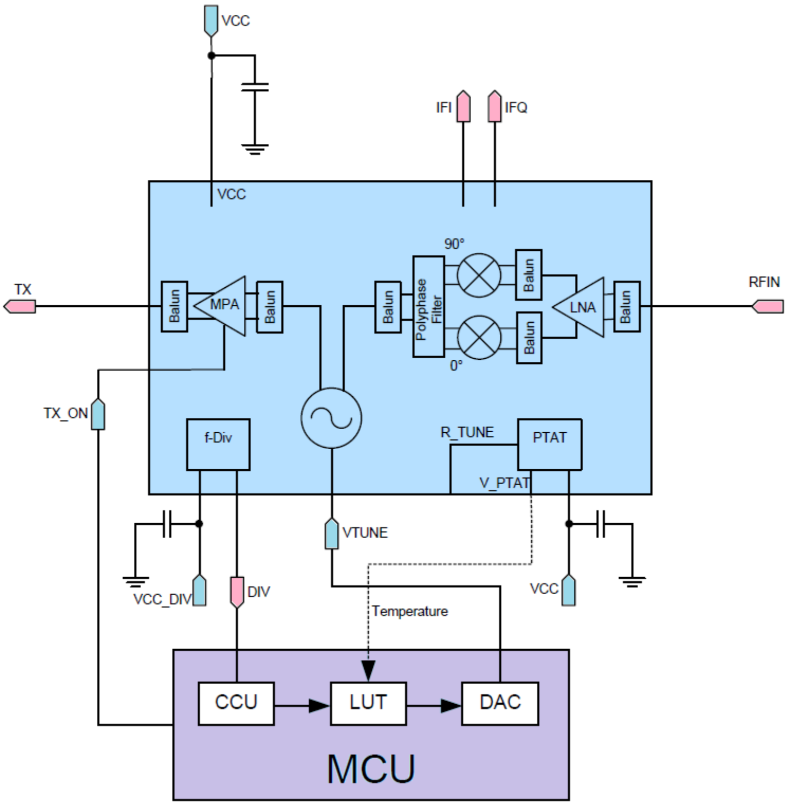

Figure 79: BGT24LTR11N16 Software-Based Open Loop for VCO frequency control as obtained from [10]

D Microstrip Formulae

The theoretical formulae which were used for the initial microstrip width computation are listed below. For a width-height ratio smaller than one, the impedance can be obtained by

$$Z_0 = \frac{60}{\sqrt{\epsilon_{eff}}} ln\Big(8\frac{H}{W} + 0.25\frac{H}{W}\Big) \tag{78}$$

where ϵ_{eff} is the effective dielectric permittivity and is computed as follows:

$$\epsilon_{eff} = \frac{\epsilon_r + 1}{2} + \frac{\epsilon_r - 1}{2}\Big[\frac{1}{\sqrt{1+12\frac{H}{W}}} + 0.04\Big(1 - \frac{H}{W}\Big)^2\Big] \tag{79}$$

For a W/H ratio larger than one the formulae that are used are:

$$Z_0 = \frac{120\pi}{\sqrt{\epsilon_{eff}}\Big[\frac{H}{W} + 1.393 + \frac{2}{3}ln(\frac{H}{W} + 1.444)\Big]} \tag{80}$$

$$\epsilon_{eff} = \frac{\epsilon_r - 1}{2} + \frac{\epsilon_r - 1}{2\sqrt{1+12\frac{H}{W}}} \tag{81}$$

E Grounded Coplanar Waveguide Formulae

$$Z_0 = \frac{60\pi}{\sqrt{\epsilon_{eff}}} \frac{1}{\frac{K(k)}{K(k')} + \frac{K(kl)}{K(kl')}} \tag{82}$$

$$k = \frac{w_{strip}}{b} \tag{83}$$

In the above equation the parameter b consist of the sum of the track width w_{strip} plus the gap widths on either side.

$$b = w_{strip} + 2d_g \tag{84}$$

$$k' = \sqrt{1-k^2} \tag{85}$$

$$kl' = \sqrt{1-kl^2} \tag{86}$$

$$kl = \frac{tanh(\frac{\pi w_{strip}}{4d_s})}{tanh(\frac{\pi b}{4d_s})} \tag{87}$$

$$\epsilon_{eff} = \frac{1+\epsilon_r \frac{K(k')}{K(k)} \frac{K(kl)}{K(kl')}}{1+\frac{K(k')}{K(k)} \frac{K(kl)}{K(kl')}} \tag{88}$$

The above stated equations for the grounded coplanar waveguide are all obtained from Transmission Line Design Handbook [79]. The parameter K(k) as used in the above formulae can be found by equations based on elliptical integrals of the first kind.

F EV-ADF4159EB3Z

A silk screen of the evaluation board is given in Figure 80 [9] where the different colors give the diagram functioning areas:

- blue: the micro-controller CY7C68013-CSP is included in this part with a USB connection for i.a. waveform control via computer.
- green: ADF4159 chip with TCXO of 100 MHz.
- red/pink: feed network including many voltage regulators on the Uxx places.
- yellow: internal VCO for the 1Z series and the loop filter given in light pink.
- grey: SMA connectors.
- light purple: pin connectors.
- dark purple: hole connectors.

For the 3Z version the VCO is not present.

The limitations on the divider values as given in the datasheet [8] are:

- $23 \leq INT \leq 4095$
- $0 \leq FRAC \leq 2^{25} - 1$
- $1 \leq Rcounter \leq 32$

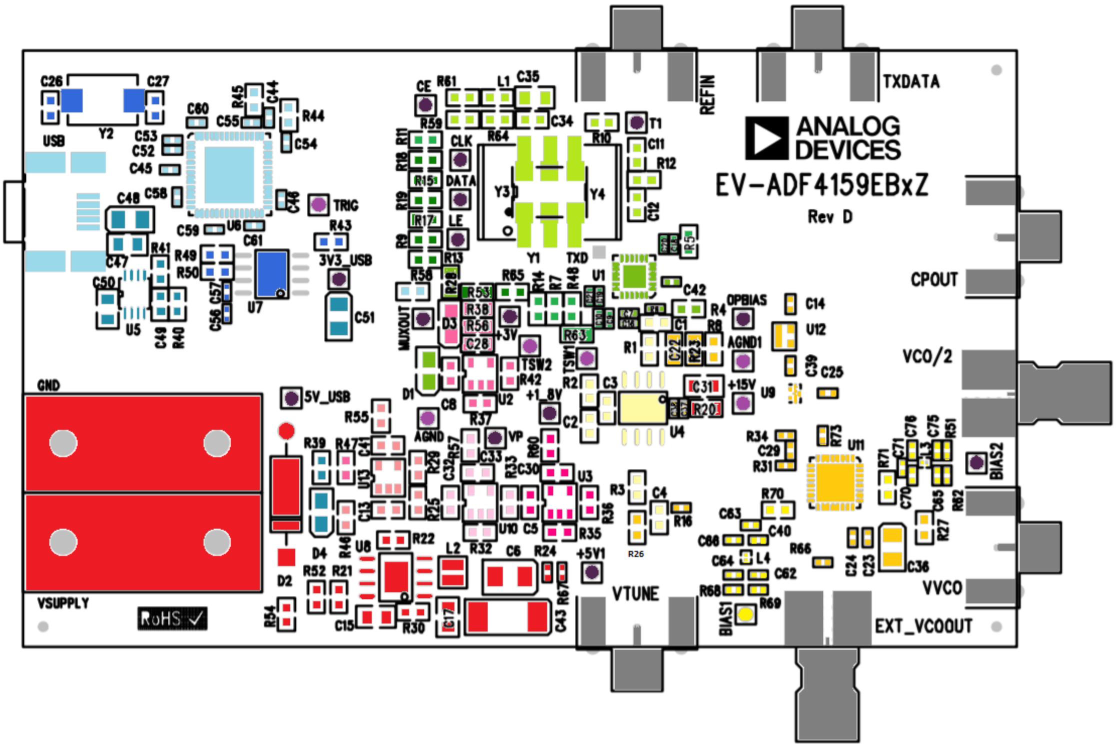

Figure 80: EVAL ADF4159EBxZ silk screen as obtained from [9]

The divider ratios of the RF synthesizer can be obtained by using predefined formulae. Since the MTR11 frequency divides the output signal of 24 GHz - 24.25 GHz by 16, the frequency range of the output signal from the PLL model should be within 1.5 GHz and 1.5156 GHz. The input reference frequency (REFin) is generated by the on board TCXO which operates on 100 MHz. The frequency step resolution of the PLL can be computed with

$$\Delta f = \frac{REF_{in}}{2^{25}} \tag{89}$$

where the factor 2^{25} equals the modulus value as shown in Figure 54 in the $\sum - \Delta$ fractional interpolator. The PFD bandwidth defined as f_{PFD} is defined as

$$f_{PFD} = REF_{in}\left(\frac{1+D}{R(1+T)}\right) \tag{90}$$

where D is RF REF_{in} doubler bit, R the RF reference division factor and T the reference divide-by-2 bit. The output frequency of the PLL can be written as

$$RF_{out} = N \cdot f_{PFD} \tag{91}$$

and using Equation (72) and Equation (90) one could rewrite the equation to obtain the division factor:

$$INT + \frac{FRAC}{2^{25}} = \frac{RF_{out}}{REF_{in}} \frac{R(1+T)}{1+D} \tag{92}$$

Computing $\frac{RF_{out}}{REF_{in}}$ for the given values give a factor between 15-15.156. To stay within the datasheet limites the INT value should at least be 23. Therefore a factor of at least 1.5333 is needed for the second term on the right of Equation (92). Since T,D can only be 0 or 1, the limits are met when R = 0, T = 1 and D = 0.

G Dielectric Permittivity Mode Chart

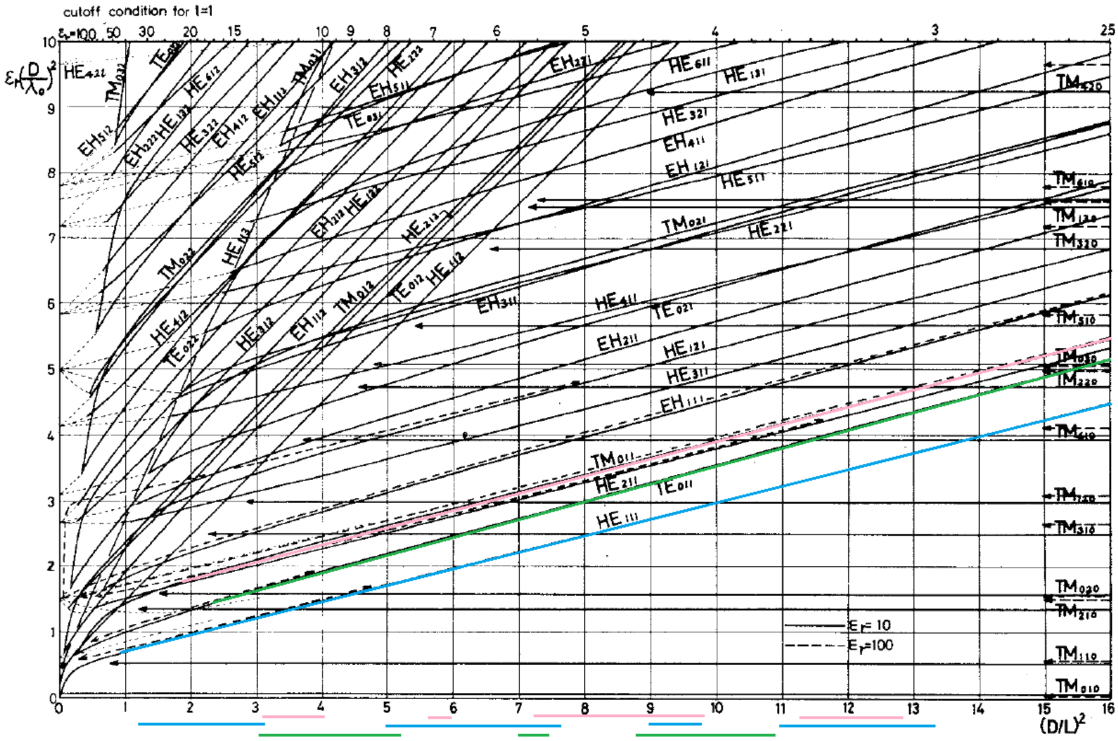

Figure 81: Dielectric rod mode chart with pink for TM011, blue for HE111 and green for TE011, obtained from [11]

G.1 Theoretical Rod Dimensions

Table 20: Theoretical resonant frequency obtained with ϵ_r = 2.712, Radius = 5.7 mm, Diameter = 11.4 mm, Length = 5 mm

Mode	freq [GHz]	mode	delta+lmode	lmode
TE01	24.108	qTE	1	0
TE02	35.379	qTE	1	0
HEM12	28.726	qTE	1	0
HEM14	41.644	qTE	1	0
HEM22	33.519	qTE	1	0
HEM32	38.528	qTE	1	0
TE01	40.283	qTE	1.999	1
TE02	48.455	qTE	1.999	1
TM01	26.757	qTM	1.016	1
TM02	40.236	qTM	1.052	1
HEM11	21.503	qTM	1.005	1
HEM12	43.483	qTE	1.999	1
HEM13	33.086	qTM	1.032	1
HEM21	26.099	qTM	1.015	1
HEM22	47.014	qTE	1.999	1
HEM23	39.666	qTM	1.051	1
HEM31	31.336	qTM	1.027	1
HEM41	36.878	qTM	1.042	1
TM01	41.485	qTM	2.008	2
HEM11	38.268	qTM	2.002	2
HEM13	45.783	qTM	2.016	2
HEM21	41.025	qTM	2.007	2
HEM31	44.467	qTM	2.013	2
HEM41	48.422	qTM	2.021	2

Table 21: Theoretical resonant frequency obtained with $\epsilon_r = 2.712$, Radius = 5.7 mm, Diameter = 11.4 mm, Length = 10 mm

Mode	freq [GHz]	mode	delta+lmode	lmode
TE012	24.111	qTE	2	1
TE03	45.138	qTE	1	0
HEM12	22.67	qTE	1	0
HEM22	28.379	qTE	1	0
TE01	24.111	qTE	2	1
TE02	35.381	qTE	2	1
TE03	49.04	qTE	2	1
TM01	21.294	qTM	1.031	1
TM02	36.354	qTM	1.098	1
HEM11	14.419	qTM	1.011	1
HEM12	28.729	qTE	2	1
HEM13	28.735	qTM	1.061	1
HEM14	41.646	qTE	2	1
HEM21	20.812	qTM	1.03	1
HEM22	33.522	qTE	2	1
HEM32	38.53	qTE	2	1
TE01	32.002	qTE	2.999	2
TE02	41.525	qTE	2.999	2
TM01	26.657	qTM	2.016	2
TM02	40.003	qTM	2.054	2
HEM11	21.462	qTM	2.005	2
HEM12	35.8	qTE	2.999	2
HEM13	32.924	qTM	2.032	2
HEM14	47.095	qTE	2.999	2
HEM21	26.006	qTM	2.015	2
HEM22	39.895	qTE	2.999	2
HEM23	39.453	qTM	2.052	2
HEM31	31.198	qTM	2.027	2
HEM32	44.281	qTE	2.999	2
HEM41	36.697	qTM	2.043	2
TE01	40.289	qTE	3.999	3
TE02	48.461	qTE	3.999	3
TM01	33.581	qTM	3.011	3
TM02	44.993	qTM	3.036	3
HEM11	29.654	qTM	3.003	3
HEM12	43.49	qTE	3.999	3
HEM13	38.759	qTM	3.021	3
HEM21	33.072	qTM	3.01	3
HEM22	47.02	qTE	3.999	3
HEM23	44.388	qTM	3.035	3
HEM31	37.222	qTM	3.018	3
HEM41	41.849	qTM	3.029	3

Table 22: Theoretical resonant frequency obtained with $\epsilon_r = 2.712$, Radius = 5.7 mm, Diameter = 11.4 mm, Length = 20 mm

Mode	freq [GHz]	delta+lmode	lmode
TE01	13.934	1	0
TE03	32.787	1	0
TE04	42.675	1	0
HEM12	20.326	1	0
TE01	16.937	2	1
TE03	45.139	2	1
TM01	18.94V 1.056	1	
TM02	31.219	1.145	1
HEM11	12.082	1.022	1
HEM12	22.67	2	1
HEM22	28.379	2	1
TE01	20.404	3	2
TE02	32.709	3	2
TE03	47.075	3	2
TM01	21.226	2.032	2
TM02	36.128	2.102	2
HEM11	14.388	2.011	2
HEM12	25.543	3	2
HEM13	28.64	2.063	2
HEM14	39.314	3	2
HEM21	20.757	2.03	2
HEM22	30.745	3	2
HEM32	36.088	3	2
TE01	24.113	4	3
TE02	35.382	4	3
TE03	49.041	4	3
TM01	23.658	3.022	3
TM02	37.903	3.071	3
HEM11	17.673	3.007	3
HEM12	28.73	4	3
HEM13	30.488	3.043	3
HEM14	41.647	4	3
HEM21	23.02	3.02	3
HEM22	33.523	4	3
HEM31	28.812	3.037	3
HEM32	38.531	4	3
HEM41	34.689	3.058	3

Table 23: Theoretical resonant frequency obtained with $\epsilon_r = 2.712$, Radius = 5.7 mm, Diameter = 11.4 mm, Length = 25 mm

Mode	freq [GHz]	delta+lmode	lmode
TE01	13.379	0	1
TE04	42.004	0	1
TE01	15.711	1	2
TE03	42.987	1	2
TE04	45.385	1	2
HEM11	11.785	1	1.027
HEM12	21.703	1	2
TE01	18.303	2	3
TE03	45.992	2	3
TE04	61.206	2	3
TM01	20.347	2	2.039
TM02	35.258	2	2.123
HEM11	13.308	2	2.013
HEM12	23.75	2	3
HEM14	38.121	2	3
HEM21	20.105	2	2.038
HEM22	29.239	2	3
HEM32	34.849	2	3
TE01	21.133	3	4
TE02	33.215	3	4
TE03	47.435	3	4
TE04	62.381	3	4
TM01	22.13	3	3.027
TM02	36.808	3	3.088
HEM11	15.614	3	3.009
HEM12	26.145	3	4
HEM13	29.286	3	3.053
HEM14	39.758	3	4
HEM21	21.547	3	3.025
HEM22	31.298	3	4
HEM32	36.549	3	4
TE01	24.113	4	5
TE02	35.382	4	5
TE03	49.041	4	5
TE04	63.677	4	5
TM01	24.201	4	4.02
TM02	38.237	4	4.068
HEM11	18.393	4	4.007
HEM12	28.73	4	5
HEM13	30.91	4	4.04
HEM14	41.647	4	5
HEM21	23.553	4	4.019
HEM22	33.523	4	5
HEM23	37.788	4	4.066
HEM31	29.22	4	4.035
HEM32	38.532	4	5
HEM41	35.016	4	4.055
TE01	27.206	5	6
HEM12	31.47	5	6
HEM31	31.114	5	5.028

H Measurements

H.1 MTR evaluation board connection

What has to be checked on the MTR evaluation board:

1. Pin 15 & 16 (test pins) have to be connected

Setup of MTR board:

1. Make sure the DC elements (capacitor + resistor) between the Q2 and GND pin are connected
2. 50Ω terminate TX, TXX, LO, RFIN
3. DC block IFI, IFIX, IFQ, IFQX with scope connections, set on a high ohmic load (1MΩ) and AC coupling
4. DC block and the Q1, Q1N connectors and connect one of them to a high speed (>1.5126 GHz) scope and terminate the other with 50Ω
5. Connect the arduino SPI output through a voltage divider (5 V - 3.3 V) with GND, SCK, CS and SI pins of the MTR board
6. Pin 26 (TXOFF, output ANA2) should be grounded if an SPI is used for enabling output power
7. Connect a power supply to Vcoarse and/or to Vfine with 0.5 - 5 V (5V max) with a current limitation of 0.11 mA (smallest setting is 1 mA for our power supply)
8. Connect a power supply to Vcc with 3.3 V (max 3.465 V) with a current limitation of 190 mA
9. Connect a power supply to Vcctemp with 3.3 V (max 3.465 V) with a current limit of of 3 mA
10. The voltage on the tuning voltage pins (Vcoarse & Vfine) should be larger than 0.5 V at any time for the VCO to function

H.2 PLL evaluation board setup

Setup of PLL board:

1. Connect 15 V from a voltage supply with 25 mA current limitation to the +15V and GND pins next to the opamp OP27
2. Connect the battery to the PLL voltage supply with 5.5V
3. connect Vtune with a SMA coax cable with an SMA to BNC converter with screws and to a clip for the Vtune pin
4. connect the mini USB cable to the PLL board and to a computer
5. Connect the Q1 or Q1N output of the MTR board to the VCO/2 on the PLL board
6. Set reference frequency to 100 MHz and set the Ref/2 on (PFD frequency should be 50 MHz).
7. Set charge pump current to 2.5 mA
8. Set the phase detector polarity to inverting active loop filter configuration
9. define the muxout output in the PLL software

10. if VCO/2 is used, program PLL for half the PFD frequency
11. connect VCO/2 to Q1 or Q1N of the MTR board
12. set waveform parameters as simulated by ADIsimPLL

Remarks on the PLL evaluation board:

1. One of the differential TX or TXX pins have to be terminated by 50 Ω which will reduce the output power by 3 dB (balun on 24 GHz is not that straightforward to make/obtain), the maximum output power is then 7.2 dBm
2. The IFI and IFQ signals have an impedance of 800 Ω and might be connected directly to an ohmic load greater then 10 kΩ. For smaller loads a coupling capacitor is needed (typical 2.3±0.2 DC voltage)
3. AC swing is max 0.6 V pk-pk (up to 1 V pk-pk when deeply in saturation)
4. TX and LO sensor are voltage peak detectors, and Vref (ANA1) can be used to eliminate temperature and supply voltage variations, the compensated detector output can be obtained by subtracting the Vref signal from the measured output power sensor

I Prototype V1.0

The first prototype was fabricated by Eurocircuits where PCB consisted of a Rogers 4350B material of 0.508 mm thickness was used and plated with 0.35μm copper traces. A layered structure view is of the prototype model simulated in CST is shown in Figure 42. The entire process of selecting the type of antenna and obtaining the CST models is further described in the internship report [80].

The measurements were done in an anechoic chamber at TU Delft with support of the Microwave Sensing, Signals & Systems group.

There were 6 versions in total of the prototype which were fabricated in a similar way and the connectors were soldered with different techniques as shown in Table 24. To the PCB prototype the holes of the connector had to be enlarged which is defined by the column 'Holes' and the end of the grounded coplanar waveguide had to be shorten (given by column 'Shorten') in order to make it fit the connector. The end of the grounded coplanar waveguide was a bit larger than designed since there was a minimum spacing size between PCB edge and the copper plating. The soldering of the legs and pins which is expected to influence the antenna performance significantly is also stated in Table 24. The first technique used was soldering by hand using a small soldering iron. The other technique is used by placing small soldering glue dots around and heat them up with hot air using an air gun.

Table 24: Adjustments on prototype PCB, H = by hand, M = machined, A = air blown soldering.

Version	Shorten	Solder pin	Solder legs	holes
V1	M	A	A+H	M
V2	M	A	A+H	M
V3	H	H	H	H
V4	H	A	H	H
V5	H	H	H	H
V6	H	H	H	H

From the S11 results of a bare PCB it can be seen that the soldering methods do indeed influence the results significantly.

The following subsections will show the measurement results of the S11 parameters of all PCB versions 1-6, the measured radiation pattern over a frequency range of 10 GHz to 30 GHz of PCB version 1,2,3,5 and the polar plots of these radiation patterns on 24 GHz and 25 GHz since this is the range of interest. The reason for leaving out PCB version 4 and 6 is due to their shifted S11 parameters to 20 GHz which is not as desired.

The following sections will show the measurement results of the different version prototype antennas.

I.1 Measurement Results

I.1.1 S11 Results

This section shows the measured S11 parameter results. The bare PCB means only the slot is radiating without an aluminium L2 on top of it and also without the resonator. With just a microstrip fed slot antenna with a length of 5.5 mm one would expect the S11 parameters to be a single peak around 27.3 GHz. However, from Figure 82 one could see that the measured S11 parameters are all shifted and have multiple peaks.

With the DRAs and aluminium L2 ground plane added to the structures, one could see from Figure 83 that the resonant frequency indeed shifts to a lower frequency. However, almost none of the resonant dips do really resonate at the designed 24.125 GHz. The largest dips from V1 and V5 resonate around 25 GHz while the other two PCB versions are still resonating around 27 GHz.

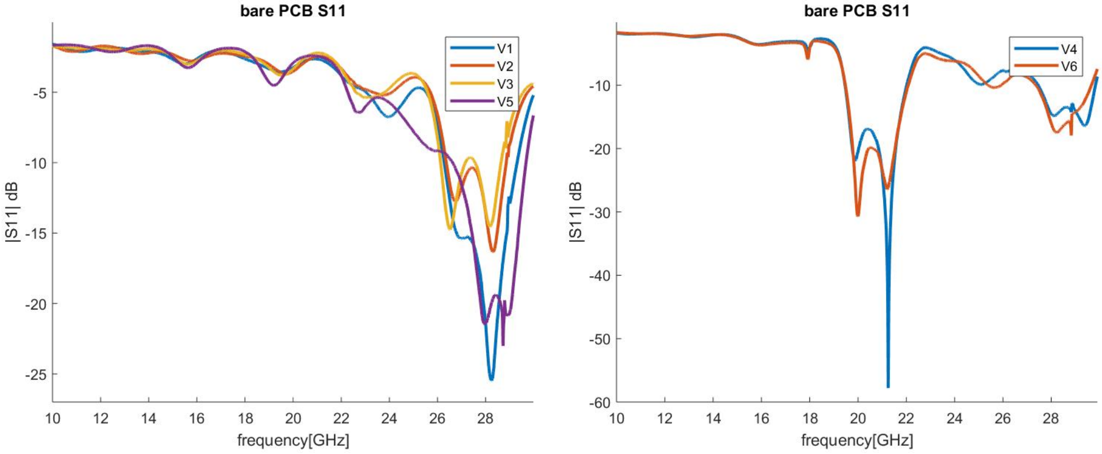

(a) S11 results of bare PCB version 1,2,3,5 **(b)** S11 results of bare PCB version 4,6

Figure 82: S11 measurement results of bare PCBs

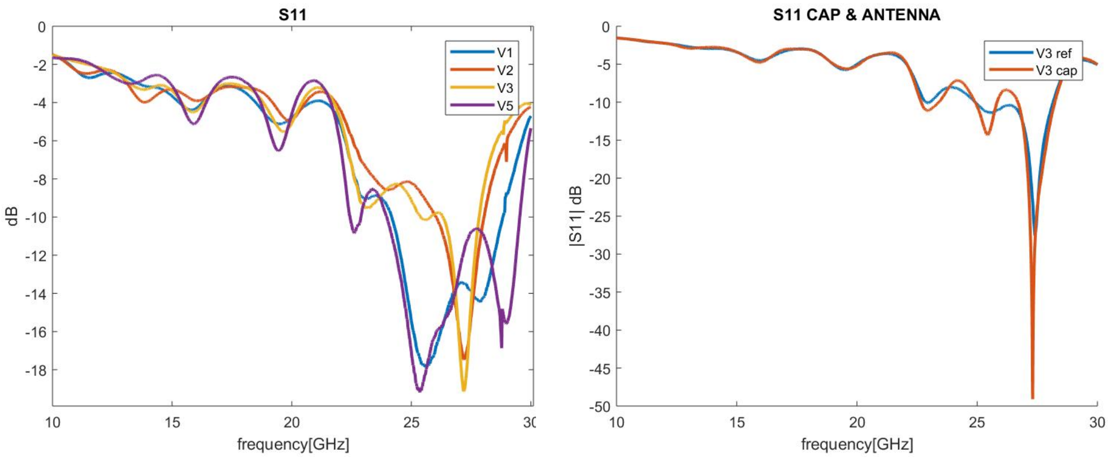

(a) S11 results of DRA + PCB version 1,2,3,5 **(b)** S11 results of V3 PCB,DRA and bulb cap

Figure 83: S11 measurement results of adding the DRA and bulb cap.

I.1.2 Radiation Pattern Results over Frequency Range 10 GHz to 30 GHz

This sections shows the radiation pattern 2D fields measured over a frequency range from 10 GHz to 30 GHz. The data in the plots are given in dB and are raw measured data. Comparing different PCB versions one could say that the patterns do vary a bit and the radiation pattern of the antennas are also quite resonating around 14 GHz.

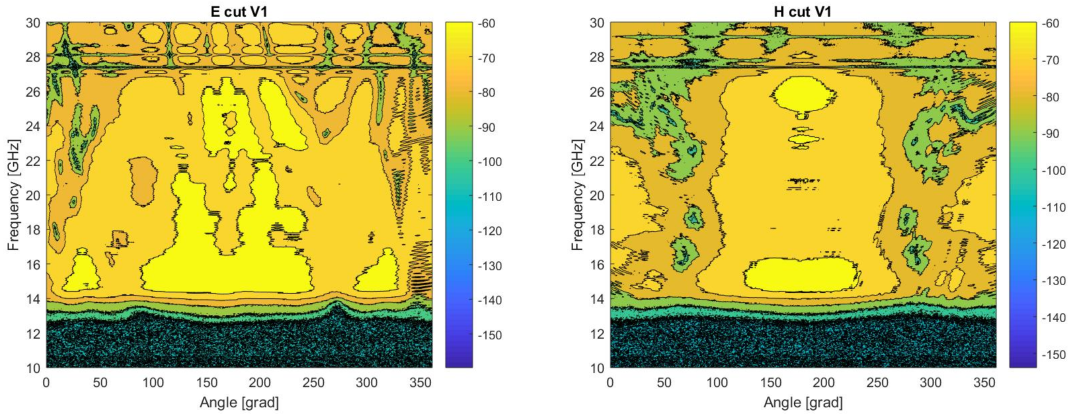

(a) E cut V1 **(b)** H cut V1

Figure 84: Radiation Pattern V1

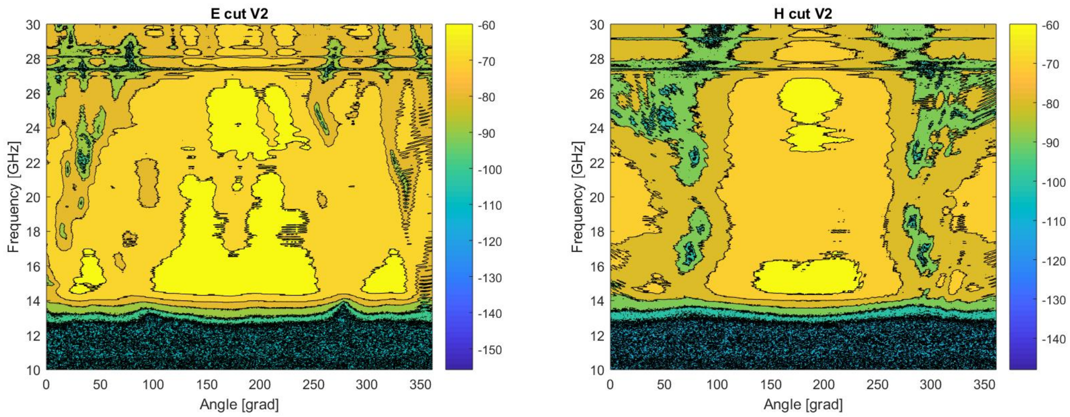

(a) E cut V2 **(b)** H cut V2

Figure 85: Radiation Pattern V2

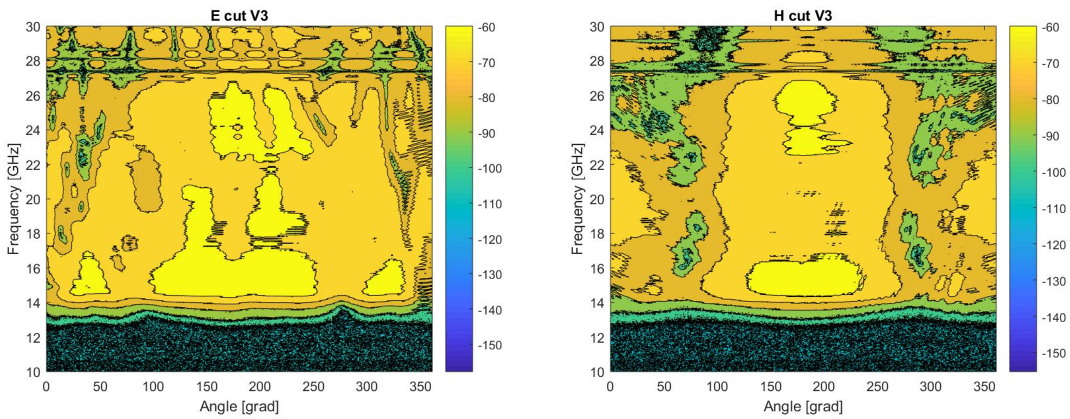

(a) E cut V3 **(b)** H cut V3

Figure 86: Radiation Pattern V3

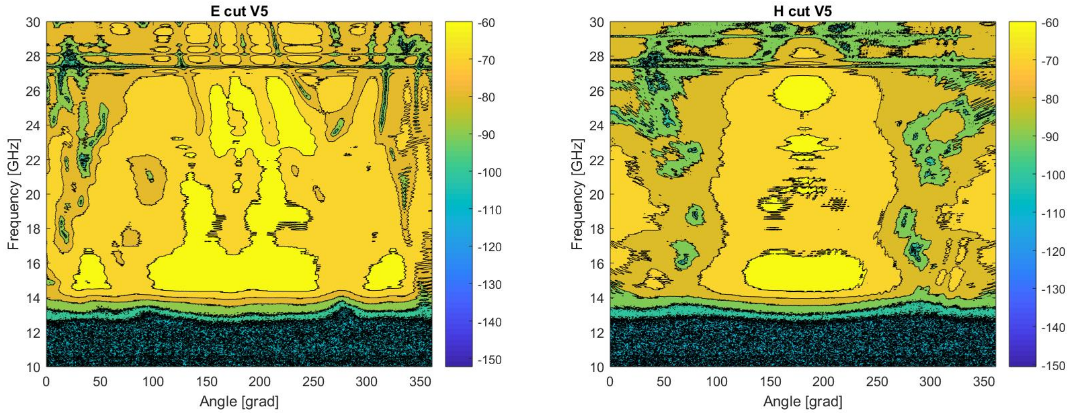

(a) E cut V5 **(b)** H cut V5

Figure 87: Radiation Pattern V5

I.1.3 Measured Radiation Patterns

This section shows the measurement results of the different PCB versions for both E and H cut. One could conclude from these measurements that the H cut are overall quite comparable to the simulated results and only the E cut differs a lot with the expected results.

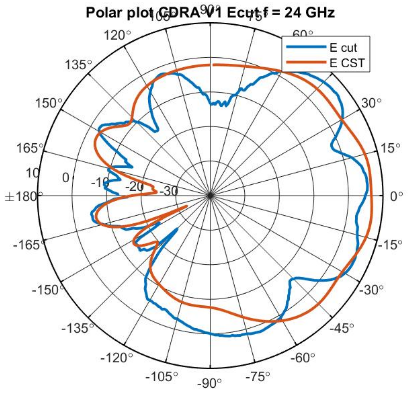

(a) E cut of V1 board at 24 GHz

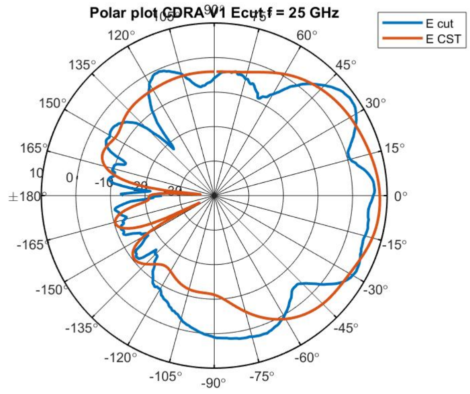

(b) E cut of V1 board at 25 GHz

Figure 88: V1 E cut at different frequencies

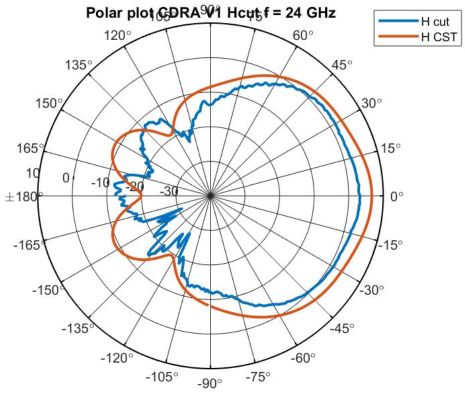

(a) H cut of V1 board at 24 GHz

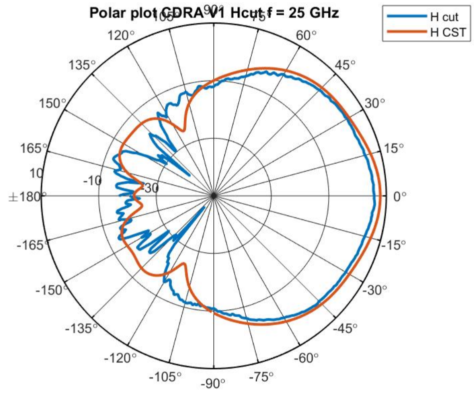

(b) H cut of V1 board at 25 GHz

Figure 89: V1 H cut at different frequencies

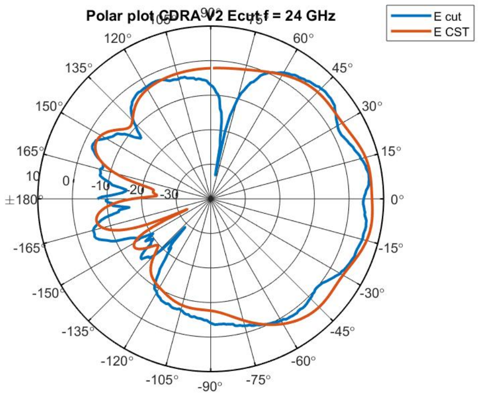

(a) E cut of V2 board at 24 GHz

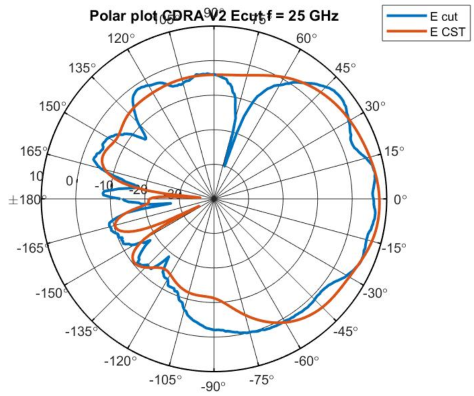

(b) E cut of V2 board at 25 GHz

Figure 90: V2 E cut at different frequencies

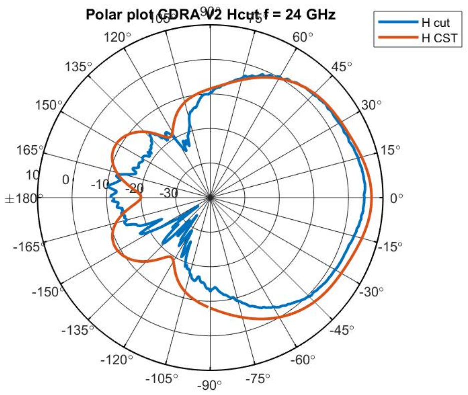

(a) H cut of V2 board at 24 GHz

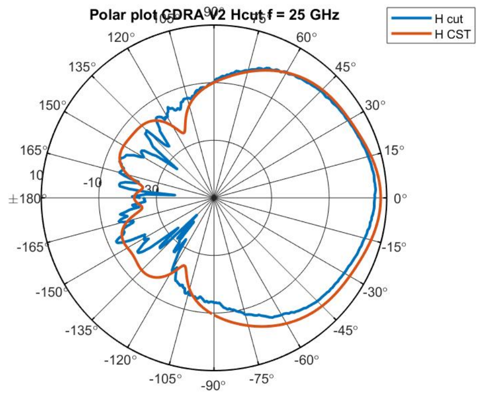

(b) H cut of V2 board at 25 GHz

Figure 91: V2 E cut at different frequencies

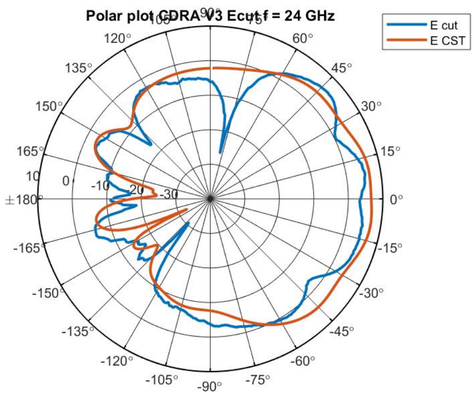

(a) E cut of V3 board at 24 GHz

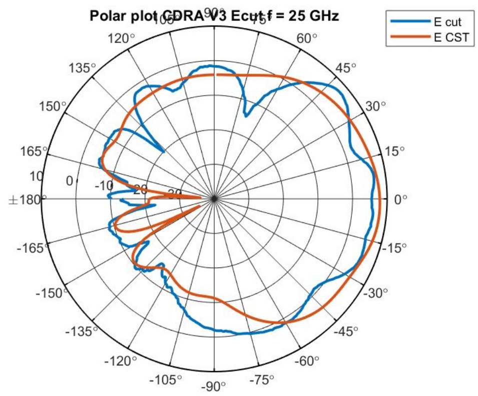

(b) E cut of V3 board at 25 GHz

Figure 92: V3 E cut at different frequencies

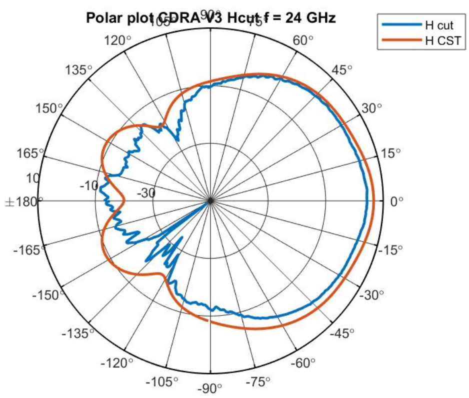

(a) H cut of V3 board at 24 GHz

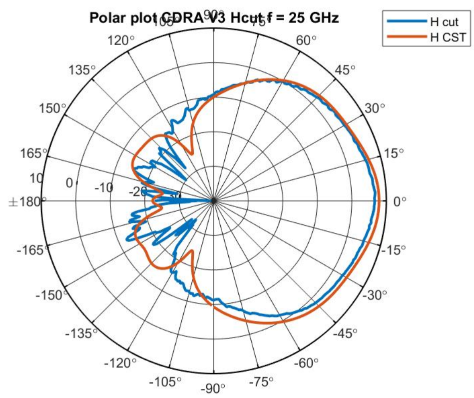

(b) H cut of V3 board at 25 GHz

Figure 93: V3 H cut at different frequencies

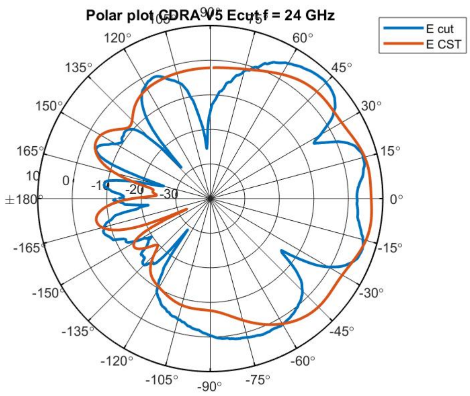

(a) E cut of V5 board at 24 GHz

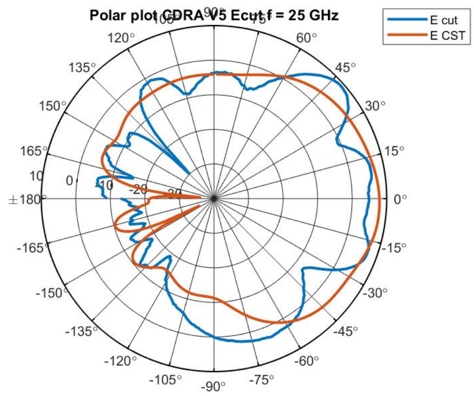

(b) E cut of V5 board at 25 GHz

Figure 94: V5 E cut at different frequencies

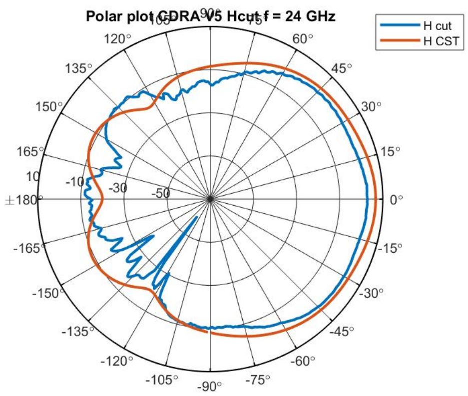

(a) H cut of V5 board at 24 GHz

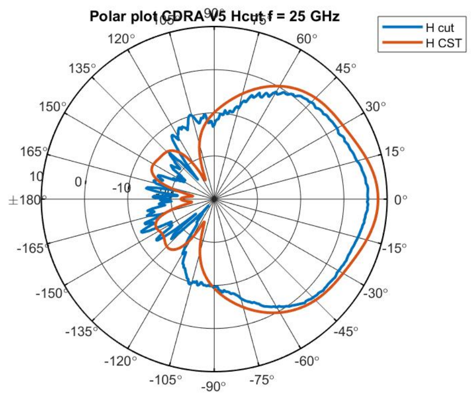

(b) H cut of V5 board at 25 GHz

Figure 95: V5 E cut at different frequencies

The following plots are measured with different DRA sizes, where a is the radius of the dielectric resonator and H the height. The PCB V1 will be used for each measurement to consider the effect of the different DRA sizes.

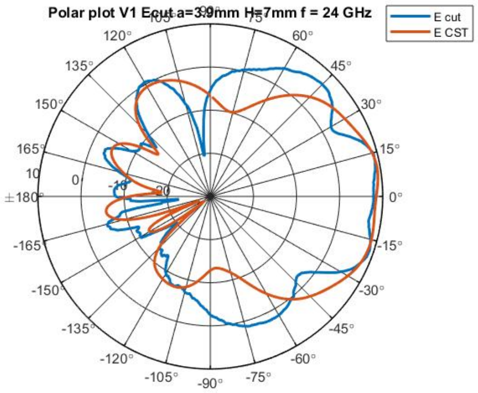

(a) E cut of V1 board with DRA dimensions a=3.9mm H=7mm at 24 GHz

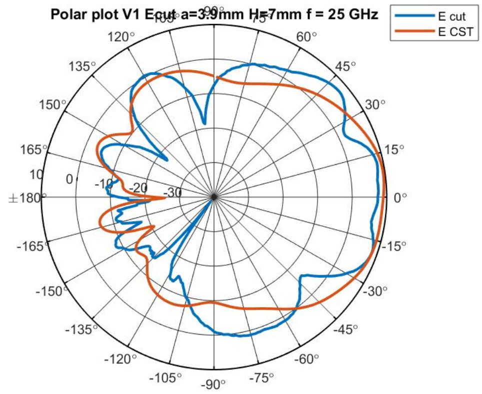

(b) E cut of V1 board with DRA dimensions a=3.9mm H=7mm at 25 GHz

Figure 96: V1 a=3.9mm H=7mm E cut at different frequencies

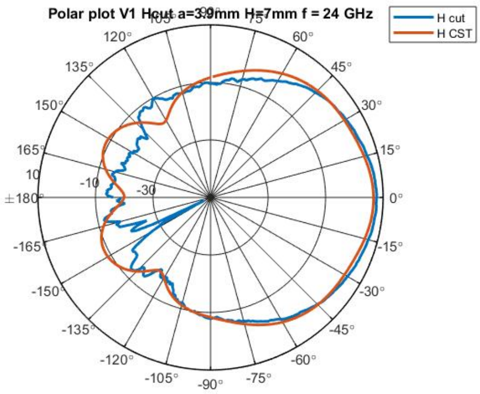

(a) H cut of V1 board with DRA dimensions a=3.9mm H=7mm at 24 GHz

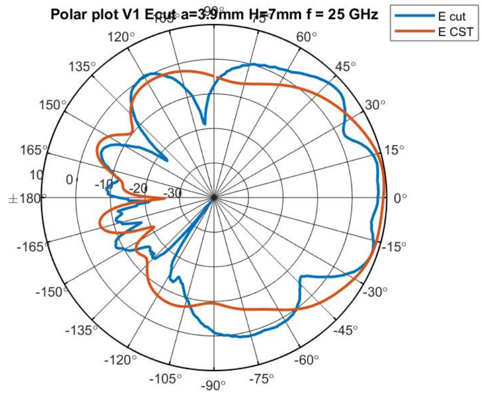

(b) H cut of V1 board with DRA dimensions a=3.9mm H=7mm at 25 GHz

Figure 97: V1 a=3.9mm H=7mm H cut at different frequencies

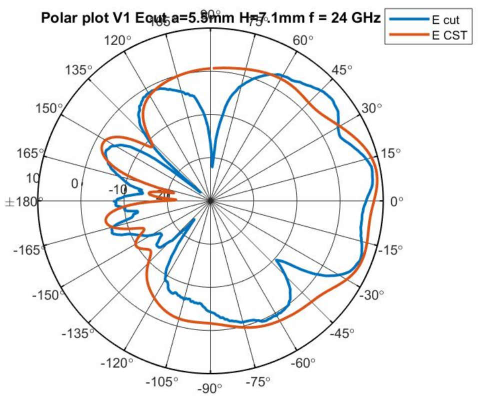

(a) E cut of V1 board with DRA dimensions a=5.5mm H=7.1mm at 24 GHz

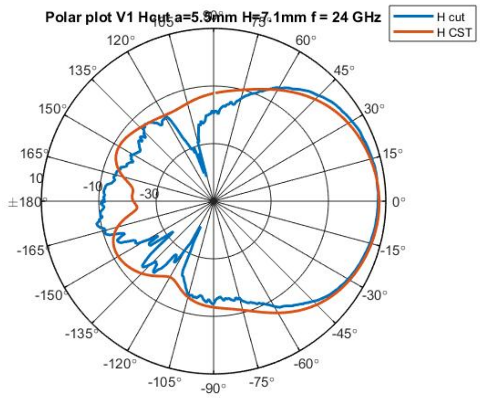

(b) H cut of V1 board with DRA dimensions a=5.5mm H=7.1mm at 24 GHz

Figure 98: V1 a=5.5mm H=7.1mm E,H cut at 24 GHz

J Matlab Code

Separate Matlab files will be used for different transmit waveforms in order to compare their detection performance under the identical detection methods.

J.1 Fast_Chirp_Radar_Model.m

The purpose of the Fast_Chirp_Radar_Model.m script is to model the radar system by using the fast chirp waveform and its corresponding 2D FFT signal processing. This script is used as main file which also includes other functions. The input parameters which are relevant for this script are hereafter.

Table 25: Input parameter of Fast_Chirp_Radar_Model.m

Parameter	Description	Unit
fs	sample frequency	Hz
T_{sweep}	sweep time of a single ramp	s
M	number of points for first FFT	-
N	number of points for second FFT	-
K	amount of ramps per sample period	-
dsr	down sample rate	-
fc	carrier frequency	Hz
B	sweep bandwidth	Hz
c	speed of light	m/s
Vtx	target speed	m/s
Rtx	target range	m
rcs	radar cross section of target	m^2
Tc	radar transceiver chip temperature	deg
Ta	antenna temperature	deg
T0	room temperature	K
Gtx,Grx	gain transmit, receive antenna	dB

For the target related parameters as stated above x can be replaced by the target number (1,2,3...).

```
close all,clear all,clc
% ----------------------- Fast Chirp waveform -----------------------------
%   fd_max < 1/(2*Tramp)
%   dFd = 1/(Tramp*Ns);
%   dR = c/(2*B) = 0.75m
%   dV = lambda/(2*Tsweep*K) = 62.1332/K  m/s
%   unambiguity:
%       R_ua = fs*c/(2*B*PRF) = 3.75e4 m
%       V_ua = c*PRF/(4*fc) = 31.0666 m/s
% ----------------------------- START CODE ---------------------------------
addpath ('LUT','functions');
%% Parameters
fs = 500e6;                     % Fs >= 2*B = 500 MHz
Tsweep = 0.1e-3;                % single ramp sweep time, max 0.777 ms // PRF > = 5.1661e-08 , Tramp = 1/PRF
% Ttrans = 0.1e-4;              % transit time after one ramp
% Tramp = Tsweep + Ttrans;      % total ramp time

% M = 2048;                     % 1st FFT Range// required M >= 1935.7 --> 2^11 in total
```

```
% N = 32768;                        % 2nd FFT Doppler

K = 256;                            % amount of sample period sweeps for processing
dsr = 2^10;                         % down sample rate 2^10 max for Rua > 10 m

% predefined variables/ constants
fc = 24.125e9;                      % center/carrier frequency // predefined
B = 200e6;                          % sweep bandwidth (max ISM band 250e6) // predefined
c = physconst('LightSpeed');        % speed of light [m/s]

% Target definition
Vt1 = -1;                           % target speed [m/s] < 4 m/s
Rt1 = 6;                            % target range [m]  < 10 m
Vt2 = -1.5;
Rt2 = 8;

% RCS
rcs1 = 1;
rcs2 = 1;

alpha = B/Tsweep;                % chirp rate/ slope
lambda = c/fc;                  % wavelength Rx signal

% Chip Temperature
T = 25;
% Antenna temperature
Ta = 25;

% Radar Equation parameters
T0 = 290;                   % room temperature
Tsys = 273.15 + T;            % system temperature [K]
Gtx = 10^(8/10);            % 7 - 9 dBi from antenna gain
Grx = 10^(8/10);

% fast time t for each ramp from [-Tsweep/2, Tsweep/2]
tvec = -Tsweep/2 : 1/fs : Tsweep/2 - 1/fs;
% slow time k, # of ramps in total
kvec = 1:K;
[t,k] = meshgrid(tvec,kvec);

%% LUT
NF = NF_I_MTR(T);
CG = VCG_I_MTR(T);
PTx = PTx_LUT_MTR(T);
Atx = sqrt(PTx);                % transmit amplitude

%% FAST CHIRP S_TX, I signal
s_tx = Atx.*sin( 2*pi*fc*t + pi*alpha.*t.^2);

%% Target detection
tdvec = Tsweep.*kvec;           % target displacement in slow time
tfvec = 0:1/fs:Tsweep-1/fs;     % target fast time [0,Tsweep]
[td,tf] = meshgrid(tdvec,tfvec);
[tau1, ~] = target(Vt1, Rt1, td, c, fc, tf);
[tau2, ~] = target(Vt2, Rt2, td, c, fc, tf);
```

```
%% FAST CHIRP S_RX
% Amplitude Reflected Signal
[Prx1] = radar_eq(fc, PTx, Gtx, Grx, Rt1, rcs1);
[Prx2] = radar_eq(fc, PTx, Gtx, Grx, Rt2, rcs2);
Arx1 = sqrt(Prx1);
Arx2 = sqrt(Prx2);
s_rx =  Arx1.*sin( 2*pi*fc*(t-tau1') + pi.*alpha.*(t-tau1').^2) + ...
        Arx2.*sin( 2*pi*fc*(t-tau2') + pi.*alpha.*(t-tau2').^2);

% Mixer signal output
s_mix = s_rx.*conj(s_tx);

%% downsampling + FIR lowpass filter
fsd = fs/dsr;                  % >= 2*fb_max
s_ds = zeros(K,ceil(length(t)/dsr)); % [K x # down samples]
for ll = 1:K
s_ds(ll,:) = decimate(s_mix(ll,:),dsr,'fir');       % FIR lowpass by default Chebyshev filter/ FIR order n = 20
end

s = s_ds;                         % input signal to plot and FFT
fft_dB = 20*log10(abs(fftshift(fft2(s),1)));   % 2D FFT

%% Unambiguous Range and Velocity Theoretical Computation
PRF = 1/Tsweep;
R_ua = fs*c/(2*B*PRF);
V_ua = c*PRF/(4*fc);
% Unambiguity downsampled signal
R_uads = fsd*c/(2*B*PRF);     % sample frequency is different
V_uads = V_ua;

%% PLOT
% imagesc([0, R_ua],[-V_ua, V_ua],fft_dB);
% xlabel('Range bin');
% ylabel('Velocity bin');
% title('SNR Plot[dB]');
% colorbar

% plot range-doppler plot of down sampled signal
imagesc([0, R_uads],[-V_uads, V_uads], fft_dB);
xlabel('Range[m]');
ylabel('Velocity[m/s]');
title('Range-Doppler Plot Down Sampled');
shg

% --------------------------- END OF CODE --------------------------------

%% beat and doppler frequency
% fb = 1.674258e5 for Rmax = 10, Vmax = 4

% V = 4;%V_ua;
% R = 10;%R_ua;
% fd = 2*fc*V/c;                    % max doppler frequency
% fr = 2*R*alpha*(1-2*V/c)/c;       % max range beat frequency
% fb = fd + fr

%% plot range-doppler plot of mixed signal
```

```matlab
% imagesc([0, R_ua],[-V_ua, V_ua], fft_dB);         % axis limited by unambiguous range/velocity
% set(gca,'clim',[-60 0],'xlim',[0 30],'ylim',[-10 10]);
% xlabel('Range[m]');
% ylabel('Velocity[m/s]');
% title('Range-Doppler Plot Mixed');

%% Matlab Radar Equation Approximation
% SNR1 = radareqsnr(lambda,Rt1,PTx,Tsweep*K,'Gain',7)
% SNR2 = radareqsnr(lambda,Rt2,PTx,Tsweep*K,'Gain',7)
% SNR = 10;
% RCS = 1;
% Pt = radareqpow(lambda,Rt1,SNR,Tsweep*K,'rcs',RCS,'gain',Grx)
% maxrng = radareqrng(lambda,SNR,Pt,Tsweep*K,'rcs',RCS,'gain',Grx)
```

matlab/Fast_Chirp_Radar_Model.m

J.1.1 Triangle_Radar_Model.m

The triangle radar model is based on a slow triangle waveform and uses the up and down beat frequency to determine the target range and velocity.

```matlab
close all,clear all,clc
% ------------------------- TRIANGULAR FMCW ------------------------------
% generates a up and down chirp and adds them together to create a
% triangular waveform.
% afterwards the mixed signal of the transmit and received is Fourier
% transformed resulting in a beat frequencies.
% The beat frequencies are then used for the range and velocity computation
% of the target.
%
% TO DO:
% - target approaching angle
% - antenna gain from CST for models
% ---------------------------- START CODE --------------------------------
% profile on
addpath ('LUT','functions');

%% Parameters
B = 200e6;                     % sweep bandwidth (max ISM band 250e6)
fs = 2*B;                      % Fs >= 2*B = 400 MHz
Ts = 1/fs;                     % sampling period
fc = 24.125e9;                 % center frequency for sweep between 25-225 MHz
Tcpi = 2e-3;                   % coherent processing interval time
T = Tcpi/2;                    % factor 1/2 due to up & down chirp generation
c = physconst('LightSpeed');   % speed of light [m/s]
lambda = c/fc;                 % wavelength Rx signal
alpha = B/T;                   % since one period is now T/2
% Target parameters
Vt = 1;                        % target speed [m/s] < 4 m/s
R = 5;                        % target range [m] < 10 m
rcs = 1;
% Temperatures in Celsius
```

```
Tc = 60;                           % chip
Ta = 40;                           % antenna
Tr = 25;                           % room temperature
% Radar Equation parameters
T0 = 290;                          % room temperature [K]
Tsys = 273.15 + Tc;                % system temperature [K]
Gtx = 10^(8/10);                   % 7 - 9 dBi from antenna gain (simulations)
Grx = 10^(8/10);
NF = 12.4275; % in dB at 24.125 GHz and 25 Celsius

% timing vector
t = -T/2 : 1/fs : T/2 - 1/fs;


%% transmit signal
% read out given values for BGT24MTR11 transceiver
Ptx = PTx_LUT_MTR(Tr);
Atx = sqrt(Ptx);
NF_I = NF_I_MTR(Tr);         % noise figure I signal
VCG_I = VCG_I_MTR(Tr);       % voltage conversion gain I signal
% transmitted signal
stx_up =@(t) Atx.*exp(1i.*( 2*pi*fc*t + pi*alpha.*t.^2)); % upchirp
stx_down =@(t) Atx.*exp(1i.*( 2*pi*fc*t - pi*alpha.*t.^2)); % downchirp
stx = [stx_up(t) stx_down(t)]; % one ramp generation

%% received signal
% Amplitude of received signal
Prx = radar_eq(fc, Ptx, Gtx, Grx, R, rcs);
Arx = sqrt(Prx);
% target induced parameters
tau = 2 * R / c;
fD = -2*fc*Vt / c;
% phase of the received signal
phi_r_up =@(t) 2*pi*fc.*(t-tau) + pi*alpha.*t.^2 - 2*pi*alpha*tau.*t + 2*pi*fD.*t;
phi_r_down =@(t) 2*pi*fc.*(t-tau) - pi*alpha.*t.^2 + 2*pi*alpha*tau.*t + 2*pi*fD.*t;
% up and down sweep signal
srx_up =@(t) Arx.*exp(1i.*(phi_r_up(t)));
srx_down =@(t) Arx.*exp(1i.*(phi_r_down(t)));
% add up and down for one combined signal
phi_r = [phi_r_up(t) phi_r_down(t)];
srx = Arx.*exp(1i.*(phi_r));
% srx = awgn(srx,60);                              % White Gaussian Noise


%% Plots FD, TD received sweeps
% FD received signal
% subplot(311)
% spectrogram((s_rx_up(t)),128,64,128,fs,'yaxis'); title('s_{rx} up');
% subplot(312)
% spectrogram((s_rx_down(t)),128,64,128,fs,'yaxis'); title('s_{rx} down');
% subplot(313)
% spectrogram((srx),128,64,128,fs,'yaxis'); title('s_{rx} combined');

% TD received signal
% plot(t,srx_up(t));title('s_{rx} up');
```

```
% figure;
% plot(t,srx_down(t));title('s_{rx} down');
% figure;
% t2 = -T : 1/fs : T - 1/fs;
% plot(t2,srx);title('s_{rx} combined');


%% Processing
% Window received signal, smearing with factor 1.5
Wud = kaiser(length(srx_down(t)),2);
W = kaiser(length(srx),2);
% mix transmit and receive signal & apply window
% s_mixd = Wud'.*srx_down(t).*conj(stx_down(t));
% s_mixu = Wud'.*srx_up(t).*conj(stx_up(t));
% s_mix = W'.*srx.*conj(stx);
% out comment this part below for no windowing
s_mixd = srx_down(t).*conj(stx_down(t));
s_mixu = srx_up(t).*conj(stx_up(t));
s_mix = srx.*conj(stx);

% -------------
% downsampling
% -------------
dsr = 2^10; % <= 1495.3, max 2^10
fsd = fs/dsr;
s_ds = decimate(s_mix,dsr);       % FIR lowpass by default Chebyshev
    filter/ FIR order n = 20

% -------------
%   FFT + MIX
% -------------
% zero pad of 2^25 of total signal is needed without downsampling to get a
% very accurate fb readout.
s = s_ds;
% Smixd = 20*log10(abs(fftshift(fft(s_mixd)))); % zpad
% Smixu = 20*log10(abs(fftshift(fft(s_mixu)))); % zpad
Smix = 20*log10(abs(fftshift(fft(s,2^10)))); % zpad*2,extra zero pad since
     mixed signal is double in length compared to the separate mixed one


%%  Detection
NFFT = length(Smix);         % length mixed signal
k = 0:NFFT-1;                % frequency index
f = (-NFFT/2+k)/NFFT * fsd; % change the fs to fsd for down sampled
    signals

plot(f,Smix,'LineWidth',1.5); xlabel('Frequency[Hz]');ylabel('Power[dB]');
% title('Mixed Tx,Rx Signal');
% xlim([-40 40]);

% make the frequency grid for NFFT/2 sized signal
NFFT2 = NFFT/2;
p = 0:NFFT2-1;
f2 = (-NFFT2/2+p)/NFFT2 * fs;

% figure;
% plot(f2*10^-3,Smixu);hold on;
% plot(f2*10^-3,Smixd); xlabel('Frequency[kHz]');ylabel('Power[dB]');
```

```matlab
% title('Mixed Up and Down Ramp');
% legend('Mixed Up ramp','Mixed Down ramp');
% xlim([-40 40]);

% -------------
%   MAX PEAKS
% -------------
% fbu_val = max(Smixu);            % get max peak
% fbu_bin = find(Smixu==fbu_val);  % find bin value
% fbu = f2(fbu_bin);               % corresponding bin freq.
% fbd_val = max(Smixd);            % get max peak
% fbd_bin = find(Smixd==fbd_val);  % find bin value
% fbd = f2(fbd_bin);               % corresponding bin freq.

% -------------
%     CFAR
% -------------
% Threshold = alpha * Pn
% alpha = N(Pfa^(-1/N) - 1)
% Pn = 1/N sum(Xm) for m = 1:N

Tcells = 20;                       % training cells
Gcells = 10;                       % guard cells
Pfa = 1e-3;                        % false alarm rate

x = 10.^(Smix./10);                % mixed signal in time domain
Ncells = length(x);                % total signal
Tcells2 = round(Tcells/2);         % one side training cells
Gcells2 = round(Gcells/2);         % one side guard cells
Scells = Gcells2 + Tcells2;        % one side total cells

alpha = Tcells*(Pfa*(-1/Tcells) - 1);% detector scale factor

th = zeros(1,Ncells);
for i = Scells+1 : Ncells-Scells-1  % +-1 due to Matlab indexing
    % summation left and right training cells of CUT
    sumR = sum(x(i-Scells : i-Gcells2-1));
    sumL = sum(x(i+Gcells2+1 : i+Scells));
    % taking average of all test cells
    Pn = (sumR + sumL)./Tcells;
    th(i) = alpha.*Pn;             % starts at 15
    % compensate threshold for the first&last one sided cells
    if i <= Scells+1               % first Scells+1 replaced by first th value
    th = [linspace(th(Scells+1),th(Scells+1),Scells) th(i)];
    elseif i >= Ncells-Scells-1    % replace last Scells by last th value
    th = [th linspace(th(Ncells-Scells-1),th(Ncells-Scells-1),Scells+1)];
    end

end
hold on;
plot(f, 10*log10(th),'LineWidth',1.5);
legend('Mixed FFT signal','CA CFAR Threshold');

th_dB = 10*log10(th);
pkidx = find(Smix > th_dB);        % get element values of peaks
[pks,pklocs] = findpeaks(Smix(pkidx));% peak values & location
fb = f(pkidx(pklocs))             % obtain resulting peak frequency
```

```
% fstep = fsd/NFFT;                    % minimum FFT resolution

% -------------
%  TARGET R,V
% -------------
fbu = fb(1);
fbd = fb(2);
R_t = (fbd - fbu) * c * Tcpi / (8 * B)
v_t = -1.*(fbd + fbu) * lambda / 4

% profile viewer
% ----------------------------- END CODE ----------------------------------
%% theoretical frequency shifts
% tau = 2 * R / c;                  % time delay
% fb = tau * B / T;                 % range freq shift
% fd = 2 * fc * Vt ./ c;            % Doppler freq shift
% fbu = fb + fd
% fbd = -fb + fd
% R_t = (fbu - fbd) * c * Tcpi / (8 * B) % target range
% v_t = (fbd + fbu) * lambda / 4

%% plots
% subplot(311)
% spectrogram((s_tx_up(t)),128,64,128,fs,'yaxis'); title('s_{tx} up');
% subplot(312)
% spectrogram((s_tx_down(t)),128,64,128,fs,'yaxis'); title('s_{tx} down');
% subplot(313)
% spectrogram((s_tx),128,64,128,fs,'yaxis'); title('s_{tx} combined');

% spectrogram((s_mix),128,64,128,fs,'yaxis'); title('s_{mix}');
% fft_dB = 20*log10(abs(fftshift(fft(s_mix))));
% f = (0:length(fft_dB)-1)*800000/length(fft_dB);
% plot(f,fft_dB);
```

matlab/Triangle_Radar_Model.m

J.2 radar_eq.m

```
% -------------------------- RADAR EQUATION -------------------------------
% Parameters:
% freq       = frequency [Hz]
% lambda     = wavelength [m]
% Gtb        = time bandwidth product gain
% Gd         = Doppler processing gain
% G          = total antenna gain (Rx & Tx)
% L          = system losses
% F          = noise figure
% T          = antenna temperature
% Rmax       = maximum radar range
% rcs        = radar cross section target
% Rt         = target range
% -------------------------- START FUNCTION -------------------------------
% function [amplitude, Rmax] = radar_eq(freq, T, Pt, Gtx, Grx, L, Rt, rcs,
   SNRmin,NF)
```

```matlab
function [Prx] = radar_eq(freq, Pt, Gtx, Grx, Rt, rcs)
% constants
% k = physconst('Boltzmann');     % boltzman constant [J/deg]
c = physconst('LightSpeed');       % speed of light [m/s]
lambda = c./freq;    % wavelength
Prx = Pt.*Gtx.*Grx.*lambda^2.*rcs ./ ((4*pi)^3.*Rt.^4);

end
% --------------------------- END FUNCTION --------------------------------
```

matlab/radar_eq.m

J.3 target.m

```matlab
% -------------------------- TARGET model --------------------------------
% Input:
% - Vt: target velocity
% - R: target range
% - t_slow: slow time
% - c: speed of light
% - f0 : carrier frequency
% - t_fast : fast time
%
% output
% - tau: time delay due to target reflection
% - fd: Doppler shift frequency due to target
%
% ---------------------------- START CODE ---------------------------------

function [tau, fd] = target(Vt, R, t_slow, c, f0, t_fast)

% tau = 2.*(R + Vt*t_slow + Vt*t_fast)./c;              % reflected signal time delay
tau = 2.*(R + Vt*t_slow)./c;              % reflected signal time delay
fd = -2.*f0.*Vt./c;                   % Doppler shift

end

% ---------------------------- END OF CODE --------------------------------
```

matlab/target.m

J.4 LUT

```matlab
function [VCG_I_val] = VCG_I_MTR(T)
% measured at 24.125 GHz?
% values readout are in dB
VCGrefI = [10.2414356
    12.42750453
    14.4048648];
Tref = [-40 25 125];

Ti = -40:1:125;
VCGI = interp1(Tref,VCGrefI,Ti);

```

```
index = find(T == Ti);                  % get index for T
VCGI_valdB = VCGI(index);                 % get value for T
VCG_I_val = 10^(VCGI_valdB/10);

end
```

matlab/VCG_I_MTR.m

```
function [NF_I_val] = NF_I_MTR(T)
% measured at 24.125 GHz?
% values readout are in dB
Ptxref = [10.2414356
    12.42750453
    14.4048648];
Tref = [-40 25 125];

Ti = -40:1:125;
NFI = interp1(Tref,Ptxref,Ti);

index = find(T == Ti);                  % get index for T
NFI_valdB = NFI(index);                 % get value for T
NF_I_val = 10^(NFI_valdB/10);

end
```

matlab/NF_I_MTR.m

```

function [Ptx_val] = PTx_LUT_MTR(T)
% measured at 24.125 GHz?
% values readout are in dB
Ptxref = [12.10707587
    11.34168173
    10.04211867];
Tref = [-40 25 125];

Ti = -40:1:125;
Ptx = interp1(Tref,Ptxref,Ti);

index = find(T == Ti);                  % get index for T
Ptx_valdB = Ptx(index);                 % get value for T
Ptx_val = 10^(Ptx_valdB/10);

end
% plot(Ti,Ptx,'*');
```

matlab/PTx_LUT_MTR.m

```
% ------------------------ VCO BGT24LTR11N16 ------------------------------
% generates lookup table for the tuning voltage of the VCO integrated in
% the infineon transceiver BGT24LTR11N16.
% inputs:
%   - V_PTAT: readout to get chip temperature
%   - f_VCO: desired VCO frequency
% output:
%   - v_tune: tuning voltage needed for specified VCO frequency
%
% ---------------------------- START CODE ---------------------------------
```

```

function [v_tune] = VCO_LUT(T, f_VCO)

% f_VCO = A + Bx - Cx2
%   A,B and C are fits of f_VCO over different temperatures.
%   f_VCO is also fitted based on the measured data in the datasheet
A = [23157.28751 23061.86829 22962.9124 22826.00536 22739.9495 22622.9191
    22475.07532];
B = [1054.59809 1066.05281 1073.53223 1097.06897 1108.83051 1131.96225
    1152.88345];
C = [140.94337 142.56955 142.73041 147.77887 149.1121 155.32744
    158.88117];

%% interpolate for every 1 degree celsius
Tp = [-40 -20 0 25 40 60 85];    % measured temperature points
Ti = -40:1:85;                   % interpolated temperature vector
Afit = interp1(Tp,A,Ti);
Bfit = interp1(Tp,B,Ti);
Cfit = interp1(Tp,C,Ti);
index = find(T == Ti);           % get index for T
Afit = Afit(index);              % get value for T
Bfit = Bfit(index);
Cfit = Cfit(index);

%% total function
% solved v_tune with function :
%   f_VCO = Afit   +   Bfit.*v_tune      -  Cfit.*v_tune.^2;
% ABC formula output for v_tune
v_tunep = (Bfit + sqrt(Bfit^2-4*Cfit*f_VCO + 4*Afit*Cfit))/(2*Cfit);
v_tunem = (Bfit - sqrt(Bfit^2-4*Cfit*f_VCO + 4*Afit*Cfit))/(2*Cfit);
% select only positive value for v_tune
v_tune = [v_tunep v_tunem];
v_tune = v_tune(v_tune > 0);

end

% ---------------------------- END OF CODE
    --------------------------------

%% polynomial fit of 9th order
% Afit= 22969.92478         - 5.90363.*T ...
%     -0.05561.*T^2         + 0.00148.*T^3 ...
%     +5.30457E-5.*T^4      - 1.28447E-6.*T^5 ...
%     -1.0616E-8.*T^6       + 4.23217E-10.*T^7 ...
%     -3.14336E-12.*T^8     + 6.16871E-15.*T^9;
% Bfit = 1073.36476         + 0.76122.*T ...
%     +0.0236.*T.^2         - 3.46738E-4.*T.^3 ...
%     -2.32489E-5.*T.^4     + 4.43557E-7.*T.^5 ...
%     +5.82098E-9.*T.^6     - 1.71351E-10.*T.^7 ...
%     +9.89909E-13.*T.^8    - 4.1395E-16.*T.^9;
% Cfit = 142.84382          + 0.13565.*T ...
%     +0.00738.*T.^2        - 1.15177E-4.*T.^3 ...
%     -7.7494E-6.*T.^4      + 1.46636E-7.*T.^5 ...
%     +2.17063E-9.*T.^6     - 5.76088E-11.*T.^7 ...
%     +2.55997E-13.*T.^8    + 4.64124E-16.*T.^9;

%% Linear formula, linear interpolation fit
% switch logical(true)
```

```
%      case T < -20
%          Afit = -4.7710*(T+40) + A(1);
%          Bfit = 0.5727*(T+40) + B(1);
%          Cfit = 0.0813*(T+40) + C(1);
%
%      case T >= -20 && T < 0
%          Afit = -4.9478*(T+20) + A(2);
%          Bfit = 0.3740*(T+20) + B(2);
%          Cfit = 0.0080*(T+20) + C(2);
%
%      case T >= 0 && T < 25
%          Afit = -5.4763*T + A(3);
%          Bfit = 0.9415*T + B(3);
%          Cfit = 0.2019*T + C(3);
%
%      case T >= 25 && T < 40
%          Afit = -5.7371*(T-25) + A(4);
%          Bfit = 0.7841*(T-25) + B(4);
%          Cfit = 0.0889*(T-25) + C(4);
%
%      case T >= 40 && T < 60
%          Afit = -5.8515*(T-40) + A(5);
%          Bfit = 1.1566*(T-40) + B(5);
%          Cfit = 0.3108*(T-40) + C(5);
%
%      case T >= 60     % gives small rounding errors with constants
%          Afit = ((A(7)-A(6))/25) *(T-60) + A(6); %-5.9138
%          Bfit = ((B(7)-B(6))/25)*(T-60) + B(6); %0.8368
%          Cfit = ((C(7)-C(6))/25)*(T-60) + C(6); %0.1421
% end
```

matlab/VCO_LUT.m